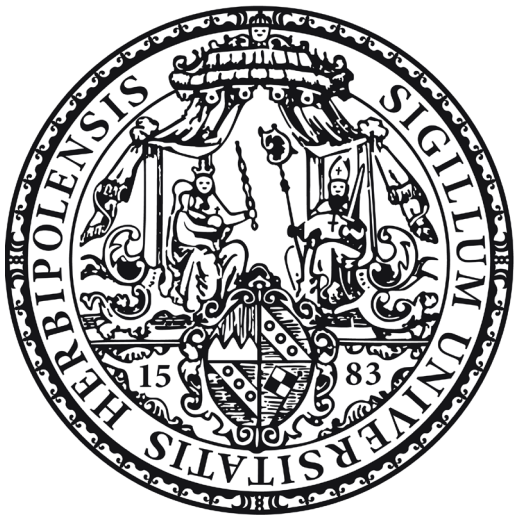

Development of *In vitro* Models for Tissue Engineering Applications Using a High-Resolution 3D Printing Technology

Entwicklung von *In vitro*-Modellen für Tissue-Engineering-Anwendungen mithilfe einer hochauflösenden 3D-Drucktechnologie

Doctoral thesis for a doctoral degree
at the Graduate School of Life Sciences,
Julius-Maximilians-Universität Würzburg

Section: Biomedicine

submitted by

Ezgi BAKIRCI

from

Azdavay, Turkey

Würzburg 2021

Submitted on:

……..……..

Office stamp

Members of the Thesis Committee

Chairperson: Prof. Dr. Thomas Dandekar

Primary Supervisor: Prof. Dr. Paul D. Dalton

Supervisor (Second): Prof. Dr. Carmen Villmann

Supervisor (Third): Prof. Dr. Reiner Strick

Date of Public Defence:

Date of Receipt of Certificates:

To my lovely family,

This work was conducted from April 2018 until November 2021 at the Department for Functional Materials in Medicine and Dentistry at the University of Würzburg under the supervision of Prof. Dr. Paul Dalton.

Acknowledgments

Without the support of many wonderful and inspirational people, this thesis would never have been completed.

First, I eternally appreciate my supervisor Paul Dalton, a great role model who gave me the strength and belief in myself to continue during the hard times. Thank you, Paul, for giving me this life-changing opportunity by showing me kindness and enjoyment in science. I have felt your support and guidance constantly, and I learned so much from you. Thank you!

I deeply thank Carmen Villmann for taking such good care of me during a challenging time, teaching me, supporting me, and listening to me; without your efforts, this project would have been a whole different story. Thank you!

Over the last three years, my time as a visiting scholar at CREATE group at the University of Otago in New Zealand has been a pivotal event. Gabriella Lindberg, Tim Woodfield, and Khoon Lim are among the most brilliant and ambitious scientists I know. I had the great pleasure of engaging with you for two months. It was the highlight of my Ph.D.

I also want to thank Reiner Strick, Hans-Werner Schmidt, and Pamela Strissel for all the advice and questions during our SFB meeting. Also, thanks to Juergen Groll and all SFB members for creating a dynamic environment for researchers. Moreover, I want to thank TRR225 A04 and B01 projects for funding.

Thank you, Andreas, Dieter, Natasha, and Simon, for all your supports and excellent companionship. You are the best colleagues I could ever wish! Thank you, Ingrid, for your collaborative work. Also, thank you, Annalena for your assistance.

I would also thank our lab technicians, Harald, Toni, Judith, and Alice, for solving my problems whenever needed. Furthermore, I would like to thank Tanja and

Brigit for their excellent administrative support. Also, thanks to the University of Wuerzburg GSLS team, especially Gabby, Irena, and Heike, for their supports.

Thanks to all the Biofab students we met across the globe, Deanna, Samantha, Tom, Marius, Andreas, especially, Ouafa, Chiara, and Hannah. Thanks to Ouafa being my first friend in Germany, showing me beautiful Wuerzburg and our long night talk about research and personal life with cold coffee in 522. Thanks to Chiara, showing me German culture and all the folk fest and making me feel a part of the Grosshaus family. Thank you, Hannah, for being always there when I need support and distraction from work.

Luckily, I also had a chance to supervise some of the Biofab students. I learned so much from you about research and about myself! Thank you, Nick, Estaban, Jae, Zeynep and Paul. I wish you all the best for your bright future!

Berat and Ali, my determined and committed companions. Thank you for all the memories over these years. It was a great pleasure!

Philipp, thank you for showing me how to make small things bigger and approaching differently to problems. Also, thanks to all SEM sessions, they were my monthly therapy.

Thank you, Andrei, Moataz, Christoph, and Carina, for being perfect senior PhDs in the MEW lab, especially Andrei; thanks for leading me in the MEW world and teaching me how to tame the jet. I missed your sarcastic jokes after your graduation. Also, I thank all the PhD students, especially Rike and Alessandro, postdocs, visiting scholars, and leaders in FMZ, for being helpful when I needed it. Special thanks to Joerg for our discussion before my seminar and Taufiq for brainstorming about creative projects! I would like to thank also all Tissue Engineering Department for confocal facility.

Biranche and Juliane…. Biranche, thank you for every moment we spent together and coming to MEW lab as first aid when all my friends left Wuerzburg!

Juliane, thank you for always being with me and bringing me more plants; visiting your home always feels like a holiday.

Also, my fellow PhDs, my mates, Rita and Sanjana. I felt so lucky that you were around for the last three years. I appreciate each year we spent together, and I am looking forward to a lifetime of funny stories and beautiful friendships. You are fantastic people, and I wish you all the best!

Thanks to my oldest friends Nage, Hanife, Cansu, Kagan, Kerstin, Ersoy, Ecem and Mehmet for being part of this journey. Also, my friends from Switzerland, Helga, Marzi, Gudong, and Georg helping me survive my PhD journey!!!! Even though there are long distances between us, we always find a way to feel close!

And my dear family, I would like to thank my mum, father, and sister, who always believed in me. Thank you from the bottom of my heart for being the most supportive and loving family I could ever wish for!

It is not the strongest species that survive, nor the most intelligent, but the one more responsive to change.

Charles Darwin

Abstract

In vitro models mimic the tissue-specific anatomy and play essential roles in personalized medicine and disease treatments. As a sophisticated manufacturing technology, 3D printing overcomes the limitations of traditional technologies and provides an excellent potential for developing *in vitro* models to mimic native tissue. This thesis aims to investigate the potential of a high-resolution 3D printing technology, melt electrowriting (MEW), for fabricating *in vitro* models. MEW has a distinct capacity for depositing micron size fibers with a defined design. In this thesis, three approaches were used, including 1) extending the MEW polymer library for different biomedical applications, 2) developing *in vitro* models for evaluation of cell growth and migration toward the different matrices, and 3) studying the effect of scaffold designs and biochemical cues of microenvironments on cells.

First, we introduce the MEW processability of $(AB)_n$ and $(ABAC)_n$ segmented copolymers, which have thermally reversible network formulation based on physical crosslinks. Bisurea segments are combined with hydrophobic poly(dimethylsiloxane) (PDMS) or hydrophilic poly(propylene oxide)-poly(ethylene oxide)-poly(propylene oxide) (PPO-PEG-PPO) segments to form the $(AB)_n$ segmented copolymers. $(ABAC)_n$ segmented copolymers contain all three segments: in addition to bisurea, both hydrophobic and hydrophilic segments are available in the same polymer chain, resulting in tunable mechanical and biological behaviors. MEW copolymers either support cells attachment or dissolve without cytotoxic side effects when in contact with the polymers at lower concentrations, indicating that this copolymer class has potential in biological applications. The unique biological and surface properties, transparency, adjustable hydrophilicity of these copolymers could be beneficial in several *in vitro* models.

The second manuscript addresses the design and development of a melt electrowritten competitive 3D radial migration device. The approach differs from most of the previous literature, as MEW is not used here to produce cell invasive scaffolds but to fabricate an *in vitro* device. The device is utilized to systematically determine the matrix which promotes cell migration and growth of glioblastoma cells. The glioblastoma cell migration is tested on four different Matrigel concentrations using a melt electrowritten radial device. The glioblastoma U87 cell growth and migration

increase at Matrigel concentrations 6 and 8 mg mL^{-1} In the development of this radial device, the accuracy, and precision of melt electrowritten circular shapes were investigated. The results show that the printing speed and design diameter are essential parameters for the accuracy of printed constructs. It is the first instance where MEW is used for the production of *in vitro* devices.

The influence of biochemical cues and scaffold designs on astrocytes and glioblastoma is investigated in the last manuscript. A fiber comprising the box and triangle-shaped pores within MEW scaffolds are modified with biochemical cues, including RGD and IKVAV peptides using a reactive NCO-sP(EO-*stat*-PO) macromer. The results show that astrocytes and glioblastoma cells exhibit different phenotypes on scaffold designs and peptide-coated scaffolds.

Zusammenfassung

In-vitro-Modelle sind Werkzeuge, die die gewebespezifische Anatomie nachbilden und eine wesentliche Rolle in der personalisierten Medizin und bei der Behandlung von Krankheiten spielen. Als hochentwickelte, multifunktionale Fertigungstechnologie überwindet der 3D-Druck die Grenzen herkömmlicher Technologien und bietet ein hervorragendes Potenzial für die Herstellung von *In-vitro*-Modellen. Der 3D-Druck ist eine der vielversprechendsten Techniken, um biologische Materialien in einer komplexen Anordnung zusammenzusetzen, die das natürliche Gewebe nachahmt.

In dieser Arbeit soll das Potenzial der hochauflösenden 3D-Drucktechnologie melt electrowriting (MEW), für die Herstellung von *In-vitro*-Modellen untersucht werden. Wir konzentrieren uns auf drei Ansätze: 1) die Erweiterung der MEW-Polymerbibliothek für verschiedene biomedizinische Anwendungen, 2) die Entwicklung von *In-vitro*-Modellen zur Bewertung des Zellwachstums und der Zellmigration in Richtung der verschiedenen Matrizes und 3) die Untersuchung der Auswirkungen von MEW-Gerüstdesigns und biochemischen Faktoren der Mikroumgebung auf Zellen.

Zunächst haben wir die MEW-Verarbeitbarkeit von segmentierten $(AB)_n$- und $(ABAC)_n$-Copolymeren vorgestellt, die eine thermisch reversible Netzwerkformulierung auf der Grundlage physikalischer Vernetzungen aufweisen. Bisurea-Segmente werden mit hydrophoben hydrophobic poly(dimethyl siloxane) (PDMS) oder hydrophilen poly(propylene oxide)-poly(ethylene oxide)-poly(propylene oxide) (PPO-PEG-PPO) Segmenten kombiniert, um die $(AB)_n$ segmentierten Copolymere zu bilden. Segmentierte $(ABAC)_n$-Copolymere enthalten alle drei Segmente: Zusätzlich zu den Bisurea-Segmenten sind sowohl hydrophobe als auch hydrophile Segmente in derselben Polymerkette vorhanden, was den segmentierten $(ABAC)_n$-Copolymeren abstimmbare mechanische und biologische Eigenschaften verleiht. MEW-Copolymere unterstützten entweder die Anhaftung an Zellen oder lösten sich ohne zytotoxische Nebenwirkungen auf, wenn sie in niedrigeren Konzentrationen mit ihnen in Berührung kamen, was darauf hindeutet, dass diese Copolymerklasse über umfassende biologische Eigenschaften verfügt. Die einzigartigen biologischen Eigenschaften und Oberflächeneigenschaften, die

Transparenz und die einstellbare Hydrophilie dieser Copolymere könnten in verschiedenen *In-vitro*-Modellen von Vorteil sein.

Das zweite Manuskript befasst sich mit einem durch MEW hergestellten wettbewerbsfähigen 3D-Radialmigrationsdesign. Der Ansatz unterscheidet sich vom Großteil der MEW-Literatur, da MEW nicht zur Herstellung von invasiven Zellgerüsten verwendet wurde, sondern zur Herstellung eines *In-vitro*-Designs diente. Das Design wurde verwendet, um systematisch die Matrix zu bestimmen, die die Zellmigration und das Wachstum von Glioblastomzellen fördert. Die Migration der Glioblastomzellen wurde auf vier verschiedenen Matrigel-Konzentrationen unter Verwendung einer durch MEW hergestellten Radialvorrichtung getestet. Das Wachstum und die Migration der Glioblastomzellen U87 nahmen bei Matrigelkonzentrationen von 6 und 8 $mg\ mL^{-1}$ zu. Wir untersuchten auch die Genauigkeit und Präzision der durch MEW erzeugten Kreisformen. Die Ergebnisse zeigten, dass die Druckgeschwindigkeit und der Designdurchmesser wesentliche Parameter für die Genauigkeit der gedruckten Konstrukte sind. Die Arbeit ist die erste Studie, die MEW für die Herstellung von *In-vitro*-Modellen verwendet.

Im letzten Manuskript wurde der Einfluss von biochemische Funktionalisierung in Kombination mit Gerüstdesigns auf Astrozyten und Glioblastome untersucht. Die kastenförmigen und achteckigen MEW-Gerüste wurden mit biochemischen Wirkstoffen modifiziert, darunter RGD- und IKVAV-Peptide unter Verwendung von reaktivem NCO-sP(EO-*stat*-PO). Wir fanden heraus, dass Astrozyten und Glioblastomzellen unterschiedliche Phänotypen auf den verschiedenen Designs und mit Peptiden beschichteten Gerüsten aufweisen.

Abbreviations

2D	Two dimensional
3D	Three dimensional
4D	Four dimensional
AAB	Aspiration-assisted bioprinting
AFM	Atomic force microscopy
Al	Aluminum
AM	Additive manufacturing
ANOVA	One-way analysis of variance
Ar	Argon
BSA	Bovine serum albumin
CAN	Crimped acupuncture needle
CaP	Calcium phosphate
CM	Conditional medium
CTCs	Circulating tumor cells
CTS	Critical translational speed
D_A	Actual maximal circular diameter
D_{ACC}	Printing accuracy
DAPI	4′,6-diamidino-2-phenylindole
D_D	Designed diameter
DMEM	Dulbecco's Modified Eagle Medium
dsDNA	Double stranded DNA
D_T	Top layer diameter
ECM	Extracellular matrix
EV	Extracellular vesicles
F/CaP	Fluorinated calcium phosphate
FCS	Fetal calf serum
FITC	Fluorescein isothiocyanate
GBM	Glioblastoma multiforme
GelMA	Gelatin methacrylamide
HAMA	Hyaluronic acid methacrylate
HAN	Hanging acupuncture needle
HEPES	(4-(2-hydroxyethyl)-1-piperazineethanesulfonic acid)
hOBs	Primary human osteoblasts
IKVAV	Ile-Lys-Val-ala-Val
L929	Murine fibroblast cell line
LF	Lactoferrin
LVE	Linear viscoelastic
MEM	Minimum essential media
MES	Melt electrospinning
MEW	Melt electrowriting
MFP	Molecular force probe
MRI	Magnetic resonance imaging
MSC	Mesenchymal stem cells

N_2	Nitrogen
NaOH	Sodium hydroxide
NCO-sP(EO-stat-PO)	Isocyanate-terminated poly(ethylene oxide-stat-propylene oxide)
NEAA	Non-essential amino acid
nHA	Nanosized crystals hydroxyapatite
O_2	Oxygen
OB	Osteoblasts
PCL	Poly(ε-caprolactone)
PDMS	Poly(dimethylsiloxane)
PEG	Poly(ethylene glycol)
PLA	Polylactic acid
PLA-PEG-PLA	Poly(lactide-block-ethylene glycol-block-lactide)
PLGA	Poly(lactic-co-glycolic) acid
plMSCs	Placenta-derived mesenchymal stem cells
PPO-PEG-PPO	Poly(propylene oxide)-poly(ethylene oxide)-poly(propylene oxide)
PS	Polystyrene
PVC	Poly(vinyl chloride)
PVDF	Poly(vinylidene difluoride)
RGD	Arg-Gly-Asp
ROX	Roxithromycin
RT	Room temperature
SEM	Scanning electron microscopy
SrBG	Strontium-substituted bioactive glass
Ti	Titanium
T_i	Inward tilting index
U87	Human primary glioblastoma cell line
USPIO	Ultrasmall superparamagnetic iron oxide
UV	Ultraviolet
WP	Whey protein
WST-1	Tetrazolium dye
η*	Complex melt viscosity

List of Publications

As the first author:

1. **Bakirci E**, Schaefer N, Dahri O, Hrynevich A, Strissel P, Strick R, Dalton PD, Vilmann C.
   Melt Electrowritten *In Vitro* Radial Device to Study Cell Growth and Migration.
   Advanced Biosystems 4, no. 10 (2020): 2000077.

2. **Bakirci E**, Frank A, Gumbel S, Otto PF, Tessmer I, Schmidt HW, Dalton PD.
   Melt Electrowriting of Amphiphilic Physically Crosslinked Segmented Copolymers.
   Macromolecular Chemistry and Physics, (2021): 2100259.

As a co-author:

3. Wieland A, Strissel PL, Schorle H, **Bakirci E**, Janzen D, Beckmann MW, Eckstein M, Dalton PD, Strick R.
   Melt Electrowritten Scaffold Tracts Reveal Enhanced Durotaxis and RHOB Dependent Amoeboid Migration of Brain and Breast Cancer Cells with PTEN Loss of Function.
   Cancers 2021, 13(20), 5144

4. Fischhaber N, Faber J, **Bakirci E**, Dalton PD, Budday S, Villmann C, Schaefer N.
   Spinal Cord Neuronal Network Formation in a 3D printed Reinforced Matrix - a Model System to study Disease Mechanisms.
   Advanced Healthcare Materials, (2021):202100830.

5. Kim J, **Bakirci E**, O'Neill K, Hrynevich A, Dalton PD.
   Fiber Bridging during Melt Electrowriting and the Influence of Fiber Diameter and Wall Height.
   Macromolecular Materials and Engineering 306, no. 3 (2021):2000685.

6. Mechau J, Frank A, **Bakirci E,** Gumbel S, Jungst T, Giesa R, Groll J, Dalton PD, Schmidt HW.
   Hydrophilic $(AB)_n$ Segmented Copolymers for Melt Extrusion-Based Additive Manufacturing.
   Macromolecular Chemistry and Physics 222, no. 1 (2021): 2000265.

7. Grosshaus C, **Bakirci E,** Berthel M, Hrynevich A, Kade JC, Hochleitner G, Groll J, Dalton PD.
   Melt Electrospinning of Nanofibers from Medical-Grade Polycaprolactone with a Modified Nozzle.
   Small 16, no. 44 (2020): 2003471.

8. Janzen D, **Bakirci E,** Wieland A, Martin C, Dalton PD, Villmann C.
   Cortical neurons form a functional neuronal network in 3D printed reinforced hydrogel.
   Advanced healthcare materials 9, no. 9 (2020): 1901630.

9. Schaefer N, Janzen D, **Bakirci E**, Hrynevich A, Dalton PD, Villmann C.
3D Electrophysiological Measurements on Cells Embedded within Fiber Reinforced Matrigel.
Advanced healthcare materials 8, no. 5 (2019): 1801226

Table of Contents

1. Introduction

Tissue engineering and regenerative medicine is an interdisciplinary field that intends to produce function for damaged/diseased tissues or organs [1]. Different cell types, biomaterials, and stimulatory signals have been investigated for their potential to support tissue repair and regeneration and recreate the extracellular space through scaffolds and matrices [2]. Furthermore, advances in engineering, material, and cell technologies allow various possibilities for the precise manipulation and control of cells and cellular environments [3].

As the field develops, tissue engineering has a noticeable impact on other disciplines, such as cancer research, enabling three-dimensional (3D) tumor/tissue models of increased complexity that more closely resemble living tissue dynamics [4]. Therefore, tissue engineering is playing a broad yet critical role in the development of new and improved *in vitro* models and therapies [5].

1.1. *In vitro* models

In vivo, cells are immersed in a complex 3D microenvironment formed of extracellular matrix (ECM) components, biological factors, and other adjacent cells [6]. Cells are continuously spreading, migrating, proliferating, differentiating, and interacting with each other and their surroundings in response to biological cues in their environment. Since two-dimensional (2D) cell cultures, which are commonly used in cell-based assays, are simple, they are used as high throughput solutions for various biomedical research applications [7]. However, since the 1970s, researchers have been aware of the limits of 2D cultures compared to 3D cultures [8]. 2D cell culture models can not reflect the anatomical and metabolic complexity of native tissues and organs; they may produce misleading and non-predictive results [9]. Hence, animal testing is often performed after 2D cell culture investigations or before clinical trials. Furthermore, animal models are time-consuming, costly, and have ethical concerns, so it is essential to base these on relevant data [10].

On the other hand, 3D *in vitro* models offer the ability to replicate the microcellular environment and cell-cell interactions accurately in laboratory conditions. Recent studies have identified and characterized 3D matrices essential

for cell attachment and accurate reproduction of the cellular microenvironment [11]. They have led to the generation of living tissue from a cell source. There is also the possibility of modeling various tissue *in vitro* or having a particular impact on the study of various diseases [12]; however, it is difficult to obtain accurate animal models. Ideally, 3D *in vitro* models will allow researchers to better study the safety and efficacy of different biochemical agents, such as drug development, and modeling biological processes such as tissue development before starting animal testing [3].

Various 3D fabrication techniques have been used to create 3D *in vitro* models [13] with the high spatial and temporal resolution, including soft lithography, microfluidics, and additive manufacturing (AM) (Figure 1). These techniques better control biological processes that govern tissue regeneration and mimic the cellular microenvironment [3].

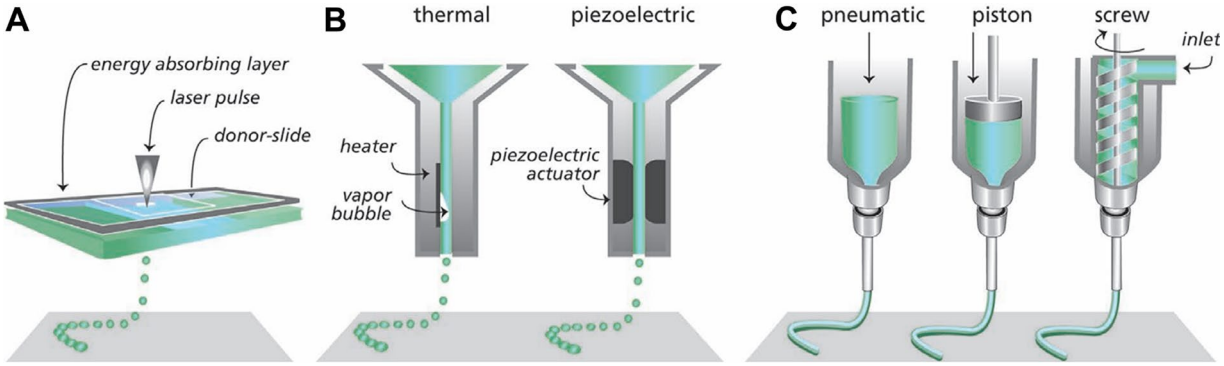

Figure 1. Major additive manufacturing techniques. A) Laser assisted printing, B) inkjet printing C) extrusion-based printing. Published by John Wiley & Sons Ltd. Reproduced from [14] with permission. Copyright 2013, The Authors, published by Wiley.

From a tissue engineering perspective, AM has proven to be an effective strategy in several areas, including the fabrication of organs on chips, cancer research, and pharmaceutical engineering [15]. AM offers rapid free-form prototyping capabilities that enable relatively fast and cost-effective living tissue constructs in regenerative medicine [16]. In addition, the large surface area of 3D-printed fiber scaffolds can promote cell attachment, cell growth, and diffusion of nutrients, as well as intracellular communication, which is another advantage of AM over conventional methods [17]. Two primary AM technologies are currently used for tissue engineering: the fabrication of cell-laden 3D scaffolds, where the cells are encapsulated in a matrix (termed bioink), and scaffolds that can be populated with

cells after fabrication. For the second approach, several techniques can successfully fabricate the scaffolds: Inkjet printing, microextrusion, melt electrowriting (MEW), and laser-assisted bioprinting [18, 19].

The thesis presents critical considerations in high-resolution printing of *in vitro* models, including selecting material and designing the spatial pattern of cell types and scaffold properties. In addition, this thesis reviews recent successes with 3D printed *in vitro* models based on several different fabrication techniques, especially with respect to MEW.

1.2. The melt electrospinning (MES) process

Melt electrospinning (MES) is an electrohydrodynamic fiber manufacturing technology. A polymer melt is ejected towards the collector when applying an electrical potential difference between a nozzle and collector. MES fabricates randomly oriented fibers similar to solution electrospinning using the mechanism of electrostatic repulsion and bending instabilities in the fluid [19]. The resolution limits of other extrusion processes, which are due to die swell, can be overcome with MES technology. Fiber formation occurs from the cooling of polymer melts and allows manufacturing continuous ultrafine fibers that create a thin nonwoven construct with a low micron architecture. MES fiber diameters have been adjusted by changing pressure, polymer molecular weight, temperature, applied voltage, and nozzle to collector distance [20].

Numerous polymers can be processed by MES, including polylactic acid (PLA) [21], poly(ethylene terephthalate) [22], Poly(ε-caprolactone) (PCL) [23], poly(lactic-*co*-glycolic) acid (PLGA) [24], and polypropylene [25]. MES offers a high surface-to-volume ratio while keeping or even improving flexibility compared to other technologies. These characteristics make melt electrospun fibers highly capable for various applications such as air and water filtration [26], separation of water/oil and air/oil mixtures [27], the development of lithium-air batteries [28], optical sensors [29], textiles [30], and biomedical applications such as tissue engineering [31], drug delivery [32], and the diagnosis and treatment of cancer [33].

1.2.1. The principle of MES

As mentioned previously, the molten polymer is extruded through the nozzle. The electrostatically charged polymer droplet at the tip of the nozzle expands to form a conical shape called the Taylor cone [34]. Then, the intensity of the electric field reaches a specific critical value; the electrostatic forces overcome the surface tension of the polymer melt and force the ejection of the liquid jet from the tip of the Taylor cone. The liquid jet is ejected uniformly, and the surface tension causes the droplet shape to relax again. The molten jet expands and solidifies before reaching the collector, resulting in a randomly oriented, non-woven mesh of thin polymer fibers on the collector [35]. At first, the molten jet follows a linear trajectory, but at a critical distance from the nozzle, the jet begins to deflect chaotically, called bending instability [36]. At the beginning of this instability, the jet follows a diverging spiral trajectory. Higher-order instabilities become apparent while the jet spirals towards the collector, leading to a completely chaotic trajectory [37].

MES does not have an evaporation step before deposition on the collector, resulting in a generally larger fiber diameter than solution electrospinning. MES was actually considered for a long time as unable to produce fine diameter fibers. Therefore, our group investigated how the MES fiber size can be reduced to the nanoscale using a modified nozzle, and results showed that the fiber had the lowest diameter of 275 ± 86 nm [38]. The modified nozzle was assembled by inserting an acupuncture needle into a flat-tipped nozzle with two different fixation methods: hanging acupuncture (HAN) and crimped acupuncture needle (CAN) (Figure 2). Different protrusion of acupuncture needles has effects on fiber size. The results showed that 1-mm protrusion had the lowest fiber size and consistency, with electric field simulations increasing with more protrusion.

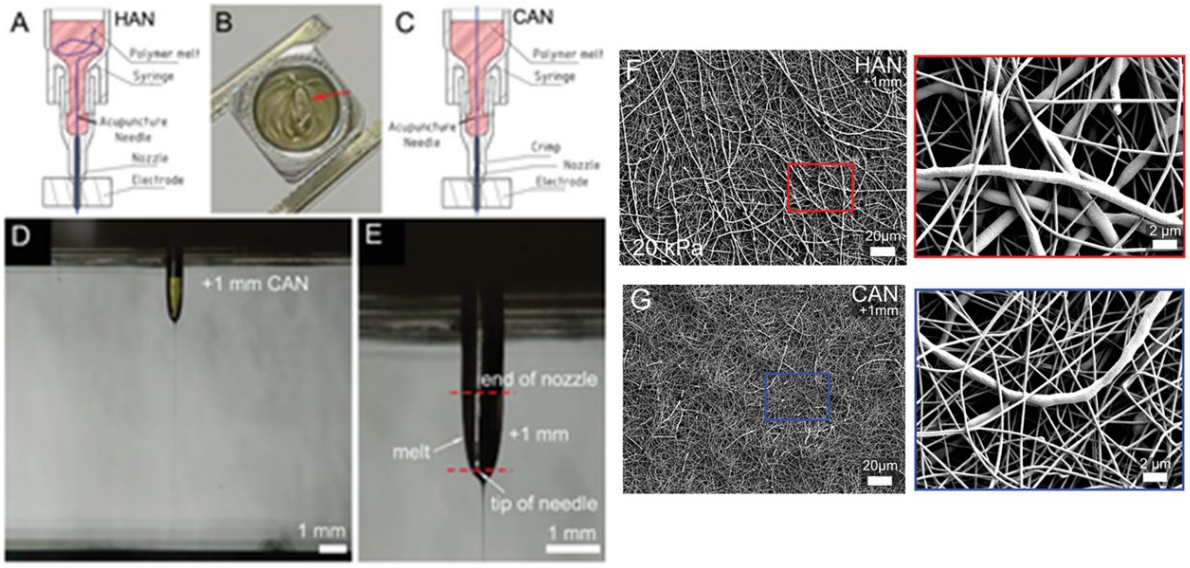

Figure 2. The modified nozzle set-up A) A schematic of a hanging acupuncture needle (HAN), made by B) bending the needle (red arrow). C) A crimped acupuncture needle (CAN), pliers were used for crushing the nozzle into the needle for fixation. D) The acupuncture needle (false-colored yellow) protrudes from the nozzle, and E) the polymer melt flows over the sharp tip surface. F) HAN and G) CAN samples show a similar increase in fiber diameter at 20 kPa. Reproduced from [38] with permission. Published by John Wiley & Sons Ltd. Licensed under the Creative Commons CC BY.

1.3. Melt electrowriting (MEW)

MEW is a hybrid technology that adopts advantages from both MES and melt extrusion AM (Figure 3) [39]. Without electrical instabilities (i.e., whipping), the molten jet of MEW deposits accurately on the collector, and with the help of a computer-aided translating collector, the desired 3D structures can be built up layer by layer. MEW is also solvent-free that provides an advantage to solution electrospinning since volatile and toxic solvents can be avoided.

The MEW process has the unique ability to deposit micron-sized fibers with ordered and predefined structures. The molten polymer is extruded through the nozzle, supplied with high voltage, and deposited on the collector, with predefined patterns via G-codes. The jet can be controlled by the printing parameters, including high voltage, temperature, pressure, translational collector speed, and working distance [40].

Sub-micron fiber diameters can be produced, but typical MEW fiber diameters range between 2 and 50 µm [41]. The different laydown patterns, interfiber spacing, and fiber diameter can impact the various properties, which make MEW constructs attractive for biomedical, tissue engineering, and microfluidic applications [42].

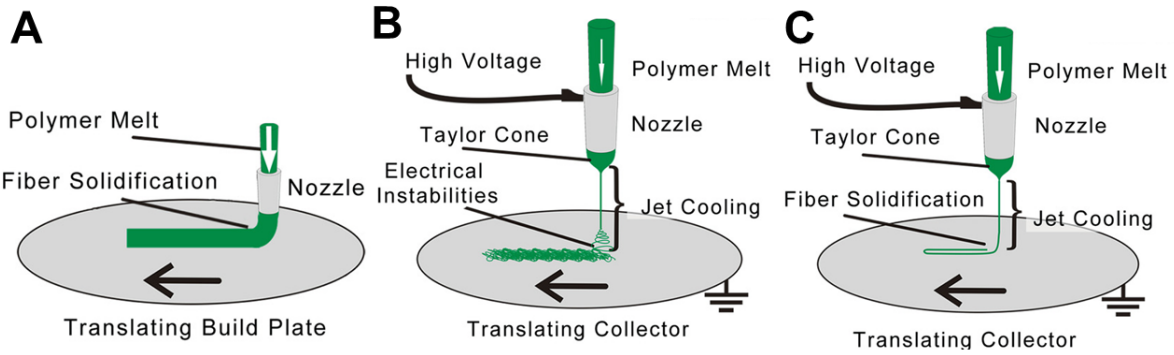

Figure 3. MEW is a hybrid technology combining extrusion 3D printing and melt electrospinning (MES). A) Extrusion 3D printing is extruded a large fiber diameter due to the die swell. B) MES, the molten polymer is extruded through the nozzle. The electrostatically charged polymer droplet at the tip of the nozzle expands to form a conical shape called the Taylor cone. The liquid jet ejected uniformly, and the surface tension caused the droplet shape to relax again. As a result, the molten jet expands and solidifies before reaching the collector, resulting in a randomly oriented, non-woven mesh of thin polymer fibers. C) MEW does not have electrical instabilities due to lower applied high voltages, short collector distance. MEW extrudes predefined patterns via G-codes. Reproduced from [43] with permission. Published by John Wiley & Sons Ltd. Licensed under the Creative Commons CC BY.

1.3.1. MEW process stability

The main process parameters for a highly regulated and reproducible MEW process were examined and found as the mass flow rate, collector speed, and electric field. In addition, the viscosity and charge of liquids determine the molten polymer characteristics. These parameters should be in harmony to achieve a stable jet, which in turn allows the production of large volumetric and highly oriented constructs. Therefore, researchers have made an effort to investigate the influence of MEW processing parameters such as collector speed, collector distance, pressure, and applied voltage on fiber diameter. The investigation of various parameters started with Brown *et al.* [44], and it continued with Hochleitner *et al.* [40]. Recently,

Dayan *et al.* [45] used response surface methodology to predict fiber diameter from collector speed, collector distance, and pressure. Finally, Mieszcanek *et al.* [46] utilized machine vision to correct and detect fiber pulsing for accurate jet placement on the collector. In addition, jet angle and Taylor cone area were monitored and analyzed to better understand, control, and predict jet instabilities.

1.3.1.1. Mass flow to the nozzle

The applied pressure and voltage are the critical parameters for stable mass flow rate in MEW. If the mass flow rates are not adjusted, the diameter oscillates in a sectional manner called “fiber pulsing” [40]. In MEW, fiber pulsing significantly affects the quality of printing. Therefore, pressure and voltage should be in equilibrium for high-quality printing and is one of the first criteria to control printing with MEW.

1.3.1.2. Critical translation speed

The second criteria, direct writing of straight fibers with MEW, is possible when the collector speed is higher than the jet speed, called the critical translation speed (CTS). The fiber can be stretched to obtain smaller diameters in the submicron range when operating well above this CTS. However, when processing below this CTS value, non-linear patterns such as side loops, eight shapes, and sinusoidal can be observed due to jet buckling.

1.3.1.3. Residual charges

The effect of residual charges also affects MEW. In the MEW process, the positive charges are transferred from the nozzle to the polymer jet; after the jet lands on the collector, the charge can be dissipated through the coronal discharge and charge removal by humidity. After deposition, partial charges, called residual charges, remain in the deposited fibers because of the semiconductive nature of molten polymers that can hold charges at a steady state. Residual charges that could not be transferred to the collector can remain on the solidified fibers and affect how subsequent fibers are deposited. The effect of the electric field has been studied on fiber diameter, but more recently, researchers have explored the effect of residual charges on fiber alignment. Ding *et al.* developed a mathematical model representing

residual charge as a tradeoff for tight control of ordered fiber alignment under the new MEW paradigm to fabricate engineered scaffolds with precise control over structural properties [47]. Chang's research group extended their research to better understand charge-based effects in the MEW process by revealing and explaining the effect of collector temperature on the extent of polarization and residual charge amount. As known, the MEW fiber has both positive and negative charges, which are spatially separated due to the polarization effect, resulting in a side-by-side attraction and repulsion between the fibers. Choosing the right collector temperature makes it possible to print scaffolds with different wall morphologies, induce or avoid different forms of disorder, and even control the internal structure within a fiber wall [48]. Our group also did a fundamental study to identify and determine the fabrication limit of MEW (Figure 4). We investigated the minimum interfiber distance between different diameter fibers and their stacking height. The results showed that the material of the collector, the fiber diameter, and the number of layers affect the limit of interfiber spacing [49].

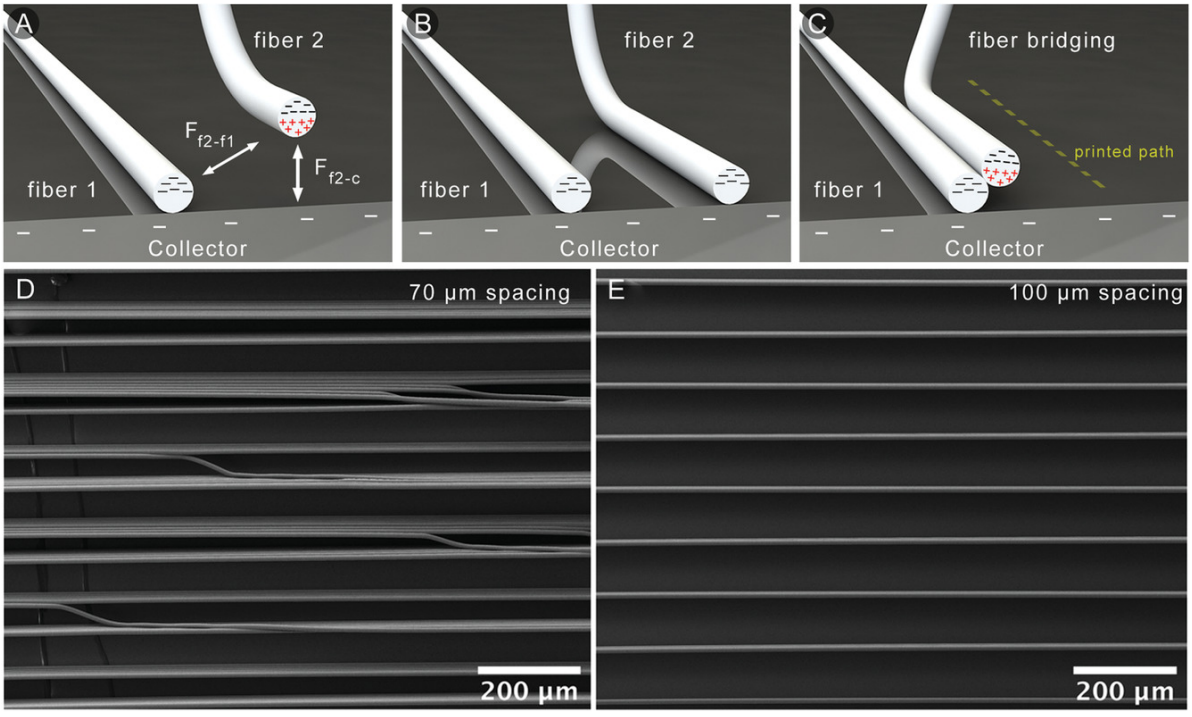

Figure 4. Fiber bridging during MEW process. A–C) Illustration of how the deposited fiber can be attracted to the already landed fiber, the force between the fiber and the collector (F_{f2-c}) must be more significant than the force between the two fibers (F_{f2-f1}). Scanning electron microscopy (SEM) images demonstrate D) fiber bridging at a 70 µm inter-fiber distance and

E) no attraction at 100 µm interfiber distance. Reproduced from [49] with permission. Published by John Wiley & Sons Ltd. Licensed under the Creative Commons CC BY.

1.3.2. MEW on non-planar surfaces

MEW is mainly performed on planar (flat) collectors and tubular mandrels. However, there is a growing interest in fabricating anatomically relevant scaffolds using different collector shapes. First, Saidy *et al.* performed MEW on an aortic root-shaped collector. Next, they used different collectors made of composite materials, such as pure Aluminum (Al), Aluminum-Titanium (Al-Ti), and Aluminum- poly-lactic acid (Al-PLA), for the stable jet. MEW performed on the Al-Ti collector resulted in unstable printing conditions such as long beading and pulsing due to inhomogeneity of the electrical field compared to the Al collector [50]. Later, Peiffer *et al.* investigated the effect of different collector geometries on printing accuracy. They showed that the electrical properties of materials have a more significant impact on accurate fiber deposition than the thickness of the collector [51]. They also proved that maintaining the electrostatic force constant and uniform (z-correction) to the collector surface is essential for accurate deposition of microfibers, which supports the results of Saidy *et al.* [50].

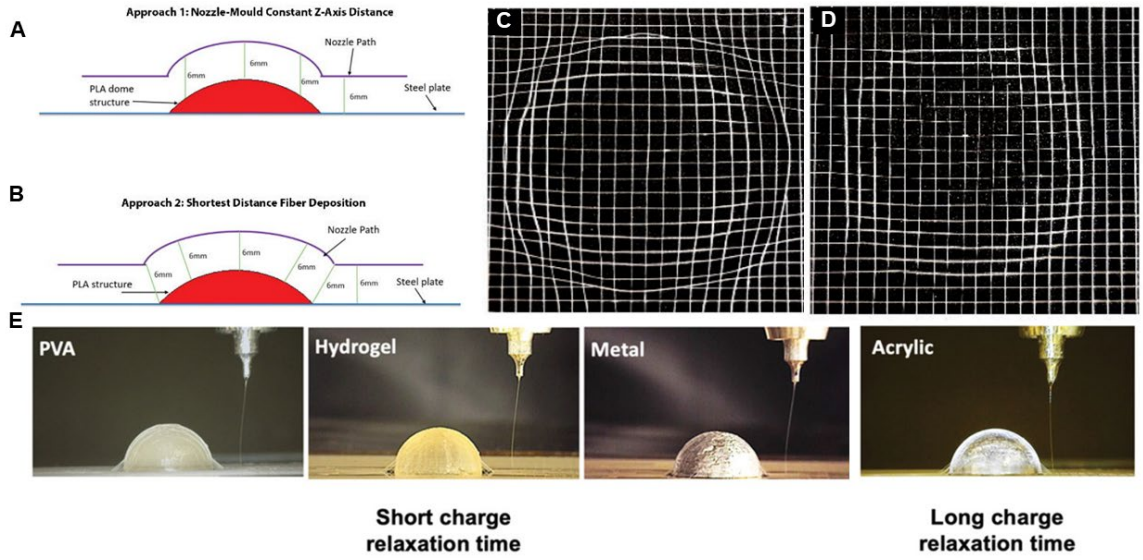

Figure 5. Different approaches for increasing accuracy of fiber deposition on non-flat surface PLA mold. A) Schematic map of coordinates generated via MATLAB code, B) illustrating vertical height adjustment for the accuracy of the fiber deposition using the shortest distance between the nozzle tip and curved surface, C-D) images of the patches with close up of edge

regions represent attraction between fiber walls and inaccurate deposition and accurate fiber deposition [52, 53]. E) Images of the experiment during printing that demonstrate deflected MEW jet in the surrounding hemispheres made from polyvinyl alcohol, hydrogel, metal, and acrylic. The jet and the degree of deflection are similar to each other—acrylic hemisphere repels rather than attracts MEW jet [54]. Reproduced from [52-54] with permission. Copyright 2021, The Authors, published by Wiley. Published by John Wiley & Sons Ltd. Licensed under the Creative Commons CC BY [52].

Recently, O'Connell *et al.* systematically investigated the effects of various parameters on fiber deflection toward hemispherical collectors. They presented a simple physical framework describing the horizontal electrostatic deflection force as a geometric phenomenon [54]. The amount of deflection depends on the object's size and charge relaxation time collector materials and not on the applied voltage or fiber diameter (Figure 5E). Furthermore, the publication from Monaghan Group examined the effects of various parameters such as collector materials (PLA and Al), topography, and nozzle positioning onto curved collectors on print quality [52]. The collector materials have a significant effect on MEW fiber deposition. The deposition of fibers on a curved PLA dome was successful, but only when a uniform vertical height was maintained alongside a constant electrostatic force (Figure 5A-D). Based on the electrical properties of the collector materials, it was found that the less conductive, the greater the amount of charge remains in the polymer fibers resulting in a repulsion. Repulsion of the PCL fibers resulted from uneven stacking of PCL fiber walls. It was observed more in 90% PLA infill rather than a 10% PLA infill. These results extend the design library of MEW for printing more anatomical shape structures.

1.4. Polymers

Different polymers can be processed via MEW. PCL, however, is the gold standard polymer due to its low melting point (60°C) and slow thermal/hydrolytic degradation. The absorbability and biocompatibility of PCL, as well as its rheological and viscoelastic properties, semi-crystallinity, and rapid solidification, make it a promising material for MEW. Other than PCL, different polymers processed with MEW include poly(vinylidene difluoride) (PVDF) [55], polypropylene [56], poly(L-Lactide) [57], poly(2-ethyl-2-oxazoline) [58], and poly(urea-siloxane) [59]. The

extended MEW polymer library is essential for being able to use MEW for different applications. Our group has put effort into extending the MEW polymer library. Table 1 shows some of the polymers used in MEW in recent years.

Table 1: Different Polymers processed with MEW and their applications

Polymers	Applications	References
Piezoelectric polymers: PVDF, Poly(vinylidene Fluoride-Co-Trifluoroethylene),	Biomedical materials, flexible electronics	[60],[55], [61]
Poly(2-ethyl-2-oxazoline)	Water soluble hydrogel	[58, 62]
PCL within poly(2-ethyl-2-oxazoline-*co*-2-(3-butenyl)-2-oxazoline)	Dissolveable channel, microfluidic	[63]
Poly(L-lactide-*co*-ε-caprolactone)	Flexible medical device	[57]
Poly (L-lactic acid)	Bone tissue engineering	[64]
Polypropylene	Surgical mesh, sutures	[63]
Isomalt	Microfluidic	[65]
Poly(L-lactide-co-ε-caprolactone-co-acryloyl carbonate)	Tissue engineering	[66]
Poly(ε-caprolactone-co-acryloyl carbonate)	Ligament and Tendon tissue engineering	[67]
Poly(urea-siloxane)s; thermoplastic elastomer	Microfluidic. Tissue engineering,	[43, 59]
Polyurethanes	Wearable devices, anti-adhesion textiles and wound dressings.	[68]

1.4.1. Composite polymers used in MEW

Composite materials were used in MEW due to the increased biocompatibility and mechanical properties of MEW constructs. For example, PCL and hydroxyapatite composites were MEW-processed for bone tissue engineering. The hydroxyapatite

composites were included 3 and 7% in PCL, and the homogeneity of distribution of hydroxyapatite nanoparticles is a crucial element for avoiding blocking of the jet and continuous fiber writing. In addition, the melt electrospun composite scaffolds increase cell growth, and both PCL and composite fibers demonstrated excellent cell infiltration into the scaffolds [69]. In addition, Paxton *et al.* were able to melt electrowrite combination of 33 wt% strontium-substituted bioactive glass (SrBG) and PCL using chloroform. The composite materials have beneficial properties of the bioactive SrBG, such as mechanical properties, and the PCL, such as MEW processability [70].

Milk proteins containing PCL were melt electrowritten for skin regeneration. Lactoferrin (LF) and whey protein (WP) with 0.05%, 0.1%, 0.25%, and a combination of them 0.25 each were used as an additive to PCL. MEW constructs were assessed chemically, physically, and biologically *in vitro.* In addition, keratinocytes and human dermal fibroblasts were used as cell components. The results demonstrated that LF (0.25%) containing scaffolds and a combination of LF and WP scaffolds significantly increased cell growth, spreading, and infiltration compared to PCL alone. Thus, the approach can be helpful for deep tissue dermal regeneration [71].

Furthermore, a triblock copolymer of poly(lactide-block-ethylene glycol-block-lactide) (PLA-PEG-PLA) was used with solid 45S5 bioactive glass. The PLA-PEG-PLA blend with 10% PLA showed promising printing results in terms of scaffold shape fidelity. In comparison, the addition of 5% solid bioactive 45S5 glass particles had no adverse effects on printing and processing ability [72].

Mueller *et al.* examined the use of PCL scaffolds loaded with ultrasmall superparamagnetic iron oxide (USPIO) nanoparticles to improve magnetic resonance imaging (MRI) visualization [73]. The results showed that MEW 3D printed composite scaffolds containing up to 0.3 wt% USPIOs can be identified *in vitro* using T2- and T2*-weighted MRI. Furthermore, the incorporation of USPIO with PCL did not affect the mechanical properties and cytocompatibility of PCL. Concentrations as low as 0.26 wt% resulted in no decrease of tensile strength and elastic modulus. In addition, cytocompatibility tests revealed excellent cell viability, with proliferating cells adhering

to all scaffolds. In addition to contributing to the MEW material library, this study offers the prospect of longitudinal MRI monitoring of MEW grafts.

In addition, PCL/PEG/roxithromycin(ROX) composite scaffolds were fabricated using MEW for bone tissue engineering. The addition of PEG and ROX improved the hydrophilicity of PCL. Also, *in vitro* drug release tests showed that the PCL/PEG/ROX scaffolds have an initial explosive release of the drug followed by a long-term sustained release, which is favorable for preventing and treating bone infections. Furthermore, the antibacterial assays showed that the composite scaffold with ROX has effective antibacterial activity. Human osteoblast-like cells on the scaffolds had good viability and growth, proven by immunostaining and metabolic activity assay [74].

Yoshida *et al.* reported composite melt electrowritten PCL/chitosan scaffolds with controlled pore microarchitecture and their effects on human bone-marrow-derived mesenchymal stem cells (MSC) proliferation and migration. In addition, 1 wt% chitosan blend formulation and scaffold microarchitecture promoted cellular activity compared to other blends [75].

In conclusion, the literature about MEW composite polymers depends on hydroxyapatite, bioactive glass, PEG, and magnetic particles loaded PCL. Also, recently biopolymers were blended into PCL to improve the biocompatibility of polymer [75]. Mostly, PCL was used as the primary material due to its excellent printability.

1.5. Surface coating

The polymers used in MEW are hydrophobic thermoplastics that cause non-specific protein absorption and subsequent uncontrollable cell adhesion. Therefore, MEW fibers can be post-processed with other materials to make them more hydrophilic using plasma treatment, sodium hydroxide (NaOH) etching, and various polymer coatings. Mostly, MEW fibers are coated with cell attractive materials such as calcium phosphate, collagen, fibronectin, and conductive materials.

The MEW fiber surface was functionalized for different applications such as pro-adipogenic cell delivery vehicles, cartilage, and bone tissue engineering to produce a bioactive surface for cells. For example, Hammerl *et al.* cocultured osteoblasts (OB) and peripheral blood mononuclear cells on calcium phosphate (CaP) coated PCL [76]. The *in vitro* system was an excellent example of a cost-effective and growth factor-free *in vitro* platform. In addition, the CaP coated MEW scaffolds better mimic the physiological microenvironment of the regenerating bone niche. Daghrery *et al.* were utilized to fluorinated calcium phosphate (F/CaP) coated MEW scaffolds for promoting the proliferation of cells and helping periodontal tissue regeneration while providing antimicrobial protection [77]. Also, Abbasi *et al.* showed that CaP coated MEW scaffolds are quite stable for bone regeneration with different pretreatment methods such as O_2 and Ar plasma and NaOH [78].

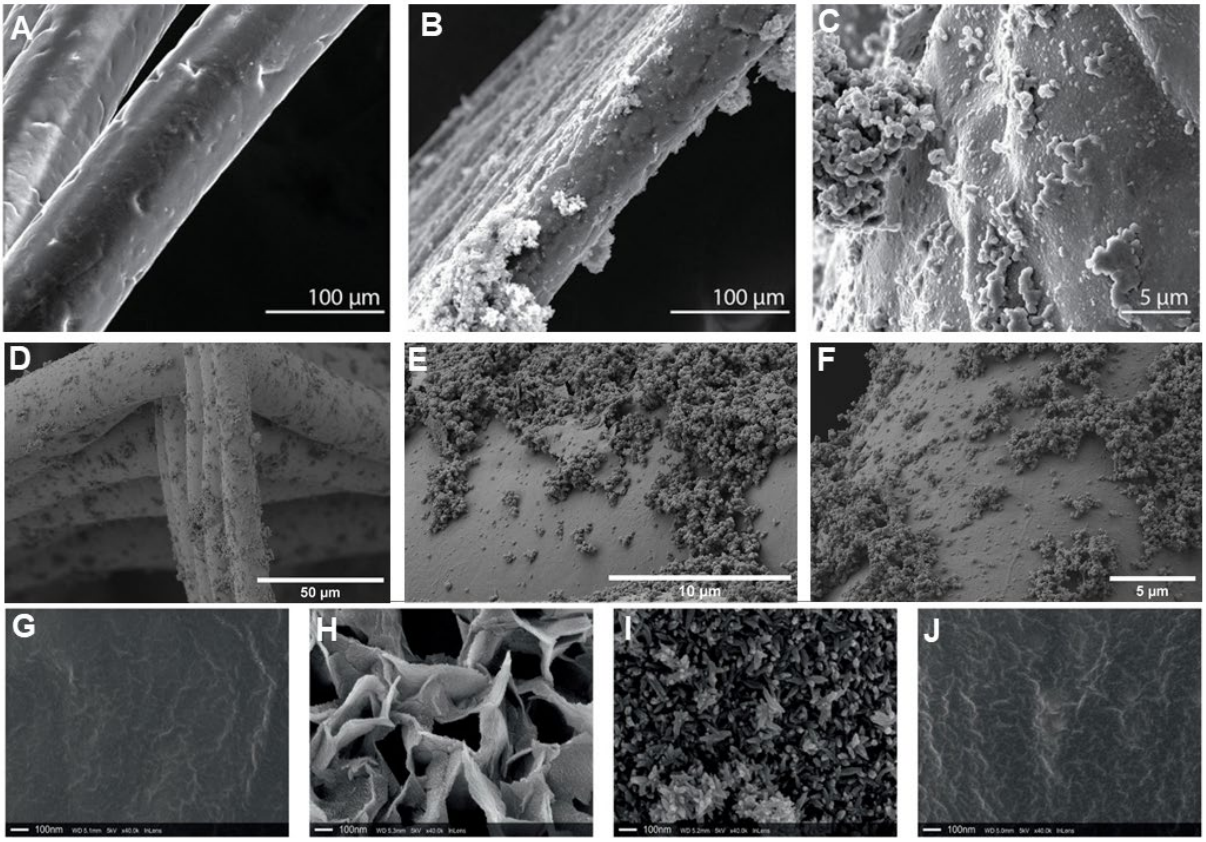

Figure 6. A) SEM image of MEW PCL fibers before coating. Scale bar, 100 µm. B) SEM image of polypyrene-coated fibers. Scale bar, 100 µm. C) Higher magnification SEM image of the polypyrene-coating particles. D-F) Biomineralization of PCL fiber with polydopamine (unpublished data) G-J) SEM imaging of PCL, plate-shaped, nanoneedle-shaped crystals, and intrafibrillar dispersed scaffolds groups, respectively. Reproduced from [79] and [80] with permission. A-C, G-J) Copyright 2020, The Authors, published by Wiley.

Furthermore, Eichholz *et al.* utilized a novel bioinspired extrafibrillar coating of needle-shaped nanosized crystals hydroxyapatite on MEW fiber to enhance MSC osteogenesis. Moreover, extrafibrillar coatings of nanoneedles facilitated the binding, stabilization, and controlled release of bone morphogenetic protein 2 from the material, which further enhanced MSC cell proliferation and bone formation (Figure G-H-I-J) [80]. In addition, the same group coated MEW scaffolds with extracellular vesicles (EV). They have functionalized the scaffolds with nanosized crystals hydroxyapatite [81]. The nanotopographical properties and a large surface area of nanosized crystals hydroxyapatite-coated scaffolds facilitate proteins' stabilization and enhancement of EV adhesion. In addition, the researchers placed the conditional medium (CM) and the isolated EVs in a collagen solution to improve the binding efficiency of the scaffolds further. The staining confirmed the presence of EVs on the fiber surface, both in CM and, to a greater extent, in EV-functionalized scaffolds. Thus, the coating methods provide homogeneous and nano topographical features, which play an essential role in promoting stem cell osteogenesis.

MEW scaffolds were also coated with polypyrene for improving electroconductive properties (Figure 6A-B-C), and they were used as the model for myocardial infarction treatment [79]. Also, the unique scaffold architecture, auxetic shape, was mimicked the anisotropic behavior of the myocardium. MEW-PCL scaffolds were functionalized with graphene oxide and graphitic carbon nitride, enabling optoelectronic transduction and wireless neuronal stimulation in neuritis under visible light [82].

MEW scaffolds were also biofunctionalized. permanently via six-arm star-shaped NCO-poly(ethylene oxide-stat-propylene oxide) (sP(EO-stat-PO)) with the collagen and streptavidin [83]. Furthermore, Blum *et al.* coated PCL MEW scaffolds with a complex ECM suspension of human decellularized adipose tissue, purified fibronectin, or laminin as a model for pro-adipogenic cell delivery platform [84].

In addition, the MEW surface coating was used to adjustable the mechanical behavior of fiber-reinforced hydrogel systems. The PCL was methacrylated, and it serves to have covalent bonding between alginate, gelatin methacrylamide (GelMA),

and PEG diacrylate. Bas *et al.* also developed a design library for tunning the biomechanical and biological properties [85].

In conclusion, there are many ways to coat MEW scaffolds. Moreover, those methods are relatively simple and cost-effective to produce promising systems for cell-material interaction, optic, and biofabrication approaches.

1.6. Soft network composites

Soft network composites have been produced using a wide range of different manufacturing technologies, mainly to increase structural integrity and strength. A combination of hydrogel and reinforcing MEW fibers have been used in several studies. The purpose of reinforcing MEW fiber into soft matrices is to increase the mechanical properties of soft hydrogels and improve the cell proliferation and alignment along fibers that mimic the ECM microenvironment.

MEW-reinforced matrices provide multiple possibilities for soft tissue regeneration and engineering. The matrices alone are very soft materials; increasing the crosslinker content, or molecular weight makes them more robust but compromises cell proliferation, migration, and differentiation within the hydrogels. The reinforced matrices meet the required mechanical properties to mimic the function of the fibrous ECM soft matrices.

MEW fiber-reinforced matrices were used for different matrices and tissue types. GelMA is one of the most used hydrogels for MEW reinforced matrices. The first publication with MEW reinforced GelMA was published in 2015 for musculoskeletal tissue engineering application [86]. The MEW reinforced hydrogels have 50 times increase in mechanical behavior compared to hydrogel alone. Following that, numerous research groups used MEW fiber-reinforced matrices to mimic the anisotropic mechanical behavior of tissues in a variety of applications, including the heart [87], multiphasic articular cartilage [51], and bone [88].

Mathematical homogenization theory was utilized to develop effective equations to understand how the applied force is distributed throughout the MEW fiber-reinforced scaffolds. The resulting model captures the orthotropic nature of the

composite and can be used to determine how the local mechanical environments are subjected depends on the MEW reinforced hydrogels [89]. In a complementary approach, Castilho *et al.* used a finite element model to investigate the strengthening mechanisms of fiber-hydrogel constructs [90]. According to their results, the load-carrying capacity of the fiber scaffold interconnections dominated the reinforcement mechanism at higher scaffold volume fractions. In addition, hydrogel provides significant resistance against buckling of the scaffold that was higher than expected based on simple tests of MEW scaffolds.

Furthermore, another computational study employed a numerical model to determine the design of a most biomechanically optimal scaffold to mimic multiphasic properties of articular cartilage. This pilot study also yielded a complete in silico design library to aid in selecting optimal fiber–hydrogel network for tissue engineering applications. This approach can be improved efficiency, cost, and effort on manufacturing and experimental testing of scaffold designs [85]. Finally, de Ruijter *et al.* demonstrated that out-of-plane MEW fibers precisely designed to stabilize an existing structure.The design increased the shear modulus of MEW reinforced hydrogels for improving compressive strength [91].

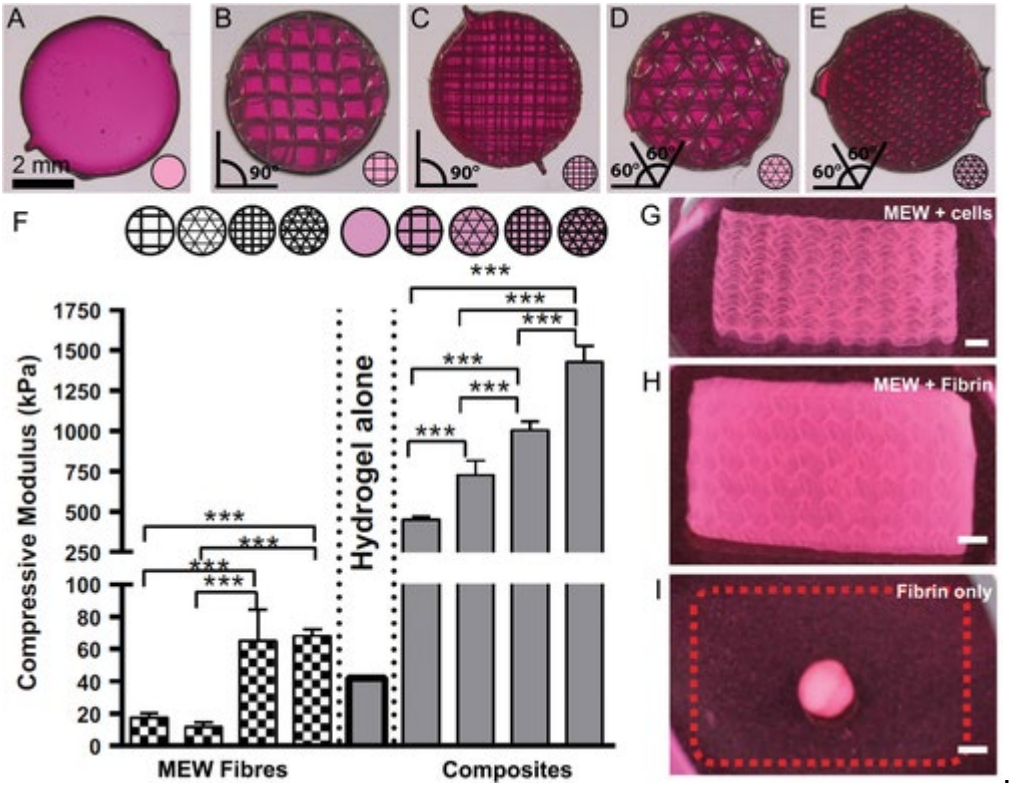

Figure 7. Various MEW fiber reinforced hydrogel strategies. MEW fiber reinforced gelatin methacrylamide (GelMA)/hyaluronic acid methacrylate (HAMA) hydrogels, with A) only hydrogel, B) 0°–90° laydown pattern with 800 µm fiber spacing, C) 0°–90° laydown pattern with 400 µm fiber spacing, D) 0°–60°–120° laydown pattern with 800 µm fiber spacing and E) 0°–60°–120° laydown pattern with 400 µm fiber spacing F) Demonstration of MEW scaffold designs and their compression modulus only and within a GelMA/HAMA hydrogel. Sinusoidal MEW scaffolds support the G) seeding of cells and H) reinforced of fibrin, images taken after two weeks. I) The fibrin hydrogel shrinks when similarly cultured for two weeks. The dashed line defines the original size of the fibrin. Scale bar = 2 mm. Reproduced from [42, 92, 93] with permission. A-F) Copyright 2015, The Authors, published by Elsevier [92]. G-I) Copyright 2019, The Authors, published by Wiley [42, 93].

1.7. Tissue engineering applications

Due to high water content, various matrices have been used in tissue engineering and regenerative medicine to mimic the ECM microenvironment. In addition, their tunable physicochemical properties, such as the components of growth and differentiation factors, can significantly impact cell activity. However, their

structures are not as mechanically robust as the ECM of soft tissues, which contains fibrous proteins. Their lack of mechanical instability also hinders adequate cellular function. Mechanical strength can be improved by increasing the polymer concentration or the degree of crosslinking in the hydrogel, but this may adversely affect cell survival, proliferation, migration, and differentiation, as previously mentioned in the soft network composite session. Highly organized MEW fiber can be reinforced inside the different matrices, which have adjustable mechanical properties to mimic the ECM of soft tissues.

The workflow of this concept, printing the MEW scaffold and embedding inside the soft matrices. Different matrices such as alginate, GelMA, Matrigel were used for different tissue applications. The first study, Visser *et al.*, showed that the stiffness of GelMA and alginate matrices could be increased by MEW fiber reinforcing to 50 and 15-fold, respectively, compared to matrix only. The stress-strain curves of reinforced GelMA closely match healthy articular cartilage values. Furthermore, the stiffness of the biodegradable composites was equivalent to the stiffness of articular cartilage, which has been reported to vary between 400 and 800 kPa [86]. Next, Bas *et al.* investigated the effect of different scaffold designs on the mechanical behavior of reinforced GelMA and GelMA/hyaluronic acid-methacrylamide (HAMA). The only GelMA and GelMA/HAMA composites exhibited a low Poisson's ratio because highly organized fiber networks suppressed the lateral deformation of the hydrogel (Figure 7) [92].

Furthermore, the MEW reinforced matrices were used in cardiac tissue engineering. The hexagonal scaffolds with a 20-40 times higher ability to absorb and release energy than rectangular scaffolds reinforced encapsulated collagen-based matrices. *In vitro* models show an increase in beating frequency (1.5-fold), improved the human induced pluripotent stem cells derived cardiomyocytes alignment, sarcomere content and organization, and an increase in expression of markers related to cardiac maturation compared with fiber scaffolds [94].

The collaboration work with Villmann lab focused on nerve tissue engineering using MEW reinforced soft matrices. For this purpose, the cortical neuron, mouse primary spinal cord neurons, glycine receptor-transfected Ltk-11 mouse fibroblast cell

line, glioblastoma, and coculture of astrocytes and neurons were used within MEW reinforced Matrigel (Figure 8).

The first study focused on enabling fast readouts from transfected cells, which are often used as model systems for 2D electrophysiology [95]. This study used MEW scaffolds with different porosity reinforced Matrigel, and 3D electrophysiology was performed on the glycine receptor-transfected Ltk-11 mouse fibroblast cell line. The second study used the MEW scaffold reinforcement to adapt this technique to cortical neurons without affecting electrophysiological measurements [96]. The results showed that cortical neurons enhance cell survival and 3D neural network development by dendritic and synapses maturation over 21 days *in vitro,* which is faster in 3D cells than 2D cultures. Furthermore, with its tremendous flexibility in MEW scaffold design and soft matrix composition, this method provided a novel tool for investigating neural networks in 3D under normal and disease conditions.

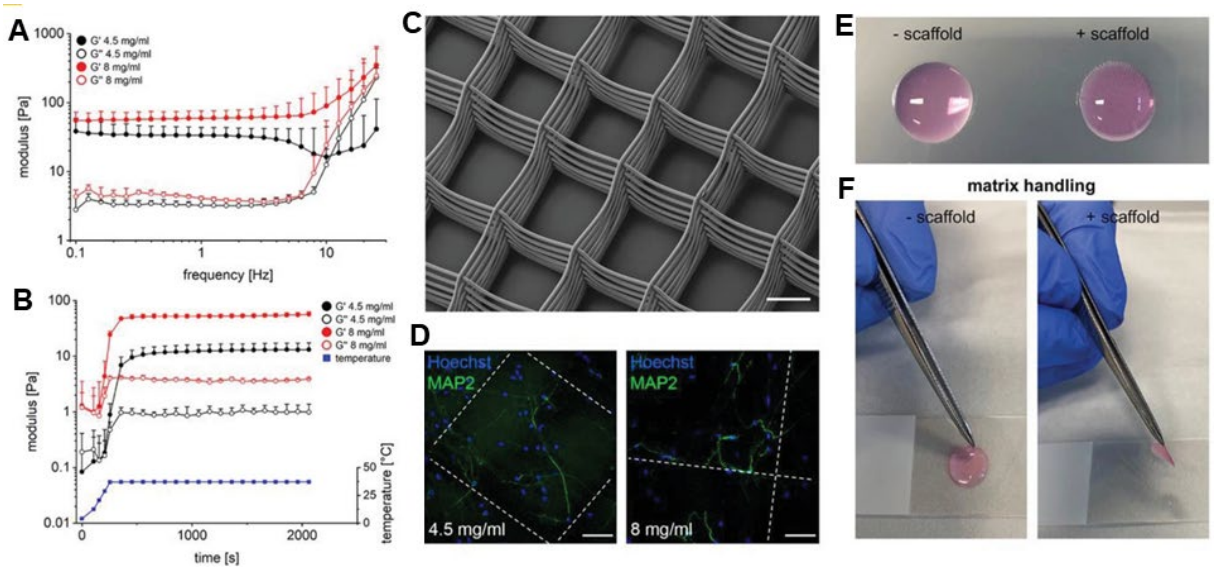

Figure 8. Rheological characterization of Matrigel at concentrations of 4.5 and 8 mg mL^{-1} . A) Frequency sweep and B) time sweep. C) SEM image of melt electrowritten scaffolds with a fiber spacing of 200 µm. D) Cortical neurons in MEW reinforced Matrigel concentration of 4.5 and 8 mg mL^{-} at day 7. E) Matrigel alone (left) and MEW scaffold reinforced Matrigel (right) F) Handling properties of Matrigel alone (left) and MEW scaffold reinforced Matrigel (right). Reproduced from [96] with permission. Published by John Wiley & Sons Ltd. Licensed under the Creative Commons CC BY.

The last study evaluated the neural network development of mouse primary spinal cord neurons in MEW fiber-reinforced Matrigel [97]. Maturation of inhibitory

glycinergic synapses was analyzed by protein expression, complex mechanical properties, calcium imaging. In 3D, the mature inhibitory synapse formed more rapidly than in 2D, confirmed by a significant increase in glycine receptor expression from days 3 and 10. The expression pattern of marker proteins at the inhibitory synapse and the mechanical properties in 3D were similar to native spinal cord tissue. Moreover, the neuronal networks of the 3D spinal cord showed intense neuronal activity after 14 days in culture.

In summary, the MEW scaffolds used in those studies provide mechanical support for weak matrices, which can be comparable to the native brain and spinal cord microenvironment and allow sufficient handling to study different neural cells in healthy and disease models.

Together, fiber-reinforced GelMA, alginate, collagen, and Matrigel have been used in musculoskeletal, cardiac, and nerve tissue engineering. The fiber-reinforced hydrogels have a synergistic effect for mimicking the microenvironment mechanically and also enhancing the biochemical properties of ECM.

1.8. Hybrid/solution 3D direct writing

Different AM techniques have their benefits and drawbacks; therefore, combining them brings endless possibilities for producing hierarchical structures for tissue engineering. MEW was combined with different AM techniques for this purpose. For instance, 3D *in vitro* device was fabricated combining 3D extrusion printing and MEW, which facilitates cell-specific alignment. It differs from the two-step fabrication of the device, which required printing a MEW scaffold and then embedding a cell-loaded hydrogel, which limited control over the precise deposition of multiple materials and cells. First, Ruijter *et al.* combined MEW with bioprinting to produce a soft network composite. GelMA was used as bioink, and MSCs were used as cell components; they printed MEW PCL fiber on bioprinted GelMA (Figure 9C-D) [98]. The mechanical properties composited did not change; however, this approach precisely controls 3D spatial organization, which better mimics the native cell microenvironment. Next, Diloksumpan *et al.* combined ceramic extrusion 3D plotting and the MEW of thermoplastic materials. The study has a novel approach to

mechanically integrate hydrogel-based soft tissues to stiff ones for the regeneration hard-to-soft tissue interface, especially for osteochondral plugs [99]. Recently, Ross *et al.* developed a platform for combined hydrogel and melt electrowritten scaffold for articular cartilage regeneration. They produced the alginate methylcellulose and MEW PCL multi-material scaffolds for tailored mechanical properties. They demonstrated long-term shape fidelity and mechanical stability of hybrid scaffolds, and the MEW PCL scaffolds support large volumetric prints [100].

The other hybrid approach was to use MEW with solution electrospinning to mimic vascular structures [101]. Hierarchical two-layer tubular scaffolds consisted of a randomly oriented dense solution electrospun mesh as the inner layer and a melt electrowritten fiber as the outer layer. Scaffolds were seeded with endothelial colony-forming cells and MSCs. The results show that scaffolds provide biomimicry morphology for both cell types without surface functionalization, only using a hybrid scaffold design.

On the other hand, MEW scaffolds were used for the assembly of different spheroids. The study extended [41], and MEW scaffolds were used as a support structure for adipose spheroids, which can be sectioned, stained, and handled efficiently (Figure 9B) [102].

Recently, MEW was utilized with inkjet printing. PLGA and gelatin mixture was electrowritten, and cytokine-bearing microspheres were accurately loaded onto the MEW scaffolds using inkjet printing. *In vivo* results showed that the scaffolds promoted cartilage repair [103].

Lastly, Wang *et al.* fabricated a micro/macro hierarchical scaffold by combining MEW and solution electrospinning for bone tissue engineering. The solution electrospinning gelatin nanofibers make the scaffolds hydrophilic, slightly increase the mechanical strength, and support the growth of 3D bone cells. In addition, MEW scaffolds increase cell adhesion efficiency and improve cell proliferation and osteoinductivity [104].

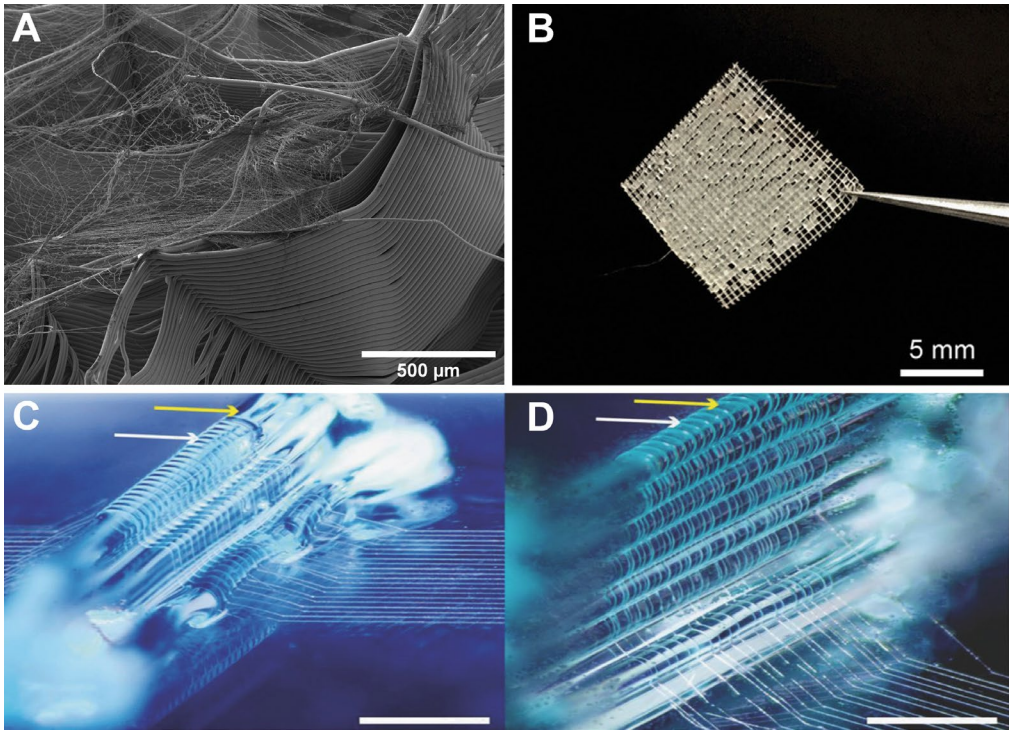

Figure 9. A) PVDF solution electrospun fiber on 1000 µm fiber spacing MEW PCL scaffolds (Unpublished data) B) Bioassembly of tissue spheroid into MEW scaffolds. Copyright 2019, The Authors, published by Wiley C- D) and out-of-plane fiber deposition. Yellow arrows depict the hydrogel, whereas the white arrows depict the PCL fiber. Scale bar = 500 µm. Copyright 2018, The Authors, published by Wiley. Reproduced from [98, 102] with permission. Published by John Wiley & Sons Ltd. Licensed under the Creative Commons CC BY.

1.9. MEW fiber studies

MEW scaffolds exhibited tunable mechanical properties changing the design parameter, such as fiber diameter and interfiber spacing wavelength, making them attractive for different tissue engineering applications.

First of all, MEW fabricated constructs with different patterns which resemble the wavelike structure of native collagen fibers to mimic the anisotropy and viscoelastic properties of native heart valve leaflets. In addition, the MEW scaffolds provided the growth of human vascular muscle cells [50]. Finally, the scaffolds showed good acute hydrodynamic performance under aortic physiological conditions in a flow circuit, a promising design approach for heart valve tissue engineering.

Another study used the machine learning methodology to focus on the mechanosensory response of cells on MEW scaffolds which served as an essential step towards developing bioinformatics-driven AM systems. In addition, this approach can be used for more homogenous cell responses from biomaterials [105].

Different pore size scaffolds were utilized as sandwich models for the model of the intervertebral disc. The results showed that MEW scaffolds were helpful for quantitative assays, and the model has successfully measured cell migration, expansion, and proliferation [106]. Differently, the effects of heterogeneous porous architectures of MEW scaffolds on osteogenic gene expression were investigated. *In vitro* results showed that the gradient scaffolds significantly increased alkaline phosphatase activity in the attached osteoblasts, while matrix mineralization was higher in the 50% offset scaffolds, which was already shown by different MEW studies for bone tissue engineering [107, 108].

Furthermore, a filter device for colon cancer was fabricated using MEW multiphase scaffolds. It had reproducibility and transparency, which facilitate microscopic analysis compared to electrospun filters. Therefore, MEW multiphasic scaffolds offer a rapid expansion of circulating tumor cells (CTCs) for clinically relevant downstream analysis such as nucleic acid composition, downstream drug screening, and treatment screening. The culture device capture the CTCs spread on the filter as single cells or clusters of a few cells, from where they extended into large cancer clusters. Each of the expanded clusters represents one or a few clones of the tumor, facilitating the identification of critical clonal subsets of cancer [109].

Recently, collagen microbundles like fibers were melt electrowritten using sacrificial polymer blended PCL. The scaffolds facilitate cell infiltration and offer an environment that inhibits unnatural apical/basal polarization by providing 3D topographical signals for the infiltrated cells, resulting in efficient M2-like phenotype polarization similar to collagen I fibrils [110].

1.10. Cocultures

MEW scaffolds could be used to mimic the endosteal microenvironment. Primary human osteoblasts (hOBs) and placenta-derived MSC (plMSCs) were

evaluated in nonosteogenic conditions and different surface treatments. The melt electrowritten scaffolds promoted the growth and migration of primary human hematopoietic stem cells (HSCs) compared to HSCs maintained in tissue culture plastic. Also, HOBs and plMSCs synthesized bone matrix on CaP coated MEW platform [111].

1.11. Folding scaffolds

Bioprinting of alginate methacrylate was combined with MEW-PCL to create four-dimensional (4D) printed scroll-like scaffolds with anisotropic topography. Combining these two techniques and materials enabled the fabrication of multiscale and multi-material shape-changing scaffolds that could self-fold after swelling. In addition, researchers were able to control the shape-morphing behavior of the constructs changing calcium ion concentration in the media. Furthermore, myoblasts cultured on these 4D printed bilayer scaffolds demonstrated excellent viability, proliferation, and alignment along melt-electrowritten fibers [112].

The same research group used different materials for the shape-changing biolayer scaffolds. Combining bioprinting of hyaluronic acid hydrogel and MEW PCL-Polyurethane were used for the study. The results show that the soft and elastic properties of the fibers allow excellent biocompatibility and biomimicry for myoblasts [113].

1.12. *In vivo* studies

3D coiled compacted scaffolds with hierarchically ordered patterns and tunable coil densities were fabricated by using MEW. The scaffolds could improve cell growth in patterns with tunable cell density. Subcutaneous implantation in mice showed favorable *in vivo* biocompatibility, as evidenced by no significant increase in tumor necrosis factor α and interleukin 6 levels in mouse serum. A long-range patterned matrix composed of programmable short-range compacted coils facilitates the design of complex structures [114].

Furthermore, Abbasi *et al.* investigated the osteoconductive potential of their previous study *in vivo*. They successfully implanted different MEW scaffolds with

gradient pore sizes into a defect in rats and assessed the effects of the graded architecture on bone formation. The constructs with larger pore sizes, such as 500 µm, and gradient scaffolds have faster bone regenerations. Thus, the results showed that gradient MEW scaffolds might provide an appropriate solution for improving bone regeneration [115].

Recently, in a rat mandibular periodontal fenestration defect model, the F/CaP-coated MEW scaffolds were shown to be biocompatible and led to periodontal regeneration. This work contributes to developing tailored scaffolds capable of facilitating tissue-specific progenitor cell differentiation and thereby guiding simultaneous and coordinated regeneration of soft and hard periodontal tissues while offering antibacterial protection [77].

1.13. Microfluidic technologies

Various techniques are available to fabricate simple suspended hollow structures, the best known of which is soft photolithography for microfluidic purposes. Recently, MEW fibers have been employed as sacrificial materials in a wide range of applications. Using microchannels to improve the function and survival of engineered tissues in regenerative medicine applications is a promising method. A MEW structure is embedded into a soft cross-linkable hydrogel solution and then removed post-fabrication, resulting in highly defined hierarchically structure hydrogels. A study by Haigh *et al.* demonstrated that sacrificial PCL templates could be printed via MEW and then easily removed from poly(2-oxazoline) hydrogels using an acetone-water mixture. Using this solvent, PCL could be dissolved, and the hydrogel preserved its swelling to prevent distortion [116]. A hollow, perfusable microchannel within a hydrogel for tissue engineering has attracted significant attention for efficiently transporting oxygen and nutrients. Recently, Isomalt was melt electrowritten for the same purposes [65].

MEW is a fascinating candidate for producing a high aspect ratio channel due to the precision and quality control of the individual MEW patterns. Zeng *et al.* developed a cost-effective and straightforward method for microfluidic channels combining MEW and poly(dimethylsiloxane) (PDMS) replica-molding techniques [117]. Alternatively, Kotz *et al.* used a similar strategy to repeat sacrificial templates in

transparent fused silica to produce arbitrarily embedded 3D free-form hollow microstructures, but the hollow microstructure is formed by a thermal debinding process that passively eliminates the PCL material [118].

In summary, fugitive or sacrificial materials printing with MEW is promising for numerous applications, such as microfluidics, optics and photonics, tissue engineering of vascular networks, and lab-on-a-chip devices.

1.14. Soft robotics

Research into soft robotics using MEW has recently begun, with the publication from the Chen group being the first in this field [119]. Researchers utilized three different techniques: MEW, micro-molding, and skiving to create a mass-produced tadpole-like magnetic PCL/Fe_3O_4 microrobot. The microrobot can be used in two different modes under the external magnetic field rolling and propulsion modes. The speed and direction of the tadpole-like microrobot can be adjusted using different frequencies, intensity, and magnetic field directions. These robots can transport one or more cargo to a predetermined destination in a controllable and precise way. MEW is such a simple and cost-effective manufacturing method for scale-up fabrication and advanced fabrication [119].

Recently, MEW tubular structures were used for the fabrication of the actuator. The design of MEW scaffolds on soft elastomers allows highly controlled deformation characteristics for actuators. The actuator has 10 to 15 mm of length and 1 of mm inner diameter. The motion can reach ~20ms without exploiting snapping instabilities or material non-linearities [120].

Shortly, the use of MEW in soft robotics is promising due to the design capacity of MEW. The fabrication of MEW structures at the nano and microscale results in actuators with precision and reproducibility. In addition, a wide range of design space provides different actuation motions and actuators' simple up-and-downscaling [121].

2. Aim and motivation

The lack of compatibility between *in vitro* and *in vivo* effectiveness of therapies is a critical barrier in the clinical translation of promising medications for the treatment of many diseases. Traditional 2D *in vitro* models frequently struggle to recapitulate the native or diseased tissue microenvironments. Recent research has demonstrated that 3D *in vitro* models, including spheroids, hydrogels, fiber scaffolds, and microfluidic organs on-chip, better simulate the cellular microenvironment than 2D *in vitro* models. Among the various fabrication technologies, 3D printing is one such technique that allows researchers to build 3D *in vitro* tissue models by assembling biological materials in a complex layout that mimics native human tissues. MEW is such a technology that allows high-resolution 3D printing without any toxic solvent. MEW scaffolds are exciting candidates for tissue engineering and regenerative medicine because of their high surface-to-volume ratio; they assist cell attachment and proliferation. The structure, porosity, size, architecture of MEW constructs for different tissues and applications could be adjusted, so they can provide a microenvironment for cell infiltration, cell binding, blood flow, and vascularization.

The overall aim of this doctoral project has been to explore the potential of MEW for the fabrication of *in vitro* models. The first goal has been to systematically characterize the copolymers' printability with MEW for potential applications. Secondly, we developed radial *in vitro* models to evaluate cell growth and migration toward the different matrices and, lastly, study the effect of scaffold designs and biochemical cues of microenvironments on cells. For this purpose, the processibility of new materials with MEW was explored. Also, the printing accuracy and precision of the MEW radial device using different process parameters were investigated. Lastly, the biological properties of MEW scaffolds were improved for more reproducible *in vitro* systems.

3. Results

3.1. Summary of manuscript I

Different $(AB)_n$ and $(ABAC)_n$ segmented copolymers with hydrophilic and hydrophobic segments were processed by MEW. All copolymers showed excellent MEW processability, with unique properties compared to those already processed with MEW, including thermal reversibility, a very smooth surface, transparency, strong interlayer bonding between fibers, and tunable hydrophilic and hydrophobic behavior.

3.1.1. Manuscript I

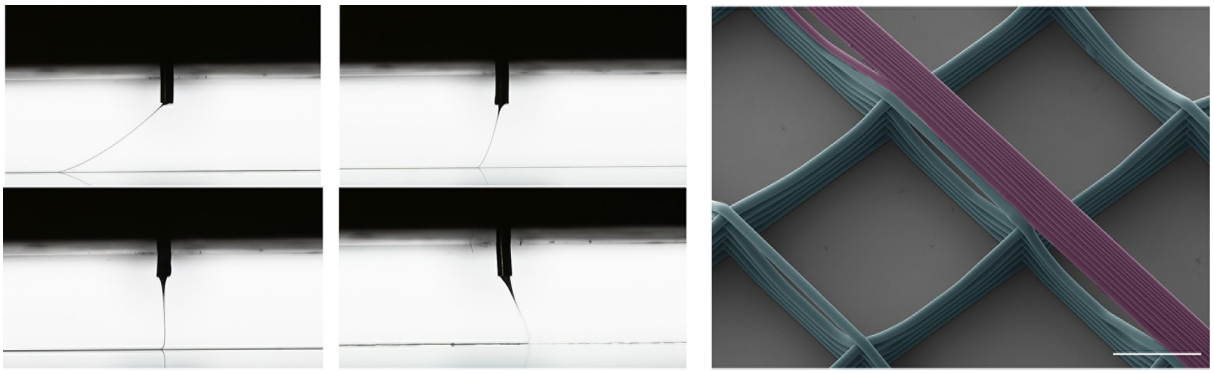

Melt Electrowriting of amphiphilic physically crosslinked segmented copolymers

First published: 30 September 2021 at Wiley Macromolecular Chemistry and Physics

https://doi.org/10.1002/macp.202100259

Melt Electrowriting of amphiphilic physically crosslinked segmented copolymers

Ezgi Bakirci[1], Andreas Frank[2], Simon Gumbel[2], Paul F. Otto[1], Eva Fürsattel[2], Ingrid Tessmer[3], Hans-Werner Schmidt[2] and Paul D. Dalton[1,4]**

E. Bakirci, P. F. Otto, Prof. P. D. Dalton
[1]Department for Functional Materials in Medicine and Dentistry and Bavarian Polymer (BPI) Institute
University Würzburg, Pleicherwall 2, 97070 Würzburg, Germany

A. Frank, S. Gumbel, Dr. E. Fürsattel, Prof. H.-W. Schmidt
[2]Macromolecular Chemistry and Bavarian Polymer Institute (BPI), University of Bayreuth, Universitätsstraße 30, 95440 Bayreuth, Germany
E-mail: hans-werner.schmidt@uni-bayreuth.de

Dr. I. Tessmer
[3]Rudolf-Virchow Center for Integrative and Translational Bioimaging, University of Würzburg, Josef-Schneider-Straße 2, 97080 Würzburg, Germany

Prof. P. D. Dalton
[4]Phil and Penny Knight Campus to Accelerate Scientific Impact, University of Oregon, 1505 Franklin Blvd, 90403 Eugene, OR, USA
E-mail: pdalton@uoregon.edu

Keywords: melt electrowriting, electrohydrodynamic, additive manufacturing, 3D printing

Abstracts

Various $(AB)_n$ and $(ABAC)_n$ segmented copolymers with hydrophilic and hydrophobic segments are processed via melt electrowriting (MEW). Two different $(AB)_n$ segmented copolymers composed of bisurea segments and hydrophobic poly(dimethyl siloxane) (PDMS) or hydrophilic poly(propylene oxide)-poly(ethylene oxide)-poly(propylene oxide) (PPO-PEG-PPO) segments, while the amphiphilic $(ABAC)_n$ segmented copolymers consist of bisurea segments in the combination of hydrophobic PDMS segments and hydrophilic PPO-PEG-PPO segments with different ratios, are explored. All copolymer compositions are processed using the same conditions, including nozzle temperature, applied voltage, and collector distance, while changes in applied pressure and collector speed altered the fiber diameter in the range of 7 and 60 µm. All copolymers showed excellent processability with MEW, well-controlled fiber stacking, and inter-layer bonding. Notably, the surfaces of all four copolymer fibers are very smooth when visualized using scanning electron microscopy. However, the fibers show different roughness demonstrated with atomic force microscopy. The non-cytotoxic copolymers increased L929 fibroblast attachment with increasing PDMS content while the different copolymer compositions result in a spectrum of physical properties.

1. Introduction

Additive manufacturing (AM) technologies have been used for different applications, including soft robotics,[1] sensors,[2] biomaterials,[3,4] and tissue engineering.[4] AM, often referred to as 3D printing, is based on layer-by-layer fabrication principles that are employed by a spectrum of different technologies.[5] Melt electrowriting (MEW) is one such AM technology that uses an applied electric field to produce fine fiber diameters,[6] typically much smaller than 100 μm,[7] and 820 nm at their smallest to date.[8] The high viscosity of polymer melts assists in the reduction in fiber diameter without jet breakup[6] and computer-aided control of the collector direct-writes the desired pattern according to G-codes.[9]

While different polymers can be processed via MEW, poly(ε-caprolactone) (PCL) is the benchmark polymer due to its low melting point (60 °C) and slow thermal/hydrolytic degradation.[10] Beyond PCL, other polymers processed with MEW include poly(vinylidene difluoride),[11] polypropylene,[12] poly(L-lactide-*co*-caprolactone-*co*-acryloyl carbonate),[13] Poly(L-lactide-*co*-caprolactone),[14] poly(2-ethyl-2-oxazoline),[15] poly(ureasiloxane)[16] and poly(urea-ethylene glycol).[17] The majority of polymers processed to date are hydrophobic, which absorb proteins that influence cell adhesion.[18]

Hydrophilic polymers can reduce cell adhesion,[19] recently more and more are available for MEW, which, in turn, aids certain biomedical devices to improve their function.[20] The improved hydrophilic properties can thus result in a significant enhancement in the biocompatibility and functionality of the materials.[21] Within biofabrication, where soluble properties have utility in the formation of perfusable channels, the polymer may need to be water-soluble over time,[22, 23] or on-demand.[24] Additionally, for any application that involves contact with cells, the polymers should be cytocompatible.[25]

Electrohydrodynamically stabilized jets of aqueous-based polymer and macromer solutions have been previously reported,[26, 27] with post-crosslinking required to achieve a hydrogel fiber. When processing via MEW, however, hydrogel fibers are made by printing a melt and then swelling in aqueous media.[7] Since the

preprinting period for MEW requires extrusion through a nozzle, non-crosslinked melts that crosslink after deposition has been developed and reported. There are several ways to achieve this crosslinking, including via UV-light,[13] Diels–Alder chemistry,[15] or using physical crosslinking such as reported with $(AB)_n$ segmented copolymers.[17] The $(AB)_n$ segmented copolymers belong to the class of physically crosslinked hydrogels. These copolymers are based on reversible, non-covalent crosslinks formed by hydrogen bonding, which allows the processing from the melt.[28] The processability of $(AB)_n$ segmented copolymers with MEW provides unique properties due to high-resolution printing and design flexibility, which makes them interesting for optics,[29] microfluidics,[30] flexible electronic devices,[31] and soft network composites[32] in materials science and soft robotics. This study investigated the MEW processability of four different $(AB)_n$ and $(ABAC)_n$ segmented copolymers combined of bisurea, hydrophobic poly(dimethyl siloxane) (PDMS), and hydrophilic poly(propylene oxide)-poly(ethylene oxide)-poly(propylene oxide) (PPO-PEG-PPO) segments (Figure 1). These copolymers have adjustable hydrophilic properties depending on their content of PPO-PEG-PPO segments. Copolymer 1 is hydrophobic due to the PDMS segments, whereas copolymer 4 is hydrophilic due to the PPO-PEG-PPO segments. Copolymers 2 and 3, however, have different hydrophobic and hydrophilic properties depending on PDMS and PPO-PEG-PPO segment contents. $(AB)_n$ and $(ABAC)_n$ segmented copolymers are ideally suited for MEW due to their physical crosslinks reversibly disassemble and assemble upon heating and cooling, respectively. For all copolymers, MEW processing conditions such as molten polymer temperature, applied pressure, voltage, tip to collector distance, and collector speed[28, 29] were systematically investigated, and the fiber diameter was correlated with the pressure and collector speed. The copolymers used in this study have unique properties compared to polymers, which have been already processed with MEW including i) thermally reversibility, ii) a highly smooth surface, iii) transparency, iv) strong inter-layer bonding between the fibers, and v) adjustable hydrophilic and hydrophobic behavior. The morphology, mechanical properties, cytotoxicity, and cell adhesion behavior of the copolymers and the MEW scaffolds were examined.

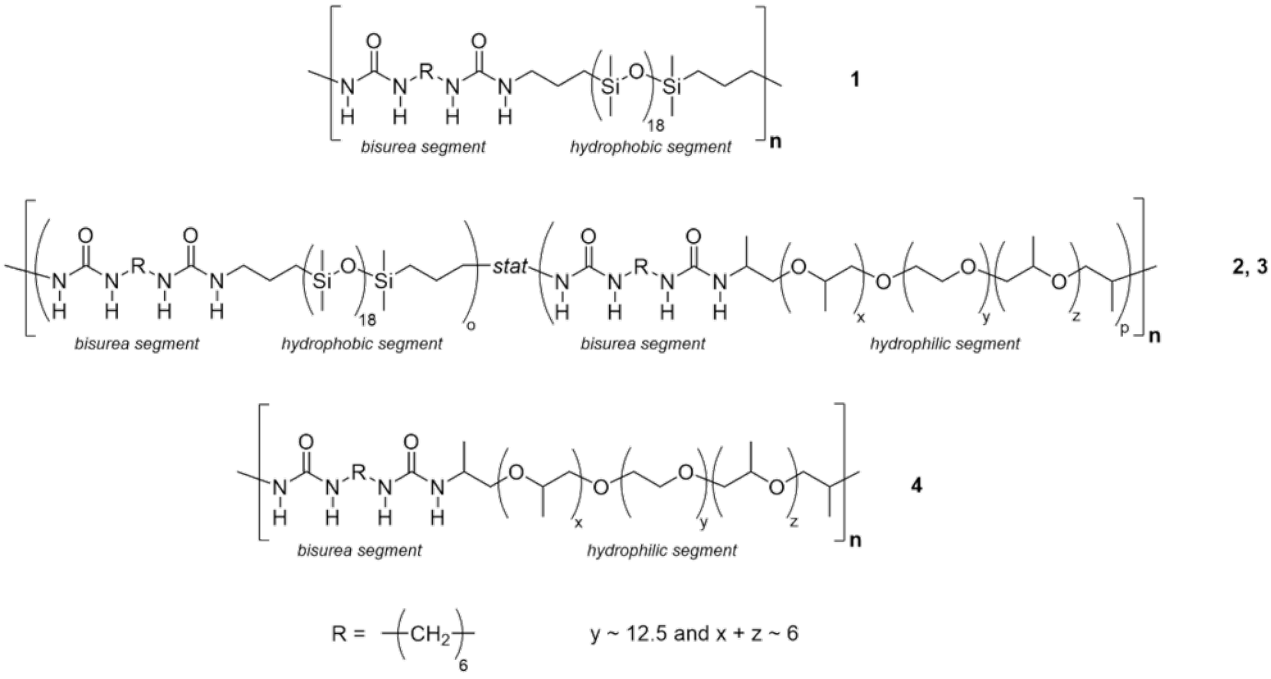

Copolymer No.	Segment content (wt.%)		
	Bisurea	PDMS	PPO-PEG-PPO
1	12	88	0
2	13	80	7
3	15	53	32
4	19	0	81

Figure 1. Chemical structures of the $(AB)_n$ segmented bisurea copolymer 1 and 4, and the $(ABAC)_n$ segmented copolymers 2 and 3. In all cases, the bisurea segments contain a hexamethylene unit. The copolymers differ in the content of the different segments as listed in the table.

2. Results and Discussion

2.1. Copolymer Properties

The $(AB)_n$ segmented copolymers are composed of bisurea segments and hydrophobic PDMS or hydrophilic PPO-PEG-PPO segments (Figure 1). Furthermore, the $(ABAC)_n$ segmented copolymers contain all three segments: besides bisurea, both hydrophobic, and hydrophilic segments are now incorporated in the same polymer chain by varying compositions. The bisurea segment is responsible for the thermoreversible physical crosslinking of the copolymer chains due to the formation

of strong hydrogen bonds. The hydrophobic PDMS segments provide mechanical stability, while water uptake is governed by the hydrophilic PPO-PEG-PPO segments. The hydrophilicity and thus water uptake can be adjusted by varying the ratio of PDMS to PPO-PEG-PPO segments. Extensive details on the polymer synthesis and resulting bulk properties can be found elsewhere.[33]

2.2. MEW Processing

For the successful printing of MEW constructs, the polymer melt viscosity at the processing temperature is an important parameter. Thus, the melt viscosity should be low enough to allow extrusion through the fine nozzle at pressures governed by the experimental setup. As shown in previous studies on similar $(AB)_n$ segmented copolymers,[16, 17] complex melt viscosities are comparable to viscosities obtained by rotational measurements, thus comply with the Cox/Merz relationship. The complex melt viscosity (η^*) for the copolymers 1 to 4 upon cooling from the melt was measured at the MEW processing temperature of 100 °C by oscillatory shear rheology and are depicted in Figure 2. At this temperature, η^* was found in the range between 40 and 500 Pa s, thus suitable for MEW in the existing MEW printer configuration. Upon heating, the physical crosslinks of the urea bonds disaggregate into a viscous melt and, when cooled, the viscosity curves show a sudden increase between 70 and 40 °C. This increase in viscosity is caused by the distinct hydrogen bond reaggregation typical for hexamethylene urea groups. At room temperature for all segmented copolymers, the η^* is around three orders of magnitude higher compared to the values in the melt. Thus, a fast solidification of the printed MEW constructs is expected.

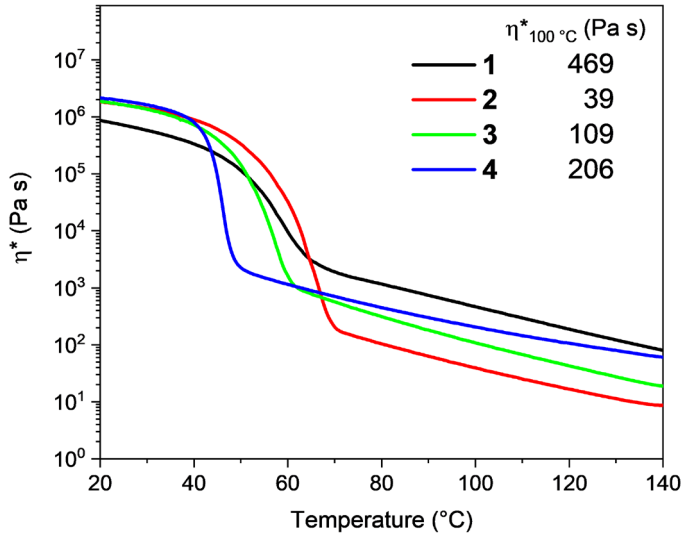

Figure 2. Complex melt viscosity (η*) versus temperature, shown are the first cooling curves of copolymers 1, 2, 3, and 4. Values of η* at the MEW processing temperature of 100 °C are listed also in the plot. (Conditions: oscillating shear rheology utilizing a plate-plate geometry (25 mm) at 1 Hz with a cooling rate of 2 K min^{-1}).

While MEW is a multi-parametric manufacturing technology, which is typically optimized for each polymer, here we aimed to process the four different copolymers under similar conditions. When using identical processing parameters — applied pressure and collector speed included — notably different jet behaviors resulted for copolymers 1 to 4 (Figure 3 and Video S1, Supporting Information). The critical translational speed (CTS) is when the collector speed matches the molten jet speed and is determined experimentally as a straight line [34] of the polymer jet towards the collector as seen for copolymer 3 (Figure 3C). Increasing the collector speed beyond the CTS increases the lag of the jet, as observed for copolymer 1 and 2 in Figure 3A,B, and affects the accuracy of the printed constructs.[35, 36] For copolymer 4, the jet speed is slightly faster than the collector speed and a pronounced heel appears, where the jet moves ahead of the nozzle (black arrow; Figure 3D).

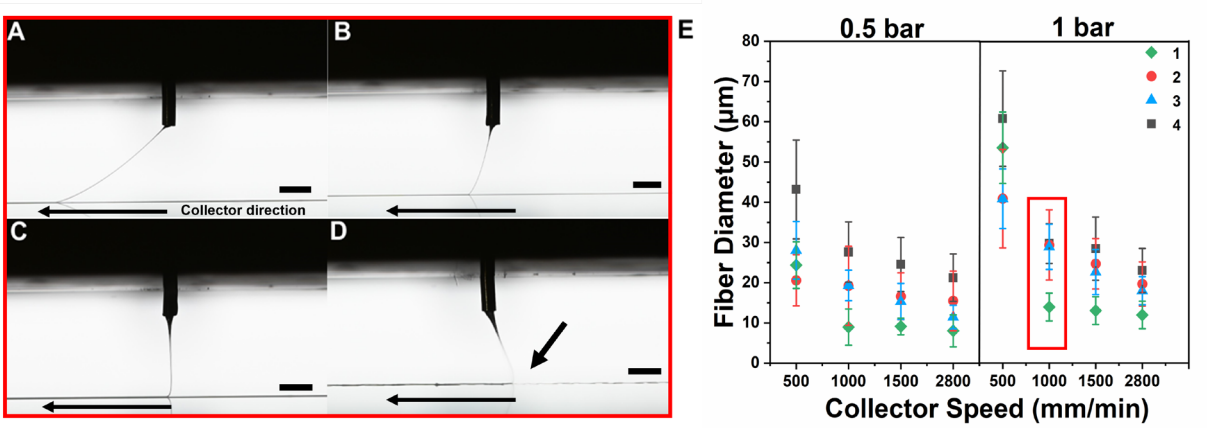

Figure 3. Jet behavior of four different copolymers using the same processing parameter (100 °C, 1000 mm min^{-1}, 1 bar, and 3 kV, see red box on the graph). Copolymers 1 A), B) 2, C) 3 have a typical jet lag which can be seen when the collector speed is faster or equal to CTS, and the fibers are straight; however, copolymer D) 4 has a pronounced "heel" typical when the collector speed is lower than the CTS, and it advances in front of the nozzle and the fibers are non-linear (scale bar:1 mm) (see Video S1, Supporting Information). E) Effect of pressure and collector speed on the fiber diameter for the copolymers 1 to 4 at 100°C of melt processing temperature, 2.2 mm of collector distance, and 3 kV of applied voltage.

Parameters such as applied voltage (3 kV), collector distance (2.2 mm) and melt processing temperature (100 °C) were kept constant for all four copolymers. The influence of the applied pressure and collector speed was investigated and is shown in Figure 3E. The thinnest fiber diameter, 7.6±3.0 µm, was achieved using 2800 mm min^{-1} collector speed and 1 bar for copolymer 1. The thickest fiber diameter was obtained using a low collector speed of 500 mm min^{-1} and 1 bar, which results in 59.0±12.5 µm for copolymer 4. In general, and in line with previous studies for other copolymers,[37] the fiber diameter decreases with increasing collector speed due to the mechanical stretching of the jet. An increase in the pressure also resulted in a thicker fiber diameter due to increased mass in the jet.

The fiber diameter did not significantly reduce at speeds greater than 1500 mm min^{-1} for both applied pressures of 0.5 and 1 bar. The fiber diameter at 1 bar resulted in fiber pulsing with long beading[34] and substantially varied compared to 0.5 bar. Comparing the four copolymers, the viscosity and probably the ratio of PPO-PEG-PPO segments in the copolymer appeared to affect the fiber diameter, with copolymer 4 having the thickest fiber diameter. The CTS of copolymer 4 was also higher than the CTS of the other copolymers. All copolymers generally printed well,

and defined scaffolds could be readily fabricated. The stacking behavior of the fibers was examined using square-shaped 10- and 20-layered constructs (Figure 4 and Figure S1, Supporting Information). As previously reported, copolymer 1 has an accurate and precise stacking behavior[16] while the copolymer 4 has lower shape fidelity compared to other copolymers at the same processing parameters. All other copolymers similarly stacked well; some defects begin occurring after 20 layers (Figure S1, Supporting Information). The copolymers also stacked upon each other with no observable deleterious interactions shown by Figure S2A,B, Supporting Information, wherein copolymer 3 was MEW upon a square design scaffold of copolymer 2. A rationale to research physically crosslinked polymers is that increased self-healing for improved fiber fusion, important for overall mechanics. The various swelling ratios or mechanical behaviors between different copolymers make this of interest for soft robotics. Using similar MEW processing conditions help when potentially switching between different copolymers while using a single nozzle — an approach already adopted within for extrusion direct writing.[38] For the future direction, the multi-material multi-nozzle 3D printing head could be used for MEW and in combination with the adjustable properties of segmented copolymers, very tiny voxelated soft matter can be generated.

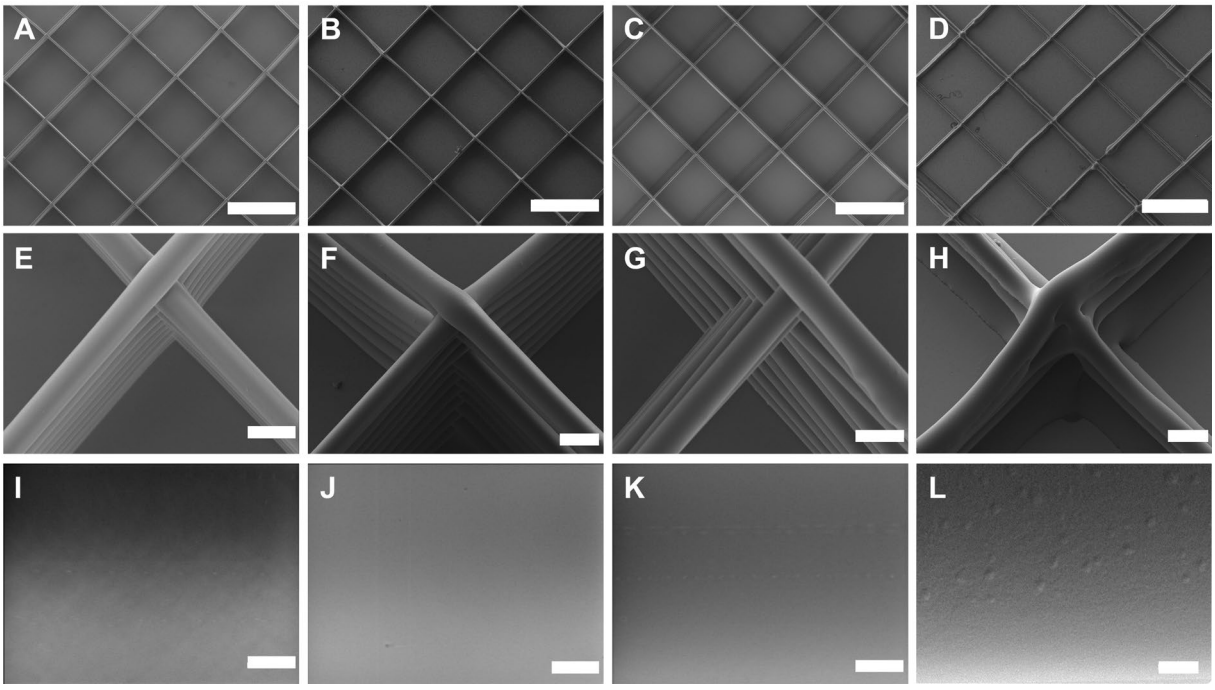

Figure 4. SEM images of copolymers 1 to 4. A–D) Square-shaped MEW scaffolds with 500 µm inter-fiber distance presenting the accurate and precise MEW fibers on top of each other for copolymer 1, 2, 3, 4 respectively (scale bar: 500 µm). E–H) Well-stacked fibers on top of

each other for copolymer 1, 2, 3, 4 respectively (scale bar: 20 µm), and I–L) showing the smooth surface of the fibers for copolymer 1, 2, 3, 4 respectively (scale bar: 2 µm).

2.3. Topographical Analysis of Fiber Surfaces

The influence of different segment ratios of the $(AB)_n$ and $(ABAC)_n$ segmented copolymers on fiber topography was investigated using single layer MEW fibers with 20 µm diameter for each copolymer. The fibers were printed between 800 and 2000 mm min^{-1} with 3.0 kV, 1.0 bar, and 2.2 mm collector distance. The single layer, straight and continuous copolymer fibers with a uniform diameter were used in the study. The MEW fibers were extremely homogenous and exhibited a smooth fiber surface for all the copolymers as seen by scanning electron microscopy (SEM) (Figure 4I–L). Compared to other polymers investigated for MEW,[10, 39] the smoothness and roughness of the fiber surface are notable difference. Often, morphological features such as spherulites[12] or striations[34] indicating flow-induced crystallization or microphase separation have been observed on the surface of MEW fibers, when semi-crystalline polymers were processed.

It is well-known that the chemical structure, average molecular weight, polarity, and volume fraction of the different segments strongly influence the morphology of a copolymer.[40, 41] Therefore, atomic force microscopy (AFM) was used to investigate surface properties for the four different copolymers. AFM analysis suggests that the ratio between the different copolymer components influences the topography of the fiber surface (Figure 5). In particular, copolymer 4 fibers showed a rougher surface topography compared to the other copolymers, with a root mean square deviation of 1.11±0.37 nm. In comparison, surface roughness of copolymers 1, 2, and 3 were 0.81±0.09, 0.44±0.04, and 0.42±0.04 nm, respectively. All surfaces have significantly different roughness values compared to each other, except for the comparably smooth surfaces of copolymers 2 and 3 ($p < 0.005$). Those roughness values are smaller than MEW PCL.[39]

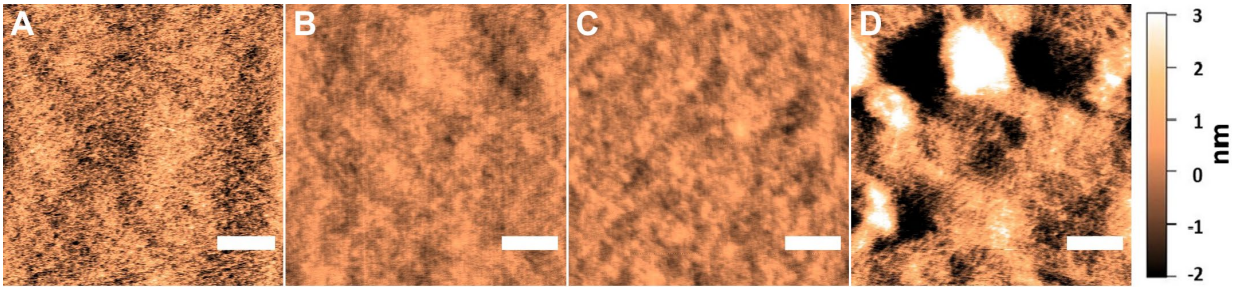

Figure 5. AFM height images of the copolymers. Copolymer A) 1, B) 2, C) 3, and D) 4 (scale bar: 200 nm). Height bar for all images shown on the right.

2.3. Inter-Layer Bonding Test

Bisurea segmented copolymers are also known for excellent bonding between single layers, meaning that physical crosslinks re-assemble after breaking.[17, 41] At the MEW processing temperature, the bisurea segments disaggregate and reform during fiber formation upon cooling, acting as physical crosslinks throughout the polymer network. It is therefore expected that layers will strongly bond together at intersection points. The inter-layer bonding of 20 µm MEW fibers from copolymers 1 to 3 are tested with Y-shaped constructs (Figure 6A). The design of Y-shaped constructs is a fiber wall divided into two different walls to measure the strength of the bonds between the layers. The constructs are bent backward by 180° and peeled under uniaxial tensile loading condition shown in Figure 6B and C. Y-shaped constructs of copolymer 1 are shown in Figure 6D before the test and of copolymer 3 after testing in Figure 6E. It is ensured that the bonded portion of the Y-shaped constructs remains perpendicular to the applied force. Maximal force is calculated using force–displacement curve (Figure 6F, G). During printing, collector speeds are adjusted to achieve the same fiber diameters for all copolymers. However, such different collector speeds will affect the jet cooling rate and therefore inter-layer bonding. The collector speeds for Y-shaped construct are 800, 2000, and 2000 mm min^{-1} for copolymer 1, 2, and 3, respectively. All three copolymers have significantly different maximum forces (Figure 6G), while copolymer 3 has the strongest inter-layer bonding with 21±1 mN. The results show that the inter-layer bonding was improved with the consisting of bisurea and PPO-PEG-PPO segments and the increasing printing speed.[42] The copolymer 4 could not be performed for this test because this copolymer shows an adhesive behavior on the printed surface and could not be removed without damage.

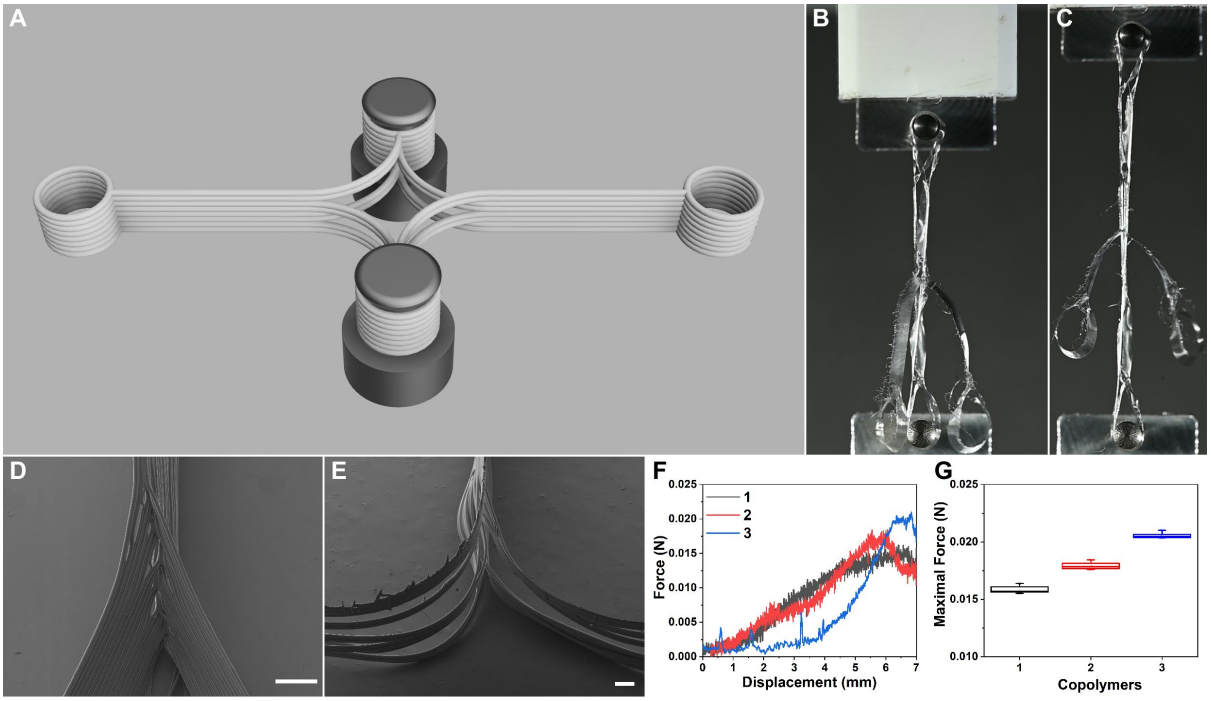

Figure 6. The inter-layer bonding behavior of the copolymers at crossover junctions. A) Rendered schematic of the test setup with two samples on metal pins. Inter-layer bonding testing setup B) before starting the test and C) during the test for copolymer 3. D) SEM pictures at crossover junction of copolymer 1 before the test and E) copolymer 3 after the test (scale bar: 200 µm). F) Force displacement and G) the average maximal force plot of the copolymers 1, 2, and 3.

2.4. Contact Angle Measurement and Swelling Test

The surface hydrophilicity of the copolymers is examined on square-shaped MEW 10-layer scaffolds with 200 µm inter-fiber distance. The scaffolds have 109 ± 20°, 107±13°, and 98±5° contact angles for copolymer 1, 2, and 3 respectively. Copolymer 4 immediately dissolved, when the water droplet is placed upon it.

The swelling behavior of the MEW scaffolds is examined by measuring the difference of the fiber width of 1-layer scaffolds and the area of 10-layer scaffolds, both with 500 µm inter-fiber distance, between in dry state and after the exposure to water for 3 h. The fibers show a rapid swelling due to their small diameters. The maximum swelling is reached immediately after the scaffolds were exposed to water (Figure S3, Supporting Information). As expected, the degree of swelling increases with the hydrophilicity of the copolymer from 1 to 4. Due to its hydrophobicity, copolymer 1 shows no swelling behavior. Swelling is investigated for copolymer 2 with 39% while

copolymer 3 shows a swelling of 42% on fiber diameter; 3% and 22% swelling is observed on 10-layer scaffold areas for copolymer 2 and 3, respectively.

2.5. *In Vitro* Cytocompatibility

Cytotoxicity of copolymers 1, 2, 3, and 4 is verified by elute test with L929 mouse murine fibroblast cells, as shown in Figure 7. Tissue culture polystyrene (PS) is used as a negative control and normalization for cellular activity, while poly(vinyl chloride) (PVC) is the positive control. The results of dsDNA amounts (Figure 7A), metabolic activity (Figure 7B), and metabolic activity per cells (Figure 7C) were normalized to negative control. Copolymers 1, 2, and 3 are non-cytotoxic. However, the cytotoxicity of copolymer 4 is depending on the concentration, thus, the copolymer displayed cytotoxicity in the range of 50–100%. The cytotoxicity of copolymer 4 is attributed to the PPO-PEG-PPO segments, which behave as a surfactant to the cell membrane.[43]

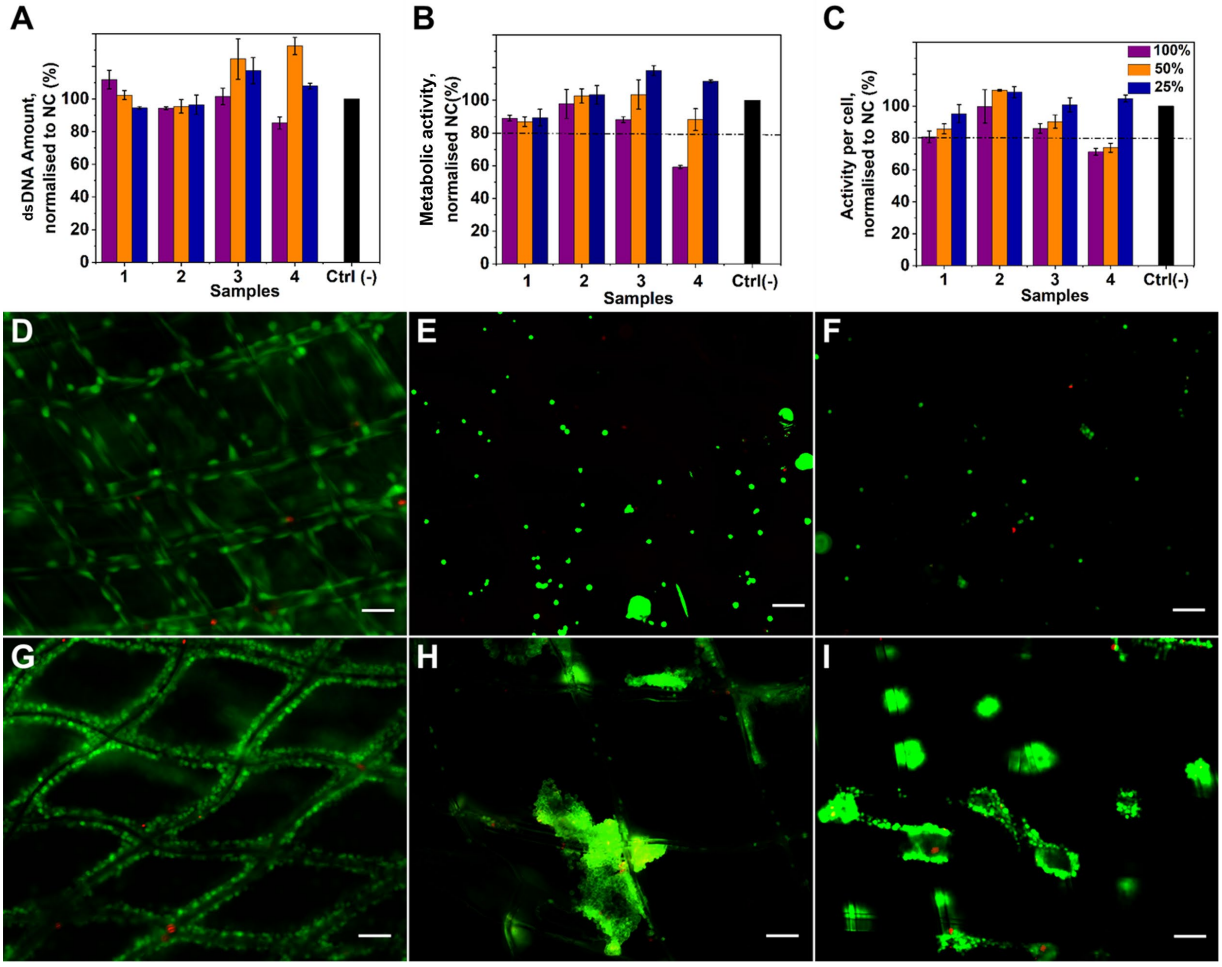

Figure 7. Cytotoxicity tests of copolymer films using L929 murine fibroblasts A–C) and viability of L929 murine fibroblast cells on MEW copolymers D–I). A) dsDNA amounts, B) metabolic activity, and C) metabolic activity per cell determined via eluate testing using PS and PVC as controls. Live/Dead staining (alive cells: green; dead cells: red) of attached L929 cells to MEW copolymers D–F) copolymer 1, 2, and 3 at day 1, G–I) at day 4, respectively. The cell attachment is lower with the present of the PPO-PEG-PPO segments (scale bar: 100 µm at (E–I), 50 µm at (D)).

Live/Dead staining is performed with L929 cells on MEW scaffolds (Figure 7D–I), and cell viability is over 80% for copolymer 1, 2, and 3 at day 4. The attachment and proliferation, as well as metabolic activity of L929 cells on the MEW scaffolds, are determined via dsDNA content and metabolic cell activity at days 1 and 4 (Figure S4, Supporting Information). The results of PicoGreen assay indicate that dsDNA amounts are increased at day 4 compared to day 1 (Figure S4B, Supporting Information). However, the cell attachment is lower on copolymer 3 at day 1 compared to copolymer 1 and 2 due to the bioinert nature of PPO-PEG-PPO segments. Also, there is significantly less adhesion on the copolymer 3 scaffold

compared to copolymer 1 and 2 at day 4. The metabolic cell activity on MEW scaffolds is increased at day 4 except for copolymer 3 (Figure S4A, Supporting Information). Copolymer 4 is not investigated due to its immediate dissolution.

3. Conclusion

In conclusion, $(AB)_n$ and $(ABAC)_n$ segmented copolymers are well compatible with MEW at similar processing conditions. Smooth, well-formed fibers could be formed across different chemical compositions that ranged from hydrophobic through to hydrophilic. The fiber deposition can be well-controlled, enabling the fabrication of complex and layer-by-layer structures. When in contact with cells, the scaffolds either supported adhesion or dissolved without cytotoxic products at lower concentrations indicating that this class of copolymers has broad physical properties. There are several specialized areas such as capillary origami, microfluidic, flexible electronic device, soft network composites, sacrificial materials where these copolymers could have utility due to their unique surface properties, transparency, and adjustable hydrophilicity.

4. Experimental Section

Materials

The $(AB)_n$ and $(ABAC)_n$ segmented copolymers (Figure 1) were synthesized according to the previous work.[16,17,33] Copolymer 1 is a hydrophobic $(AB)_n$ segmented copolymer made of bisurea segments and PDMS segments. Copolymers 2 and 3 are amphiphilic $(ABAC)_n$ segmented copolymers consisting of bisurea segments, hydrophobic PDMS segments, and hydrophilic PPO-PEG-PPO segments. The ratios between bisurea, PDMS, and PPO-PEG-PPO segments are 13:80:7 wt.% for copolymer 2 and 15:53:32 wt.% for copolymer 3. Copolymer 4 is a hydrophilic $(AB)_n$ segmented copolymer and has bisurea segments and PPO-PEG-PPO segments.

Rheology

Oscillatory shear rheology experiments of the copolymers were conducted using a Kinexus lab+ rheometer (Malvern Panalytical) at a cooling rate of 2 K min^{-1} and a frequency of 1 Hz. Samples with a thickness around 1 mm were investigated in a 25 mm plate-plate geometry. First cooling cycle was recorded, whereas melting the sample in the rheometer was considered as first heating.

MEW Device and Printing Parameters

All experiments were performed with a custom-built MEW printer as previously described[17] and syringes pressurized with N_2 and regulated using a pressure gauge (FESTO, Berkheim, Germany). Inside the MEW head, a 26-gauge nozzle with the length of 5.4 or 7 mm (Unimed S.A., Lausanne, Switzerland) and a glass syringe (FORTUNA® Optima, 3 mL, Poulten & Graf GmbH, Wertheim, Germany) with the copolymer was heated by three ceramic electric heaters (Bach RS, Germany). The x-y movement of the collector was controlled by linear stages and operated by G-code. All MEW constructs were printed at an ambient temperature of 21.5±1.5 °C and relative humidity of 35±2%. Furthermore, all copolymers were processed at 100 °C and printability assessed using collector speeds ranging from 500 to 2800 mm min^{-1} for 0.5 to 1.0 bar. The scaffold printing ultimately was performed on between 800 and 2000 mm min^{-1} at 1.0 bar.

Imaging

The average fiber diameters were measured by using a tabletop SEM (TM3030, Hitachi High-Technologies Corporation, Mannheim, Germany) and a crossbeam 340 SEM equipped with GEMINI e-Beam column (Carl Zeiss Microscopy GmbH) with all samples imaged after platinum coating (Leica EM ACE600, Wetzlar, Germany). Video was recorded using a Nikon Z6 digital camera with Nikon ED 200 mm lens. Furthermore, the SEM FEI Quanta FEG 250 (Thermo Fisher Scientific) was used for imaging the surface of the constructs. The untreated constructs were placed in the sample chamber of the FEI Quanta FEG 250, and the measurements were

conducted in the low vacuum mode (water pressure of 40 Pa in the sample chamber).

Atomic Force Microscopy (AFM)

AFM imaging was performed in air on a Molecular Force Probe (MFP) 3D system (Asylum Research, Oxford Instruments). Samples were scanned at 2.5 μm s−1 in amplitude modulation mode using AC240 AFM probes with nominal resonance frequency of ≈70 kHz and spring constant of 2 N m−1. Images were recorded at a resolution of 1.95 nm pixel−1. Surface roughness values are given as averages from 8 to 14 different surface areas of 250 nm × 250 nm in at least two 1 μm × 1 μm images from independent fiber positions per sample and were measured as root mean square height variations using the MFP software (Asylum Research, Oxford Instruments).

Contact Angle Measurement and Swelling Tests

For the surface wettability test, MEW scaffolds with 10 layers with 200 μm inter-fiber distance were used. The measurement was performed with deionized water using a static contact angle measurement instrument (Contact Angle System OCA20).

For the swelling experiment, a 1-layer and a 10-layer MEW scaffold with 500 μm inter-fiber distance from every copolymer was exposed to deionized water at ambient conditions. The swelling was monitored and recorded by microscope (Nikon Dualphot 300). Pictures were taken for 3 h with a magnification at 10×. The fiber diameter and scaffold size change were determined by using ImageJ.

Inter-Layer Bonding Test

The Y-shaped constructs and mechanical setup allowed to test fiber bonding between layers shown in Figure 6A. Additional G-codes are provided in Supporting Information. The inter-layer bonding was measured with an ElectroForce 5500 test instrument (TA Instruments, USA) using a 250 g load cell, previously described.[44]

Eluate and Direct Cell Cytotoxicity Testing

Eluate tests were performed according to ISO 10 993-5 applying L929 (ATCC, Rockville, USA) cells. Copolymer films were incubated in cell culture media consisting of Dulbecco's modified Eagle's medium, GlutaMax, 1%, 1 M HEPES, 1% penicillin–streptomycin, and 10% FCS. Cytotoxic PVC platelets were used as a positive control. Elution medium without any incubated material served as a negative control while eluates prepared by material incubation for 48 h at 37 °C. Then, suspended sediments were centrifuged and the supernatant was referred to 100% eluate. Both 50% and 25% eluates were prepared by dilution with fresh cell culture medium. WST-1 and PicoGreen assays were performed to determine metabolic L929 cell activity and DNA amount, respectively after 2 days of incubation. All samples were tested at least in triplicates.

Cell adhesion experiments were performed with L929 cells, where a total of 500 000 cells were seeded on MEW 10-layer scaffolds with 500 or 250 µm inter-fiber distance. Live dead staining, PicoGreen, and WST-1 assays were performed on day 1 and 4 according to manufacturer's instruction.

Statistics

One-way analysis of variance was performed for statistical analysis. Statistical significance is defined as $p < 0.05$.

Acknowledgments

The technical assistance of Philipp Stahlhut and Judith Friedlein for SEM imaging, Dr. Carina Blum for proof reading, Dr. Andrei Hrynevich for G-code generation, Andreas Züge for video recording, and Ievgenii Liashenko for video editing is highly appreciated. The authors thank Dr. Reiner Giesa for the help with rheological measurements and discussion. The project was financed by the Deutsche Forschungsgemeinschaft (DFG, German Research Foundation)—Project number 326998133—TRR 225 (sub-project A04). The DFG State Major Instrumentation

Program (INST 105022/58-1 FUGG) funded the Zeiss Crossbeam CB 340 SEM used in this study.

Open access funding enabled and organized by Projekt DEAL.

Conflict of Interest

The authors declare no conflict of interest.

References

1. A. Georgopoulou, L. Egloff, B. Vanderborght, F. Clemens, Actuators 2021, 10, 102.
2. Z. Zhu, H. S. Park, M. C. Mcalpine, Sci. Adv. 2020, 6, eaba5575.
3. A. Youssef, S. J. Hollister, P. D. Dalton, Biofabrication 2017, 9, 012002.
4. D. W. Hutmacher, Biomaterials 2000, 21, 2529.
5. T. D. Ngo, A. Kashani, G. Imbalzano, K. T. Q. Nguyen, D. Hui, Composites, Part B 2018, 143, 172.
6. P. D. Dalton, Curr. Opin. Biomed. Eng. 2017, 2, 49.
7. T. M. Robinson, D. W. Hutmacher, P. D. Dalton, Adv. Funct. Mater. 2019, 29, 1904664.
8. G. Hochleitner, T. Jüngst, T. D. Brown, K. Hahn, C. Moseke, F. Jakob, P. D. Dalton, J. Groll, Biofabrication 2015, 7, 035002.
9. E. C. L. Bolle, D. Nicdao, P. D. Dalton, T. R. Dargaville, In Computer-Aided Tissue Engineering: Methods and Protocols, (Eds.: A. Rainer, L. Moroni), Springer, New York, 2021, pp. 111– 124.
10. J. C. Kade, P. D. Dalton, Adv. Healthcare Mater. 2021, 10, e2001232.
11. S. Florczak, T. Lorson, T. Zheng, M. Mrlik, D. W. Hutmacher, M. J. Higgins, R. Luxenhofer, P. D. Dalton, Polym. Int. 2019, 68, 735.
12. J. N. Haigh, T. R. Dargaville, P. D. Dalton, Mater. Sci. Eng., C 2017, 77, 883.
13. F. Chen, G. Hochleitner, T. Woodfield, J. Groll, P. D. Dalton, B. G. Amsden, Biomacromolecules 2016, 17, 208.
14. R. S. Diaz, J. - R. Park, L. L. Rodrigues, P. D. Dalton, E. M. De-Juan-Pardo, T. R. Dargaville, Adv. Mater Tech. 2021, 2100508.
15. D. Nahm, F. Weigl, N. Schaefer, A. Sancho, A. Frank, J. Groll, C. Villmann, H. -. W. Schmidt, P. D. Dalton, R. Luxenhofer, Mater. Horiz. 2020, 7, 928.
16. G. Hochleitner, E. Fürsattel, R. Giesa, J. Groll, H. -. W. Schmidt, P. D. Dalton, Macromol. Rapid Commun. 2018, 39, 1800055.
17. J. Mechau, A. Frank, E. Bakirci, S. Gumbel, T. Jungst, R. Giesa, J. Groll, P. D. Dalton, H. -. W. Schmidt, Macromol. Chem. Phys. 2021, 222, 2170001.
18. B. D. Ratner, S. J. Bryant, Annu. Rev. Biomed. Eng. 2004, 6, 41.
19. A. S. Hoffman, Adv. Drug Delivery Rev. 2002, 54, 3.
20. W. Hu, S. Lu, Z. Zhang, L. Zhu, Y. Wen, T. Zhang, Z. Ji, Biomater. Sci. 2019, 7, 1323.
21. M. D. Swartzlander, C. A. Barnes, A. K. Blakney, J. L. Kaar, T. R. Kyriakides, S. J. Bryant, Biomaterials 2015, 41, 26.

22. J. S. Miller, K. R. Stevens, M. T. Yang, B. M. Baker, D.-H. T. Nguyen, D. M. Cohen, E. Toro, A. A. Chen, P. A. Galie, X. Yu, R. Chaturvedi, S. N. Bhatia, C. S. Chen, Nat. Mater. 2012, 11, 768.
23. B. Grigoryan, S. J. Paulsen, D. C. Corbett, D. W. Sazer, C. L. Fortin, A. J. Zaita, P. T. Greenfield, N. J. Calafat, J. P. Gounley, A. H. Ta, F. Johansson, A. Randles, J. E. Rosenkrantz, J. D. Louis-Rosenberg, P. A. Galie, K. R. Stevens, J. S. Miller, Science 2019, 364, 458.
24. T. Lorson, S. Jaksch, M. M. Lübtow, T. Jüngst, J. Groll, T. Lühmann, R. Luxenhofer, Biomacromolecules 2017, 18, 2161.
25. D. Williams, In Tissue Engineering, Academic Press, Burlington, 2008, pp. 255– 278.
26. J. He, X. Zhao, J. Chang, D. Li, Small 2017, 13, 1702626.
27. M. Castilho, R. Levato, P. N. Bernal, M. De Ruijter, C. Y. Sheng, J. Van Duijn, S. Piluso, K. Ito, J. Malda, Biomacromolecules 2021, 22, 855.
28. G. M. Pawar, M. Koenigs, Z. Fahimi, M. Cox, I. K. Voets, H. M. Wyss, R. P. Sijbesma, Biomacromolecules 2012, 13, 3966.
29. Q. Chen, X. Mei, Z. Shen, D. Wu, Y. Zhao, L. Wang, X. Chen, G. He, Z. Yu, K. Fang, D. Sun, Opt. Lett. 2017, 42, 5106.
30. F. Kotz, P. Risch, K. Arnold, S. Sevim, J. Puigmartí-Luis, A. Quick, M. Thiel, A. Hrynevich, P. D. Dalton, D. Helmer, Nat. Commun. 2019, 10, 1.
31. K. Koenig, K. Beukenberg, F. Langensiepen, G. Seide, Biomater. Res. 2019, 23, 1.
32. O. Bas, E. M. De-Juan-Pardo, C. Meinert, D. D'angella, J. G. Baldwin, L. J. Bray, R. M. Wellard, S. Kollmannsberger, E. Rank, C. Werner, T. J. Klein, I. Catelas, D. W. Hutmacher, Biofabrication 2017, 9, 025014.
33. E. M. Fürsattel, Extrusion-Based Melt Processing of $(AB)_n$ Segmented Poly(urea-siloxane)s and their Modification towards Amphiphilic Hydrogels, University of Bayreuth, Bayreuth, Germany 2021.
34. G. Hochleitner, A. Youssef, A. Hrynevich, J. N. Haigh, T. Jungst, J. Groll, P. D. Dalton, BioNanomaterials 2016, 17, 159.
35. A. Hrynevich, I. Liashenko, P. D. Dalton, Adv. Mater. Technol. 2020, 5, 2000772.
36. J. Kim, E. Bakirci, K. L. O'neill, A. Hrynevich, P. D. Dalton, Macromol. Mater. Eng. 2021, 306, 2000685.
37. A. Hrynevich, B. Ş. Elçi, J. N. Haigh, R. Mcmaster, A. Youssef, C. Blum, T. Blunk, G. Hochleitner, J. Groll, P. D. Dalton, Small 2018, 14, e1800232.
38. M. A. Skylar-Scott, J. Mueller, C. W. Visser, J. A. Lewis, Nature 2019, 575, 330.
39. C. Blum, J. Weichhold, G. Hochleitner, V. Stepanenko, F. Würthner, J. Groll, T. Jungst, 3D Print. Addit. Manuf. 2021.

40. S. Sami, E. Yildirim, M. Yurtsever, E. Yurtsever, E. Yilgor, I. Yilgor, G. L. Wilkes, Polymer 2014, 55, 4563.
41. N. Candau, G. Stoclet, J. -. F. Tahon, A. Demongeot, E. Yilgor, I. Yilgor, Y. Z. Menceloglu, O. Oguz, Polymer 2021, 223, 123708.
42. E. Bakirci, N. Schaefer, O. Dahri, A. Hrynevich, P. Strissel, R. Strick, P. D. Dalton, C. Villmann, Adv. Biosyst. 2020, 4, 2000077.
43. L. Castan, C. José Da Silva, E. Ferreira Molina, R. Alves Dos Santos, J. Biomed. Mater. Res., Part B 2018, 106, 742.
44. I. Liashenko, A. Hrynevich, P. D. Dalton, Adv. Mater. 2020, 32, 2001874.

3.2. Summary of manuscript II

This work fabricated a 3D printed radial device that systematically determines the matrices promoting cell growth and migration. The study is the first time that MEW has been used to fabricate 3D *in vitro* tools rather than fabricate scaffolds. The radial device has eight chambers, and four different Matrigel concentrations are distributed into chambers U87 glioblastoma cells are seeded into the cell depot. The cell growth and migration were screened throughout all chambers for eight days. U87 cell growth and migration were promoted by 6 and 8 mg mL^{-1} Matrigel concentrations. Also, the effect of design and process parameters on the printing accuracy of radial devices was systematically investigated.

3.2.1. Manuscript II

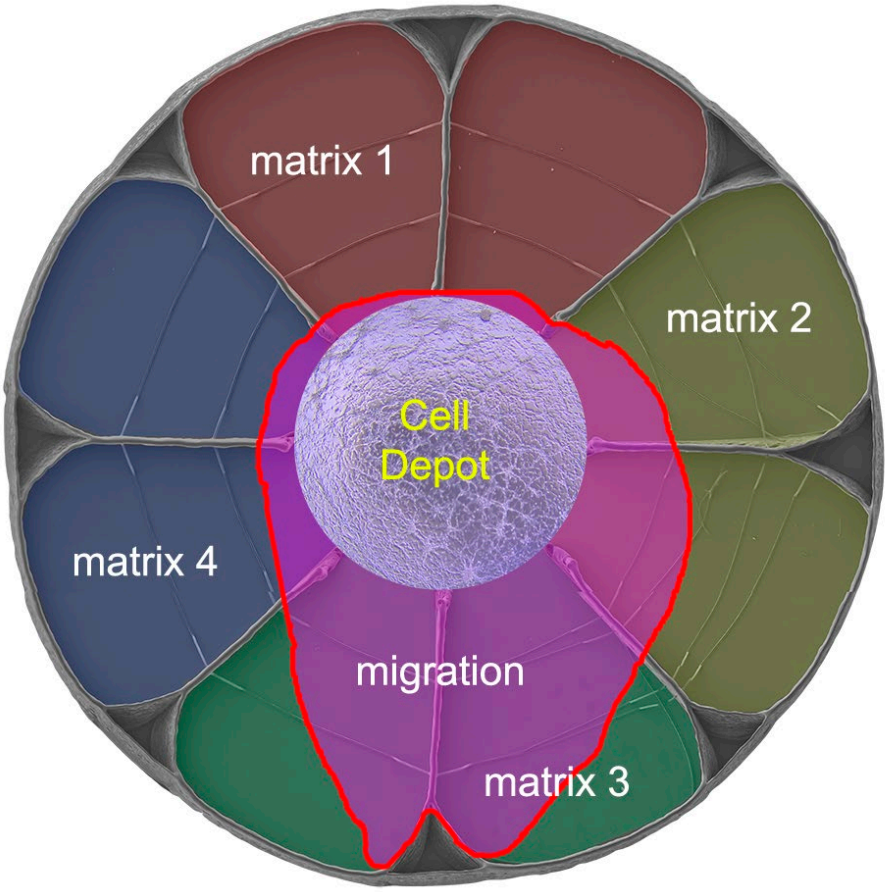

Melt Electrowritten In Vitro Radial Device to Study Cell Growth and Migration

First published: 02 September 2020 at Wiley Advanced Biosystems

https://doi.org/10.1002/adbi.202000077

Melt Electrowritten In Vitro Radial Device to Study Cell Growth and Migration

Ezgi Bakirci, Natascha Schaefer, Ouafa Dahri, Andrei Hrynevich, Pamela Strissel, Reiner Strick, Paul D. Dalton, Carmen Villmann,

E. Bakirci, O. Dahri, A. Hrynevich, Prof. P. D. Dalton
Department of Functional Materials in Medicine and Dentistry and Bavarian Polymer Institute
University Hospital of Würzburg
Pleicherwall 2, 97070, Würzburg, Germany
E-mail: paul.dalton@fmz.uni-wuerzburg.de

Prof. C. Villmann, Dr. N. Schaefer
Department of Clinical Neurobiology
University Hospital of Würzburg
Versbacherstr. 5, 97078 Würzburg, Germany

Prof R. Strick, Dr. P. Strissel
Department of Gynecology and Obstetrics, Laboratory for Molecular Medicine,
University Hospital Erlangen, Friedrich-Alexander University Erlangen-Nürnberg,
University Str. 21-23, 91054 Erlangen, Germany

** both authors contributed equally to this work*

Keywords: 3D cell culture, electrohydrodynamic, biofabrication, melt electrospinning writing

Abstracts

The development of in vitro assays for 3D microenvironments is essential for understanding cell migration processes. A 3D-printed in vitro competitive radial device is developed to identify preferred Matrigel concentration for glioblastoma migration. Melt electrowriting (MEW) is used to fabricate the structural device with defined and intricate radial structures that are filled with Matrigel. Controlling the printing path is necessary to account for the distance lag in the molten jet, the applied electric field, and the continuous direct-writing nature of MEW. Circular printing below a diameter threshold results in substantial inward tilting of the MEW fiber wall. An eight-chamber radial device with a diameter of 9.4 mm is printed. Four different concentrations of Matrigel are dispensed into the radial chambers. Glioblastoma cells are seeded into the center and grow into all chambers within 8 days. The cell spreading area demonstrates that 6 and 8 mg mL^{-1} of Matrigel are preferred over 2 and 4 mg mL^{-1}. Furthermore, topographical cues via the MEW fiber wall are observed to promote migration even further away from the cell seeding depot. Previous studies implement MEW to fabricate cell invasive scaffolds, whereas here it is applied to 3D-print in vitro tools to study cell migration.

1. Introduction

Tissue regeneration, inflammation, and cancer progression are being considered as the frontline in several tumor and tissue engineering paradigms, and cell migration is an essential part of these scenarios.[1] Migration is influenced by chemotactic, topographical, and mechanotransductive cues from the extracellular matrix.[2] Moreover, cell migration in the context of cancer metastasis is a complex and important factor for understanding tumor progression.[3]

The most aggressive form of a primary brain tumor is glioblastoma multiforme (GBM) which are highly invasive heterogenous tumors with a very low survival rate.[4] Surgical resection and chemo- or radiotherapy is commonly used for patient treatment, however, tumor recurrence is very frequent. Importantly, GBM cells invade and migrate along white matter tracts and brain blood vessels which promote tumor dissemination.[5] Hence, it is critical to understand the basic process of tumor migration and progression in order to develop new therapeutic drugs and treatment regimens.

While therapeutic approaches that minimize GBM migration are logical, another approach focuses on guiding these cells away from the tumor into biomaterial reservoirs with the goal to reduce tumor size.[6] This diversional approach is based on the placement of a tube filled with a matrix and oriented substrate that provides topographical guidance cues at the tumor site. This results in the attraction and guidance of migration of GBM cells into the tube, effectively reducing overall tumor size. Therefore, in line with this study and the fact that GBM cells have an affinity for white brain matter and blood vessels, it is important to develop new 3D in vitro cell culture models to determine the optimal matrix composition that drives GBM migration.

Novel research methods and tools provide an opportunity to study cell migration during cancer metastasis[7] where loss of cell adhesion from the primary tumor along with increased cell motility and invasion occurs. There is evidence from 3D microfluidic devices and microchips that matrix stiffness influences the migratory and invasive capabilities of tumor cells through the structure characteristics.[8]

There have been significant advances to understand the process of cell migration using in vitro models, which are cost-effective and easier to use compared to in vivo studies. With existing in vitro assays, cell migration conditions are well-defined, with many based on the traditional 2D cell culture methods.[9] While simple to use, they are challenged to recapitulate the 3D in vivo microenvironment.

Many assays have been developed to provide additional information, such as the response of cells to biochemical, adhesive, topographical,[10], and mechanical[11] cues. The scratch assay, used widely for migration analysis, consists of analyzing the movement of a monolayer of cells after a pipet tip is dragged along the surfaces.[12] Although this method is simple to use, scratch assays are not always comparable to the physiological conditions. In contrast, 3D migration environments would provide a better realization and analysis of cell migration by incorporating chemotactic stimuli or topographical cues.[13] The benefits of developing a competitive in vitro migration assay are to test a spectrum of different microenvironments at the same time.

Recent progress in additive manufacturing (AM) provides new fabrication opportunities for in vitro migration models in terms of reproducibility, precision, minimal volume of materials, well characterized microenvironment, and quantifiable gradient generation.[14] AM technologies such as fused deposition modeling, stereolithography, and melt electrowriting (MEW) facilitate faster prototyping, short times for manufacturing, and lower manufacturing cost.[15] MEW is an AM technology that uses sub-micron to micron scale diameter fibers as a building block while controlling their orientation,[16] generating structures with precise placement of fibers and high surface to volume ratio.[17] Depending on the laydown pattern and inter-fiber spacing, MEW scaffolds with different porosities and pore designs can be fabricated.[18] The fabrication of MEW structures with an increased build height might be applicable for in vitro systems. The current maximum thickness of fabricated MEW scaffolds is 7 mm.[19]

For MEW, a molten polymer is delivered to a nozzle and stretched into low-micron diameter fibers by applying an electrical field. The fiber size depends on several parameters such as nozzle diameter, pressure, and collector distance, which is the distance between the nozzle and the collector.[16] The collector speed can

affect the lag in the electrified molten jet and is therefore an important variable to control the accuracy of MEW fiber placement. The threshold collector speed that incorporates these parameters was named critical translational speed (CTS).[20] The vast majority of MEW scaffolds have been fabricated above the CTS mostly as straight fibers and box-like structures, as it is difficult to predict where the fiber will land when the collector is changing directions. Herein, we systematically investigated the influence of collector speed and number of layers on the accuracy of circular-shaped constructs to extend the design perspective for MEW. The goal of this investigation was to create a MEW in vitro competitive 3D radial device toward the rapid screening of different hydrogels and/or hydrogel concentrations/stiffness to test cell migration of the human glioblastoma cell line U87. This 3D radial device could also be adapted with different hydrogels and other cell types for future testing.

2. Results and Discussion

The structural frame of the competitive 3D in vitro radial culture device was made using MEW of poly(ε-caprolactone) (PCL). The small dimensions that we aimed to use were not currently possible with conventional extrusion-based technologies, or stereolithography, which have lower resolutions than MEW. However, since most MEW research is based on linear fiber deposition, fiber placement in this study is affected by continual changes in the direct-writing direction. Due to the need to control the molten jet lag, fiber placement under these circumstances was especially exacerbated by fiber pulsing phenomenon (Figure 1A). Therefore, very stable printing parameters (Table S1, Supporting Information) were necessary to achieve MEW fiber placement accuracy. The MEW printing conditions used here resulted in a fiber diameter of 17.55±0.87 μm and the collector speed used was 1.4xCTS to print the structural frame of the competitive 3D in vitro radial culture device.

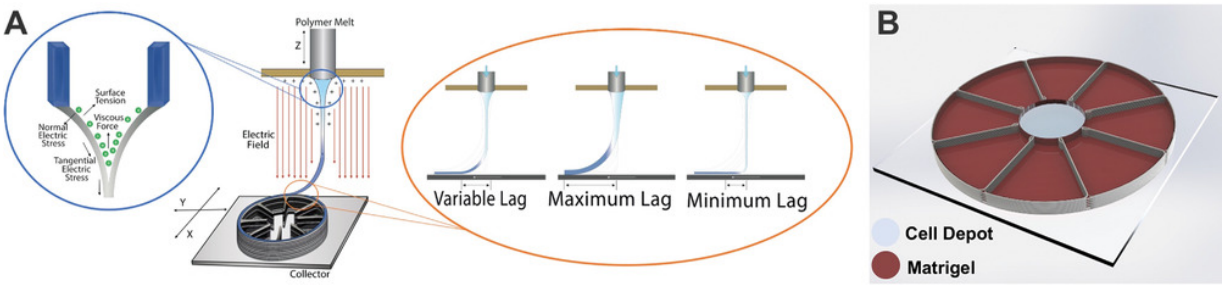

Figure 1. Overview of the competitive in vitro radial culture device. A) Schematic of the MEW jet with the blue circle demonstrates a Taylor cone of the molten polymer and the implications of fiber pulsing on jet lag (adapted under the term of Creative Commons 3.0 License.[20] Copyright 2016, The Authors, published by De Gruyter and adapted under the term of Creative Commons 3.0 License.[21] Copyright 2018, The Authors, published by IntechOpen.). B) Overview of the radial device design with the cell depot in the center (light blue) surrounded by eight chambers used for matrix testing. In the present study, different concentrations of Matrigel (red) were used.

Glass slides were coated with star-shaped NCO-poly(ethylene oxide-*stat*-propylene oxide) (sP(EO-*stat*-PO)) except for a 3 mm circle at the center of the device. This coating ensured the adhesion of the fibers during consequent washing and handling. Each radial device was composed of a central cell depot (which was devoid of the hydrophilic sP(EO-stat-PO) coating) and radially expanding matrix chambers (Figure 1).

One general limitation of MEW addressed in the current design was that fiber direct-writing is a continuous process and starting/stopping of the jet mid-print was not practically implementable. A continuous path (Figure 1A) was developed so that each printed layer had a similar height to the next. Several different design reiterations using a continuous printing path (Figure S1, Supporting Information) were investigated. The placement of cells in the central depot sealed the containers and allowed different matrices to be dispensed and form a hydrogel within each chamber of radial culture device (Figure 1B).

A 3D structure is produced by stacking the printed single fiber in a layer-by-layer approach. Since the collector speed is 1.4xCTS, the electrified molten jet lands on the collector behind the nozzle position. The designed radial culture devices contain multiple direction changes, so it is critical to compensate the jet lag to attain final reproducible structures. Therefore, we investigated the influence of collector

speed and the number of printed layers (i.e., wall height) on accuracy, precision, and dimensional consistency of the radial migration device. The determination of the dimensional differences in printing path, actual fiber placement, and the build height was therefore required.

The printing accuracy (D_{ACC}) indicates how the actual maximal circular diameter (D_A) approximates the printing path of the nozzle, or the designed diameter (D_D). To determine the printing accuracy, a series of circular structures with a diameter size from 2 to 16 mm was printed and assessed at different speeds (Figure 2). There was a clear improvement in the printing accuracy with larger circular paths (Figure S2A,B, Supporting Information) as well as with reduced collector speed close to the CTS (Figure S2C, Supporting Information). The accuracy of a 20 layer circular structure at 1xCTS, 2xCTS, and 3xCTS with the groups from 2 to 12 mm exhibited significantly different D_{ACC} values for each speed (Figure 2B). The accuracy of the circles was inversely proportional to the collector speed due to the growing lag between the nozzle and the jet contact point. In contrast, circles with a 16 mm diameter did not show any significant difference at these different speeds ($p_{1xCTS-2xCTS}$ =0.967, $p_{3xCTS-1xCTS}$ =0.069, $p_{3xCTS-2xCTS}$ = 0.127). D_{ACC} values for 16 mm were 94.6±2%, 94±1%, and 93.1±1% at 1xCTS, 2xCTS, and 3xCTS, respectively.

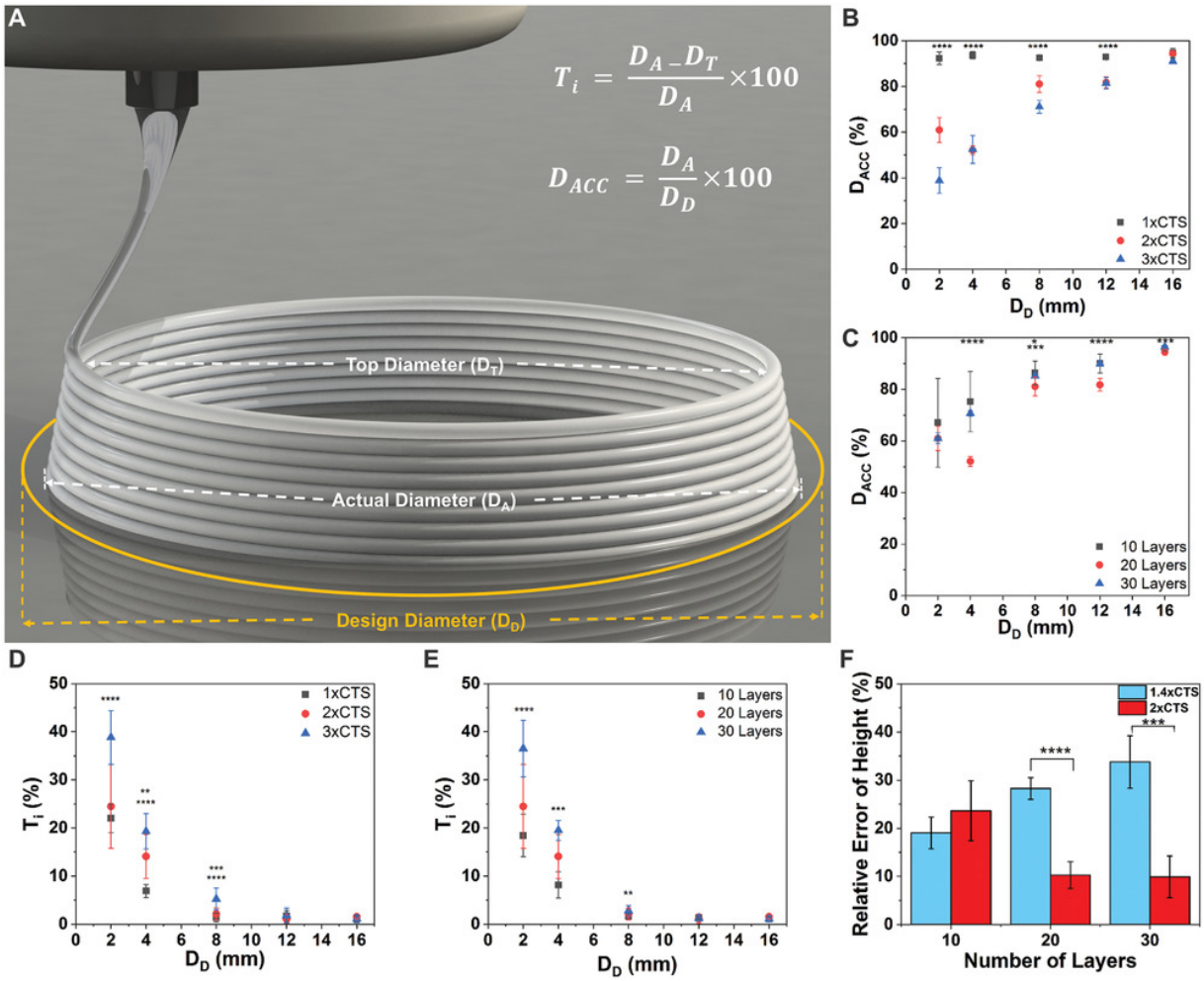

Figure 2. Effect of collector speed and construct height on geometrical accuracy. A) Schematic of MEW circular structure. B) Diameter accuracy of the circle size 2 to 16 mm at different collector speeds for 20 layers ($p_{1xCTS-2xCTS}$, $p_{1xCTS-3xCTS}$, $p_{2xCTS-3xCTS}$<0.0001 for 2 mm; $p_{1xCTS-2xCTS}$, $p_{1xCTS-3xCTS}$<0.0001, $p_{2xCTS-3xCTS}$=0.960 for 4 mm; $p_{1xCTS-2xCTS}$, $p_{1xCTS-3xCTS}$, $p_{2xCTS-3xCTS}$<0.0001 for 8 mm; $p_{1xCTS-2xCTS}$, $p_{1xCTS-3xCTS}$<0.0001, $p_{2xCTS-3xCTS}$ = 0.915 for 12 mm; $p_{1xCTS-2xCTS}$=0.967, $p_{1xCTS-3xCTS}$=0.069, $p_{2xCTS-3xCTS}$=0.127 for 16 mm). C) Different number of layers for 2xCTS ($p_{10L-20L}$=0.696, $p_{10L-30L}$=0.261, $p_{20L-30L}$=0.933 for 2 mm; $p_{10L-20L}$, $p_{20L-30L}$<0.0001, $p_{10L-30L}$=0.142 for 4 mm; $p_{10L-20L}$=0.021, $p_{10L-30L}$=0.283, $p_{20L-30L}$<0.001 for 8 mm; $p_{10L-20L}$, $p_{20L-30L}$<0.0001, $p_{10L-30L}$=0.157 for 12 mm; $p_{10L-20L}$<0.01, $p_{10L-30L}$=0.287, $p_{20L-30L}$<0.001 for 16 mm). D) The inward tilting index (T_i) at different collector speeds at 20 layers ($p_{1xCTS-2xCTS}$=0.177, $p_{1xCTS-3xCTS}$, $p_{2xCTS-3xCTS}$<0.0001 for 2 mm; $p_{1xCTS-2xCTS}$, $p_{1xCTS-3xCTS}$<0.0001, $p_{2xCTS-3xCTS}$=0.001 for 4 mm; $p_{1xCTS-2xCTS}$=0.101, $p_{1xCTS-3xCTS}$<0.0001, $p_{2xCTS-3xCTS}$<0.001 for 8 mm; $p_{1xCTS-2xCTS}$=0.445, $p_{1xCTS-3xCTS}$=0.962, $p_{2xCTS-3xCTS}$=0.306 for 12 mm; and $p_{1xCTS-2xCTS}$=0.230, $p_{1xCTS-3xCTS}$=0.991, $p_{2xCTS-3xCTS}$=0.283 for 16 mm). E) T_i of circle size from 2 to 16 mm on different diameter layers at 2xCTS ($p_{10L-20L}$=0.078, $p_{10L-30L}$, $p_{20L-30L}$<0.0001 for 2 mm; $p_{10L-20L}$, $p_{20L-30L}$<0.001, $p_{10L-30L}$<0.0001 for 4 mm; $p_{10L-20L}$=0.130, $p_{10L-30L}$<0.01, $p_{20L-30L}$=0.221 for 8 mm; $p_{10L-20L}$=0.434, $p_{10L-30L}$=0.625, $p_{20L-30L}$=0.493 for 12 mm; and $p_{10L-20L}$=0.089, $p_{10L-30L}$=0.953, $p_{20L-30L}$ =0.158 for 16 mm). F) Relative error of height of 10 mm circle diameter at 1.4xCTS and

2xCTS (p_{10L}=0.0727; p_{20L}<0.0001; p_{30L}<0.001). All the experiments have been performed with three independent samples (n = 3) (*p<0.05, **p<0.01, ***p<0.001, and ****p<0.0001).

The effect of increasing the number of layers on the D_{ACC} at 2xCTS was also investigated for 10, 20, and 30 layers (Figure 2C). The 2 mm diameter of circular structures exhibited no significant difference on the D_{ACC} with increased layers. The accuracy, however, of 4, 8, 12, and 16 mm diameter circles was significantly different at 20 layers compared to 10 and 30 layers (Figure 2C). Interestingly, the small diameter circles were cone-shaped, especially at higher collector speeds (Figure 2A). At collector speeds above the CTS, the inward tilting of the fiber wall was previously observed for sinusoidal MEW structures.[22] However, the previous study did not investigate the effect of the printing speed and the number of layers on inward tilting of walls. Such inward tilting of the wall into a cone shape can be measured by comparing the diameter of the first printed layer to the diameter of the top printed layer. The variability of different diameters was calculated using the following formula (1) in order to compare the inward tilting of the circular structures.

$$T\text{i}=\frac{\mathrm{DA}-\mathrm{DT}}{\mathrm{DA}}\times 100 \quad (1)$$

where T_i is the inward tilting index, D_A is the bottom, and D_T is the top layer diameter. Figure 2D shows the influence of the collector speed on T_i for different circle diameters using 20 layers printed at 1xCTS, 2xCTS, and 3xCTS, where T_i decreased with increasing circle diameter. T_i values were 22±2%, 6.9±1%, 1.4±0.9%, 1.6±1%, and 1.07±0.7% at 1xCTS for 2, 4, 8, 12, and 16 mm circles. No significant differences were observed between Ti values at 1xCTS, 2xCTS, and 3xCTS of circles with a diameter of 12 and 16 mm. Next, the consequences of decreased and increased layers of the circular structures and the printing speed on dimensional accuracy were evaluated (Figure 2E). T_i values revealed no significant differences between 10, 20, and 30 layers for 12 and 16 mm diameter circles.

The height of a MEW construct is expected to correspond to the number of layers multiplied by the fiber diameter. However, we found that fiber layers fuse differently depending on the collector speed. Concomitantly, the jet lag increased and affected jet cooling. As a consequence, fiber layer fusion led to decreased construct

height compared to the expected height. The relative error of the expected height versus the actual height for 10 mm diameter circular structures at 2xCTS and 1.4xCTS for 10, 20, and 30 layers is presented in Figure 2F. An increase in the number of fiber layers resulted in a larger difference between the expected and actual heights at least for a collector speed of 1.4xCTS. For the ten-layer group, the relative error of height of circular structures at 2xCTS is similar to 1.4xCTS. However, the relative error of the circles for 20 and 30 layers at 2xCTS is significantly lower than 1.4xCTS. The relative error of 10 mm scaffolds at 2xCTS is 10.2±2% and 9.9±4% for 20 and 30 layers, respectively. Since the collector distance does not change during printing, it is possible that with increased build height melting of the upper layers might occur due to increased proximity to the MEW head. Recently, Wunner *et al.* elaborated that the distance between the top layer and printing head can be kept constant by adjusting the *z*-axis while increasing the voltage[19] to produce superior layering. Adopting such parameters to our approach might preserve the electrostatic force, improve fiber stacking, and prevent excessive fusion between layers.

For the cell assay, three different groups (10 layers, 20 layers, 30 layers) of migration devices were characterized and compared (Figure 3). Representative scanning electron microscope (SEM) images of the three different scaffolds with their turning points created by the MEW jet for different layers are shown in Figure 3A–I. Based on the printing outcome and in line with the goal to minimize the size of the migration device, the final cell culture system had a diameter of 9.4±0.1 mm, a wall height of 30 layers (around 350 µm), and a wall thickness of 17±1 µm. Additionally, the internal reference rings were introduced every ten layers at a spacing of 2 mm apart to provide a visual guide and prevent the dispensed cells from being drawn into the chambers due to surface tension (Figure 4A and Figure S2D, Supporting Information).

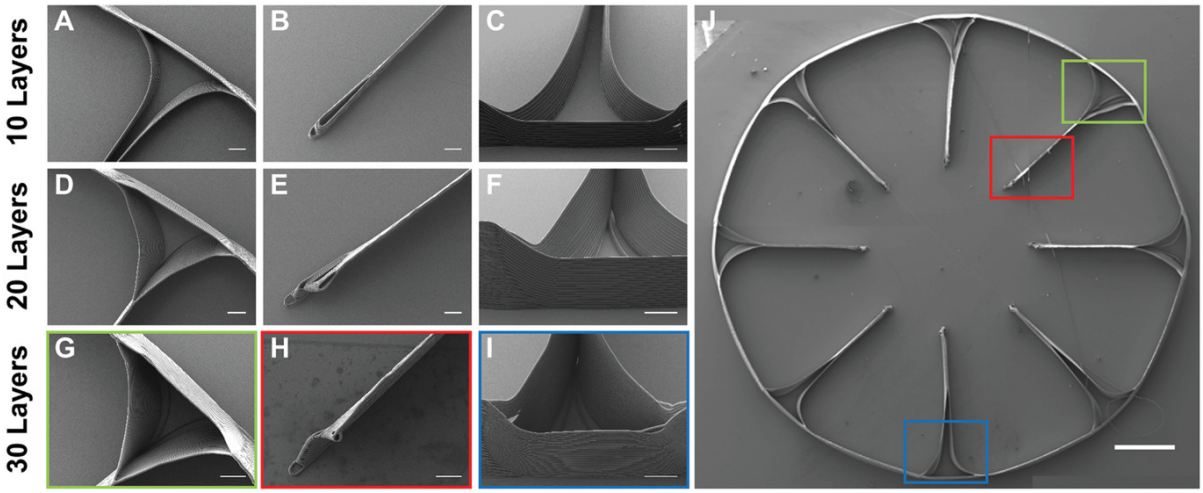

Figure 3. SEM images of different parts within the competitive 3D in vitro radial culture device. A,D,G) show 10, 20, and 30 layers (green box) and its effect on B,E,H) the point of the wall where fibers double back upon themselves (red box) and C,F,I) integrated corners (blue box). Scale bar in A–I is 200 µm. J) is a composite SEM image of a 30 layers radial culture device. Scale bar represents 2 mm.

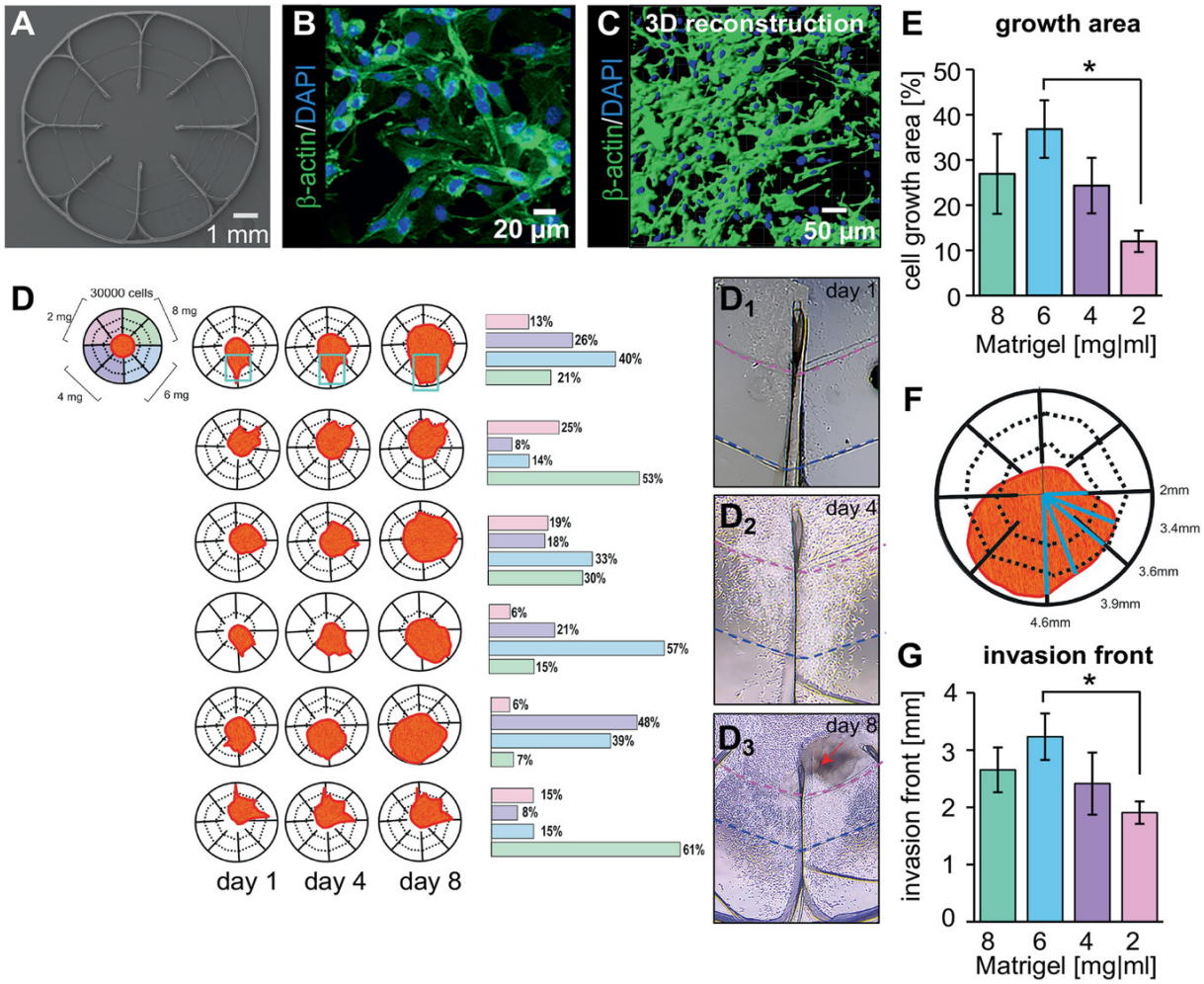

Figure 4. Glioblastoma cells prefer Matrigel concentrations of 6–8 mg mL^{-1}. A) SEM image of a radial device. B) Fluorescent staining of U87 cells for β-actin (green) and nuclear DNA (4′,6-diamidino-2-phenylindole, blue) at day 8 after seeding. C) 3D reconstruction. D) Schematic overview of a radial device showing the calculated cell growth areas in Matrigel at various concentrations (2 mg mL^{-1}, pink; 4 mg mL^{-1}, violet; 6 mg mL^{-1}, light blue; 8 mg mL^{-1}, light green) at indicated time points (days 1, 4, and 8). Values were obtained from six independent experiments (n=6). The bar diagrams (right) show the relative cell growth in different Matrigel concentrations at day 8. D_1, D_2, and D_3 demonstrate the representative images of U87 cell growth at days 1, 4, and 8. The pink and blue dotted lines show the printed rings after 10 and 20 layers which help for orientation of cell growth. The red arrow points to densely packed tumor cells growing from the bottom to the top of the Matrigel. E) Mean area of cell growth from all experiments. Note, cells prefer stiffer matrices of 6 and 8 mg mL^{-1} of Matrigel. Values of significance *p=0.044 for 6 mg mL^{-1} compared to 2 mg mL^{-1}. F, G) Calculation of the cell invasion front at day 8 (schematic view in (F)). G) Mean distances to the invasion front at day 8 in different Matrigel concentrations (five data points obtained for each concentration of Matrigel; six independent experiments were

analyzed, *n*=6). The distance to the invasion front is significantly enhanced at 6 mg mL^{-1} compared to 2 mg mL^{-1} (*p =0.037).

A human glioblastoma cell line, U87, was used to assess the competitive 3D in vitro radial culture device with respect to cell growth and migration. Different Matrigel concentrations within separate chambers facilitated U87 cells to determine a preferred matrix for migration and growth. A total of 30 000 cells in 4 mg mL^{-1} of Matrigel were seeded as a droplet into the center of the pre-warmed MEW device (Figure 4A) to seal off the chambers. Four increasing concentrations (2, 4, 6, and 8 mg mL^{-1}) of cell-free Matrigel were added into the eight surrounding chambers of the radial devices (Figure 4D), and U87 cells were cultured for 8 days. At day 8, the cytoskeletal protein β-actin and the nuclei of the U87 cells were stained and then reconstructed into 3D images (Figure 4B and Video 1, Supporting Information). U87 cells formed a dense cellular network as shown in an example from a chamber containing 6 mg mL^{-1} Matrigel (Figure 4C). Each matrix has a neighboring chamber with an identical matrix concentration, where the MEW fiber wall could be assessed for topographical migration. The areas of cell distribution were monitored at days 1, 4, and 8 (Figure 4D–D3,E). The lowest percentage of cells was present in 2 mg mL^{-1} of Matrigel (14±2.8%, Figure 4E). The calculated areas of U87 cells at different days after seeding from six independent experiments (n = 6) showed a strong preference toward 6 and 8 mg mL^{-1} of Matrigel (33±6.3% for 6 mg mL^{-1}, 31.2±8.4% for 8 mg mL^{-1}, Figure 4E). The mean values demonstrate a significant increase of tumor cell growth in 6 mg mL^{-1} compared to lower Matrigel concentrations of 2 mg mL^{-1} (p < 0.05; Figure 4E). It is notable that there is also some topographical guidance of the cells due to the MEW fiber walls, Figure 4D1–D3).

The importance of matrix stiffness for brain tumor growth has been shown in various reports.[23] For glioblastoma, it has been demonstrated that matrix stiffness influences morphology, proliferation, and migration.[24] Similar effects on morphology and proliferation have also been described for primary cells of the brain, e.g., microglia and astrocytes.[25] The matrix used in the present study, up to 8 mg mL^{-1} of Matrigel, is very soft as determined previously[26] (66±4.4 Pa for 8 mg mL^{-1} and 31±5.6 Pa for 4.5 mg mL^{-1}). The elastic modulus of 6 mg mL^{-1} Matrigel was assigned with 48±9.2 Pa; *n*=3) and is similar to values reported for the normal brain, whereas tumors have been found to prefer material with a stiffness above

100 Pa.[27] Enhanced growth and migration of the glioblastoma cell line U87 noted at higher Matrigel concentrations (6 and 8 mg mL^{-1}) is reflected in our radial culture device, although biochemical signals also play a role. The calculation of the invasion front at different Matrigel concentrations reflects the data from cell growth. The furthest distance (in mm) where cells have migrated/proliferated from the center in 8 days was observed at 6 mg mL^{-1} Matrigel (3.2±0.4 mm compared to 1.9±0.2 mm with 2 mg mL^{-1}, $*p<0.05$; 2.4±0.5 mm for 4 mg mL^{-1}, and 2.6±0.4 mm for 8 mg mL^{-1}, both did not reach significance compared to 2 mg mL^{-1}). The use of our radial device together with differential extracellular matrix densities and compositions in future experiments—especially defined matrices with immobilized cues[28, 29]—will allow the identification of formulations which either further increase or decrease the tumor migration behavior. The encouragement of GBM cells to migrate was part of certain biomaterial-based paradigms to reduce brain tumor volume in vivo.[6] To enhance spatio-temporal resolution of the cellular processes, a combined approach using automation of the matrix dispensation in the radial device together with real-time measurements to study the migratory capability of the cells[30] and a quantitative approach to investigate changes in gene expression profiles are needed to better understand tumor cell dynamics. Besides dissecting cell–matrix interaction, the radial device is further suitable to investigate the migratory behavior of cells upon co-culturing with other cell types present in the in vivo situation.[28, 31]

MEW remains a young AM technology, that is currently focusing on the fabrication of scaffolds or matrix-reinforcing structures for tissue engineering[32] or biofabrication.[33] However, MEW could also be used for the fabrication of precise and advanced in vitro systems. The limits of MEW resolution in this context reported here give insight where this AM technology can potentially contribute to establishing improved 3D in vitro assays, including radial migration. With further automation and experiment digitization, this newly developed MEW 3D in vitro radial cell culture device may be suitable to investigate cellular migration and could facilitate rapid screening and reiteration of different hydrogels in a competitive manner. The presented methodology has applicability to other cell types to study individual cell migration parameters such as cell trajectories, accumulated distance, and speed.

Initially, our in vitro model provides a tool for analyses of glioblastoma migration in 3D environments composed of different hydrogels, encouraging future

studies with co-cultures or other applications such as drug screening. Due to the ability of soluble cues to migrate between chambers, however, future designs would include matrices (or fibers) with tethered bioactive molecules,[34] so that clear distinctions between chambers are easier to elucidate.

3. Conclusion

In this study, MEW was used to fabricate a 3D radial migration device in order to establish a competitive assay for glioblastoma cell migration. Fabricating such a radial migration device using MEW, however, required a constant change in the printing path for MEW, while maintaining a continuous fiber during the printing process. With the current design of the radial device, we determined the printing effects on the radius of the final dimensions. Moreover, we showed the influence of the collector speed and wall height to the fabrication accuracy. The radial device was successfully established and functionally tested using a glioblastoma cell line implementing different matrix concentrations. Such a competitive migration device is applicable for other cell types and we predict that, when further automated, it could represent a useful tool to screen a spectrum of different matrices.

Experimental Section

Materials

Pellets of medical-grade PCL (Corbion Inc., Netherlands, PURASORB PC 12, Lot#1712002224 05/2018) were used after appropriate storage.[35] The chemically reactive macromer, six-armed star-shaped NCO-terminated sP(EO-*stat*-PO) was provided by DWI Leibnitz Institute for Interactive Materials (Aachen, Germany) with a molecular weight of 12 000 g mol^{-1}.

NCO (sP(EO-stat-PO))-Coated Glass Slides

MEW constructs for the radial device were printed onto a glass slide coated with a chemically reactive surface based on sP(EO-*stat*-PO) as previously described,[36] except for the center (3 mm in diameter) of the radial device. Briefly, glass slides were cleaned by acetone, distilled water, and isopropanol for 5 min followed by air drying. Then, the slide was activated with oxygen plasma treatment in the plasma generator (Pico low pressure plasma system; Diener electronic,

Ebhausen, Germany) in a vacuum of 0.3 mbar for 20 min. Afterward, slides were placed in a desiccator with 3-aminopropyl-trimethoxysilane for surface activation. Slides were then removed and 10 mg mL^{-1} sP(EO-*stat*-PO) in 10% tetrahydrofuran solution in MilliQ water was loaded onto the glass slides and distributed with rotational spin coating homogenously at 2500 rpm for 40 s.

Design Optimization and Printing of the MEW Radial Device

The structural frame of the radial migration device was printed using an in-house built MEW machine [37] which was based on a *x-y* slide system and controlled via a G-code (A3200 Motion, version 4.09.000.0126, Aerotech Inc., Pittsburgh, USA). An electrical heater was utilized that contained a 22-gauge nozzle with Luer Lock (Carl Roth, Germany) and a syringe filled with PCL. The final parameters were a melt-temperature of 90 °C, an applied voltage of 5.5 kV, a pressure of 0.4 bar, and a collector distance of 3 mm. A pressure control valve (SMC, Germany) was operated with air for delivering the molten polymer to the nozzle. The structural MEW-frames were printed onto sP(EO-stat-PO)-coated glass slides except for the center of the cell depots using parameters previously described for circular constructs, combined with a collector speed of 1.4xCTS. Internal reference rings were introduced into the G-code at a spacing of 2 mm apart smaller circles every ten layers. The CTS was determined at 90 °C for a single-layer circular pattern. Circles were MEW between 1xCTS and 3×CTS with 2, 4, 8, 10, 12, and 16 mm diameters at 10, 20, and 30 layers to determine the printing accuracy. The actual diameters and heights were exhibited using the stereomicroscope software (Zen 2.3, Discovery V20, Carl Zeiss Microscopy GmbH, Göttingen, Germany). For each circle, five lines were drawn through the center. The average determined from five lines was used as the actual diameter of the circle. The effect of layer number on the height of the printed structures was investigated. Images of the different structures harboring different numbers of layers (10, 20, 30 layers) were taken by using stereomicroscope. The height of the printed structures was determined using the stereomicroscope software (Zen 2.3). For every circle, perpendicular lines were drawn of which the average was used as the mean height of the structures.

Imaging of Radial Cell Culture Devices

A stereomicroscope (Discovery V20, Carl Zeiss Microscopy GmbH, Göttingen, Germany) and a Crossbeam 340 scattering electron microscope equipped with GEMINI e-Beam column (Carl Zeiss Microscopy, Göttingen, Germany) were used for imaging the printed samples. Prior to SEM, the samples were first sputter-coated with 4 nm platinum (Leica EM ACE600, Wetzlar, Germany).

Rheology

Viscoelastic measurements of Matrigel Lot #9021355 at a concentration of 6 mg mL^{-1} were performed with a Physica MCR 301 rheometer (Anton Paar, Graz, Austria). Using a 25 mm diameter parallel plate configuration with 0.5 mm gap size, 0.5 mL of pre-chilled Matrigel samples were dispensed onto a 4°C-cooled lower plate. After elevating the temperature to 37 °C for 45 min to crosslink the Matrigel, the linear viscoelastic (LVE) region was determined through an amplitude sweep from 0.01% to 100% strain at 1 Hz. The oscillatory frequency sweep was performed within this LVE (0.1% strain; 0.1–100 Hz) to observe the dynamic rheological behavior at 37 °C. All rheological experiments were performed in triplicates using a fresh sample each time. The gel region was monitored below 10 Hz ($G' > G''$) for all concentrations.

Migration Device Assembly and Cell Seeding

The U87 cell line was obtained from ATCC (HTB-14; ATCC – Global Biosource Center, Manassas, VA, USA). U87 cells were grown in Minimum Essential Media (MEM, Life Technologies, Darmstadt, Germany). The medium was supplemented with glutaMAX (200 × 10−3 M) and sodium pyruvate (100 × 10−3 M), penicillin (50 U mL^{-1})/streptomycin (50 µg mL^{-1}), and 10% fetal calf serum. Cells were grown in an incubator at 37 °C and 5% CO_2. Cells were split twice a week using trypsinization with accutase (A1110501, Thermo Fischer Scientific, Darmstadt, Germany).

Prior to seeding, radial devices were subjected to UV light for 20 min and washed once with 70% ethanol and afterward with dH2O. A total of 30 000 cells were mixed with Matrigel (Corning, NY, USA) (final concentration 4 mg mL^{-1}) and placed as a drop into the center of the radial device in a total volume of 6 µL. The cell-laden

droplet was allowed to polymerize for 2 min at 37 °C. Following polymerization of the cell-laden droplet in the center of the radial device, Matrigel (6 µL for each chamber) at four different concentrations (2, 4, 6, 8 mg mL^{-1}) was dispensed in eight different chambers surrounding the cell plaque and incubated at room temperature in the cell culture hood for 2 min to allow polymerization at 37 °C. Following polymerization, the device was filled with 7 mL of MEM medium. The growth of the cells was documented within each chamber at days 0, 1, 4, and 8 after seeding.

Immunocytochemical Staining

Cells were fixed using 2% paraformaldehyde for 20 min at 21°C. Following three washing steps with phosphate-buffered saline (PBS), cells were permeabilized by PBS, 5% bovine serum albumin (BSA), 0.1% Triton-X-100. Cells were incubated with ActinGreen 488 ReadyProbes reagent (1:50 in PBS, 5% BSA, R37110, Thermo Fischer Scientific, Darmstadt, Germany) for 2 h at 21 °C. Cells in the radial device were washed three times with PBS. Stained cells were mounted using ProLong Glass Antifade Mountant with NucBlue (Thermo Fischer Scientific, Darmstadt, Germany). Images were taken with an Olympus microscope (Fluoview ix1000, Olympus, Hamburg, Germany). Merged image stacks of 1 µm (62 total) were used to prepare a video of U87 cells in the 3D surrounding. Imaris 7.7.2 was used for 3D reconstruction (Oxford Instruments, Abingdon, UK).

Experimental Design and Statistical Analysis

MEW radial devices: D_{ACC} and T_i values of the circles were compared using the Tukey's multiple comparisons test (one-way analysis of variance (ANOVA)) (Origin Pro, 2018b, OriginLab Corporation, Northampton, MA, US). Unpaired *t*-test was performed to compare the relative error of the height between different speeds. The three different independent samples were printed and a total of 15 diameter measurements were performed for each speed. Statistical significance was determined using a one-way ANOVA test (*p*-values below 0.05 were considered significant).

Experiments including cells were performed in six independent biological replicates (unless otherwise stated). The number of experiments for analyses were presented in the legends to the appropriate figures.

Microscopy, image acquisition: Images from grown cells were taken using a Leica DM IL LED (Leica, Wetzlar, Germany) microscope together with a Samsung mobile device 16 Megapixel (CMOS), F1.9-Blend. For analyzing cell spreading, the radial device was divided into nine areas: the center and eight radial sections containing different concentrations of Matrigel. From each section, a picture was taken. The combined images gave rise to an entire radial device at the timepoints investigated (days 1, 4, and 8). The images were further developed and organized by Adobe Photoshop and Illustrator software (Adobe) or Corel Draw (Corel Draw X6). Image analysis for quantification: processing of images using ImageJ.[38]

For each quarter (two chambers contain the same Matrigel concentration) of one radial device, the total size was measured by framing the quarter manually with the *area selection tool*. The pixel number of one quarter was set to 100%. Within each quarter, the area containing cells were measured by framing (*area selection tool*). The corresponding number of pixels was taken to calculate the percentage compared to the total area (relative cell growth [%]).

The cell invasion front was determined by the distance from the center to the farthest point that cells were migrated/proliferated at day 8 after seeding. The *parallel dimension tool* (Corel Draw X6) was used to calculate the distance (in mm). For each quarter (with two chambers always containing the same Matrigel concentration) of one radial device, a total of five measurements were performed (see Figure **4F**). The mean value for the invasion front was further calculated using GraphPad Prism Software. Quantification of data obtained from cell distribution analysis and invasion front determination within the radial devices were compared using the unpaired two-tailed *t*-test (GraphPad Prism, GraphPad Software, San Diego, CA, USA) with a probability of error of $p < 0.05$ was considered significant.

Acknowledgments

This work was supported by the German Research Foundation (DFG) as part of the Collaborative Research Centre SFB TRR225 (B01) as well as the DFG State Major Instrumentation Programme for funding the Zeiss Crossbeam CB 340 SEM (INST 105022/58-1 FUGG). N.S. is supported by funds of the Bavarian State Ministry of Science and the Arts and the University of Würzburg to the Graduate School of Life Sciences (GSLS), University of Würzburg, Germany. The authors thank Dr.

Philip Stahlhut for technical assistance with SEM imaging while discussions with Dr. Ievgenii Liashenko are appreciated. The authors thank Dr. Biranche Tendon for proof reading of the manuscipt.

Open access funding enabled and organized by Projekt DEAL.

Conflict of Interest

The authors declare no conflict of interest.

References

1. W. P. Daley, K. M. Yamada, Curr. Opin. Genet. Dev. 2013, 23, 408.
2. K. M. Yamada, M. Sixt, Nat. Rev. Mol. Cell Biol. 2019, 20, 738.
3. A. C. Bellail, S. B. Hunter, D. J. Brat, C. Tan, E. G. Van Meir, Int. J. Biochem. Cell Biol. 2004, 36, 1046.
4. R. Chen, M. Smith-Cohn, A. L. Cohen, H. Colman, Neurotherapeutics 2017, 14, 284.
5. A. Farin, S. O. Suzuki, M. Weiker, J. E. Goldman, J. N. Bruce, P. Canoll, Glia 2006, 53, 799.
6. A. Jain, M. Betancur, G. D. Patel, C. M. Valmikinathan, V. J. Mukhatyar, A. Vakharia, S. B. Pai, B. Brahma, T. J. MacDonald, R. V. Bellamkonda, Nat. Mater. 2014, 13, 308.
7. K. M. Stroka, Z. Gu, S. X. Sun, K. Konstantopoulos, Curr. Opin. Cell Biol. 2014, 30, 41.
8. a) S. C. Wei, L. Fattet, J. H. Tsai, Y. Guo, V. H. Pai, H. E. Majeski, A. C. Chen, R. L. Sah, S. S. Taylor, A. J. Engler, J. Yang, Nat. Cell Biol. 2015, 17, 678; b) H. Xu, X. Liu, W. Le, TrAC,Trends Anal. Chem. 2018, 105, 1.
9. T. D. Pollard, G. G. Borisy, Cell 2003, 112, 453. B. Winkler, I. S. Aranson, F. Ziebert, Commun. Phys. 2019, 2, 82.
10. C. T. Mierke, Rep. Prog. Phys. 2019, 82, 064602.
11. C.-C. Liang, A. Y. Park, J.-L. Guan, Nat. Protoc. 2007, 2, 329.
12. M. Mak, C. A. Reinhart-King, D. Erickson, Lab Chip 2013, 13, 340.
13. L. H. Duong, P.-C. Chen, Biomicrofluidics 2019, 13, 024108.
14. T. M. Robinson, D. W. Hutmacher, P. D. Dalton, Adv. Funct. Mater. 2019, 29, 1904664.
15. A. Hrynevich, B. S. Elci, J. N. Haigh, R. McMaster, A. Youssef, C. Blum, T. Blunk, G. Hochleitner, J. Groll, P. D. Dalton, Small 2018, 14, 1800232.
16. F. Chen, G. Hochleitner, T. Woodfield, J. Groll, P. D. Dalton, B. G. Amsden, Biomacromolecules 2016, 17, 208.
17. A. Youssef, A. Hrynevich, L. Fladeland, A. Balles, J. Groll, P. D. Dalton, S. Zabler, Tissue Eng., Part C 2019, 25, 367.
18. F. M. Wunner, M. L. Wille, T. G. Noonan, O. Bas, P. D. Dalton, E. M. De-Juan-Pardo, D. W. Hutmacher, Adv. Mater. 2018, 30, 1706570.
19. G. Hochleitner, A. Youssef, A. Hrynevich, J. N. Haigh, T. Jungst, J. Groll, P. D. Dalton, BioNanomaterials 2016, 17, 159.
20. G. Zhang, L. Qian, J. Zhao, H. Zhou, H. Lan, 3D printing (Ed: D. Cvetković), IntechOpen, London 2018.

21. O. Bas, D. D'Angella, J. G. Baldwin, N. J. Castro, F. M. Wunner, N. T. Saidy, S. Kollmannsberger, A. Reali, E. Rank, E. M. De-Juan-Pardo, D. W. Hutmacher, ACS Appl. Mater. Interfaces 2017, 9, 29430.

22. a) H. Ma, H. Xu, J. Qin, Biomicrofluidics 2013, 7, 011501; b) C. Wang, X. Tong, F. Yang, Mol. Pharm. 2014, 11, 2115.

23. K. Pogoda, R. Bucki, F. J. Byfield, K. Cruz, T. Lee, C. Marcinkiewicz, P. A. Janmey, Biomacromolecules 2017, 18, 3040.

24. P. Moshayedi, G. Ng, J. C. Kwok, G. S. Yeo, C. E. Bryant, J. W. Fawcett, K. Franze, J. Guck, Biomaterials 2014, 35, 3919.

25. D. Janzen, E. Bakirci, A. Wieland, C. Martin, P. D. Dalton, C. Villmann, Adv. Healthcare Mater. 2020, 9, 1901630.

26. J. M. Barnes, L. Przybyla, V. M. Weaver, J. Cell Sci. 2017, 130, 71.

27. S. E. Reid, E. J. Kay, L. J. Neilson, A. T. Henze, J. Serneels, E. J. McGhee, S. Dhayade, C. Nixon, J. B. Mackey, A. Santi, K. Swaminathan, D. Athineos, V. Papalazarou, F. Patella, A. Roman-Fernandez, Y. ElMaghloob, J. R. Hernandez-Fernaud, R. H. Adams, S. Ismail, D. M. Bryant, M. Salmeron-Sanchez, L. M. Machesky, L. M. Carlin, K. Blyth, M. Mazzone, S. Zanivan, EMBO J. 2017, 36, 2373.

28. M. D. Wood, D. Hunter, S. E. Mackinnon, S. E. Sakiyama-Elbert, J. Biomater. Sci., Polym. Ed. 2010, 21, 771.

29. T. L. Liu, S. Upadhyayula, D. E. Milkie, V. Singh, K. Wang, I. A. Swinburne, K. R. Mosaliganti, Z. M. Collins, T. W. Hiscock, J. Shea, A. Q. Kohrman, T. N. Medwig, D. Dambournet, R. Forster, B. Cunniff, Y. Ruan, H. Yashiro, S. Scholpp, E. M. Meyerowitz, D. Hockemeyer, D. G. Drubin, B. L. Martin, D. Q. Matus, M. Koyama, S. G. Megason, T. Kirchhausen, E. Betzig, Science 2018, 360, eaaq1392.

30. D. D. Truong, A. Kratz, J. G. Park, E. S. Barrientos, H. Saini, T. Nguyen, B. Pockaj, G. Mouneimne, J. LaBaer, M. Nikkhah, Cancer Res. 2019, 79, 3139.

31. N. Abbasi, S. Ivanovski, K. Gulati, R. M. Love, S. Hamlet, Biomater. Res. 2020, 24, 2.

32. N. T. Saidy, F. Wolf, O. Bas, H. Keijdener, D. W. Hutmacher, P. Mela, E. M. De-Juan-Pardo, Small 2019, 15, 1900873.

33. a) D. Grafahrend, J. Lleixa Calvet, J. Salber, P. D. Dalton, M. Moeller, D. Klee, J. Mater. Sci.: Mater. Med. 2008, 19, 1479; b) S. E. Sakiyama, J. C. Schense, J. A. Hubbell, FASEB J. 1999, 13, 2214.

34. G. Hochleitner, T. Jungst, T. D. Brown, K. Hahn, C. Moseke, F. Jakob, P. D. Dalton, J. Groll, Biofabrication 2015, 7, 035002.

35. K. Klinkhammer, N. Seiler, D. Grafahrend, J. Gerardo-Nava, J. Mey, G. A. Brook, M. Moller, P. D. Dalton, D. Klee, Tissue Eng., Part C 2009, 15, 77.

36. M. de Ruijter, A. Hrynevich, J. N. Haigh, G. Hochleitner, M. Castilho, J. Groll, J. Malda, P. D. Dalton, Small 2018, 14, 1702773.
37. J. Schindelin, I. Arganda-Carreras, E. Frise, V. Kaynig, M. Longair, T. Pietzsch, S. Preibisch, C. Rueden, S. Saalfeld, B. Schmid, J. Y. Tinevez, D. J. White, V. Hartenstein, K. Eliceiri, P. Tomancak, A. Cardona, Nat. Methods 2012, 9, 676.

3.3. Summary of manuscript III

Many people worldwide suffer from neurological diseases. Changes in the brain microenvironment accompany neurological disease progression, and approaches that adequately reproduce these biochemical, biophysical, and cellular alterations are critical for evaluating repair outcomes or progressive degeneration. Biofabrication may be utilized to create *in vitro* models to understand better how the brain microenvironment influences disease progression of neurological diseases. In the present study, we established *in vitro* models to investigate the influence of 3D printed scaffolds design and preference of coated peptides on two different cell types, astrocytes, and glioblastoma U87 cells terms of theirs phenotypic changes. Box and triangle-shaped MEW scaffolds were coated with peptides such as RGD and IKVAV, peptide sequences of extracellular matrix proteins such as fibronectin or laminin, to simulate their complex microenvironment. The results showed that scaffolds design and biochemical cues affect the cellular shape.

3.3.1. Manuscript III

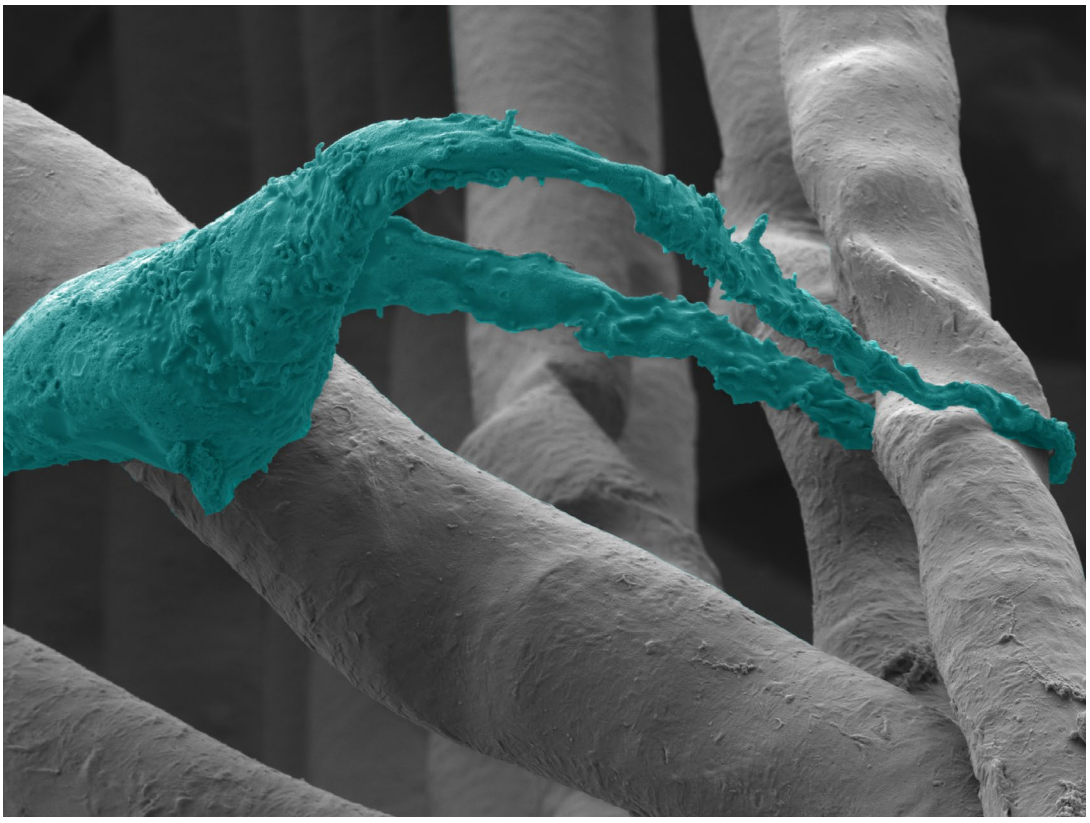

Altering the cell morphology on surface-functionalized melt electro-written scaffolds

The part manuscript III in this thesis is written as a research article and is planned to be published in the future.

Altering the cell morphology on surface-functionalized melt electro-written scaffolds

(to be submitted as a research paper)

Contributor	***Contributions***
Ezgi Bakirci	*Designed research; performed all experiments and analyzed data; prepared all the figures, wrote the manuscript*
Dieter Janzen	*Performed the astrocyte cell culture*
Carmen Villmann	*Performed the astrocyte cell culture and some confocal imaging, designed research; revised and provided feedback on the manuscript*
Paul D. Dalton	*Designed research; revised and provided feedback on the manuscript*

Abstract

Changes in the brain microenvironment accompany neurological disease progression, and techniques that effectively replicate these biochemical, biophysical, and cellular changes are important to assess repair outcomes or progressive degeneration. *In vitro* models that recapitulate the brain microenvironment is one such approach. This study uses a high-resolution three-dimensional (3D) printing technology to provide a structural and topographical framework or scaffold that can be peptide-modified to identify phenotypic alterations in astrocytes and glioblastoma cells. The 3D-printed scaffolds have a 0/90° and 0/45/90/135° laydown pattern that provides box- and triangle-shaped pore morphologies. Furthermore, these scaffolds are coated with RGD and/or IKVAV peptides to simulate sequences in fibronectin and laminin, respectively. Both the scaffold design and peptide sequence were found to affect the cellular area and eccentricity. Furthermore, scaffolds with a 200 μm interfiber spacing and peptide coating, especially RGD and IKVAV coated scaffolds, results in increased cell area than non-coated scaffolds. The results established some fundamental aspects that may be expanded upon to understand better the function of scaffold architecture and biochemical cues on cells that originate in the brain.

1. Introduction

Neurological disorders affect millions worldwide, including traumatic brain injury, stroke, primary and metastatic brain tumors, and neurodegenerative diseases [1]. In 2016, there were around 70 million cases of traumatic brain injury, 3,000 central nervous system cancers, and 8 million stroke cases in the world every year [1, 2]. These diseases are predicted to rise due to their prevalence among the elderly and increased population life expectancy. The severe and often terminal nature of these diseases underscores the urgent need to develop new experimental tools as disease models and therapeutic strategies to stop disease progression or predict improved regeneration outcomes. It is known that changes in the brain microenvironment accompany disease progression, although it is unclear how these biochemical, biophysical, and cellular aspects contribute to repair results or ongoing degeneration [3].

Biofabrication technologies have been utilized to create several *in vitro* models to understand better how the brain microenvironment contributes to processes associated with neurological diseases and constructions that promote healing and regeneration *in vivo* [4]. Melt electrowriting (MEW) is one fabrication technology used for *in vitro* models of non-neural tissue due to its accurate and precise characteristics, combined with a high porosity [5]. In addition, MEW is a fabrication technique that can be combined with other techniques, such as electrospinning and/or extrusion-based bioprinting, to control the microscale structures [6]. The modification of fibers with different biochemical cues further provides MEW scaffolds with properties well suited for 3D culture systems [7]. To increase the biomimetic properties, several strategies were used to modify MEW constructs with different biochemical cues using polydopamine, O_2 treatment, and sP(EO-stat-PO) [7-9].

To determine the feasibility of *in vitro* models, cellular phenotypes are a vital identifier as this is influenced by many intercellular mechanical processes, interactions with other cells, and the surrounding extracellular matrix. Therefore, cell morphology represents the integrative effect of many distinct processes and signaling pathways across different scales and is a valuable identifier for function, disfunction or migration, and cancer progression [10]. For instance, a recent study by Hu *et al*.

demonstrates that astrocytes exhibited different morphology when the culture was grown at different hydrogel stiffnesses [11]. Another recent study investigated cellular morphology as an indicator of cell genotypes and phenotypic responses [12]. Therefore, cellular phenotypes may contribute as an indicator and identifier for characterizing cell-material interactions. However, the quantification of cell-material interactions is challenging to interpret. Moreover, the complex biomaterial microenvironment can also contribute to the heterogeneous nature of cell shape responses. New analytical tools must be developed that consider both multi-parametric complexity and biological heterogeneity to identify and combine key cellular shape features correlated with biological outcomes [13].

In this study, we developed an *in vitro* model to study the effect of MEW scaffold design and biochemical cues on phenotypes changes of astrocytes as primary cells of the central nervous system and glioblastoma U87 as human tumor cells containing the disease state. Two different MEW laydown patterns were used for the scaffold design, which are 0/90° and 0/45/90/135°, and named box and triangle-shaped MEW scaffolds, respectively. The box and triangle MEW scaffolds were modified with biochemical cues, including RGD and IKVAV peptides, to mimic the complexity of their microenvironment. Here, we used a six-arm, star-shaped isocyanate-terminated poly(ethylene oxide-stat-propylene oxide) (NCO-sP(EO-stat-PO)) macromer to coat poly(ε-caprolactone) (PCL) MEW scaffolds. The MEW scaffold morphology was initially characterized by scanning electron microscopy (SEM) then the hydrophilicity and coating stability were investigated. Human glioblastoma U87 and primary murine astrocytes were then cultured on the scaffolds and monitored for phenotypical differences through cellular area and eccentricity.

2. Results and Discussion

2.1. Scaffold characterization

Box and triangle-shaped MEW scaffolds were produced from 3.7±0.4 μm diameter fibers, as shown in Figure 1. The box-shaped scaffold (Figure 1A) is a standard morphology that creates a cube-shaped void as the pore [14], while the triangle-shaped pore is a result of a 0/45/90/135° laydown pattern (Figure 1B, C). Such a

“triangle” lay-down pattern has been reported previously for MEW, and aligning the fibers; however, they intersect to form identical triangle pores is especially challenging [15, 16].

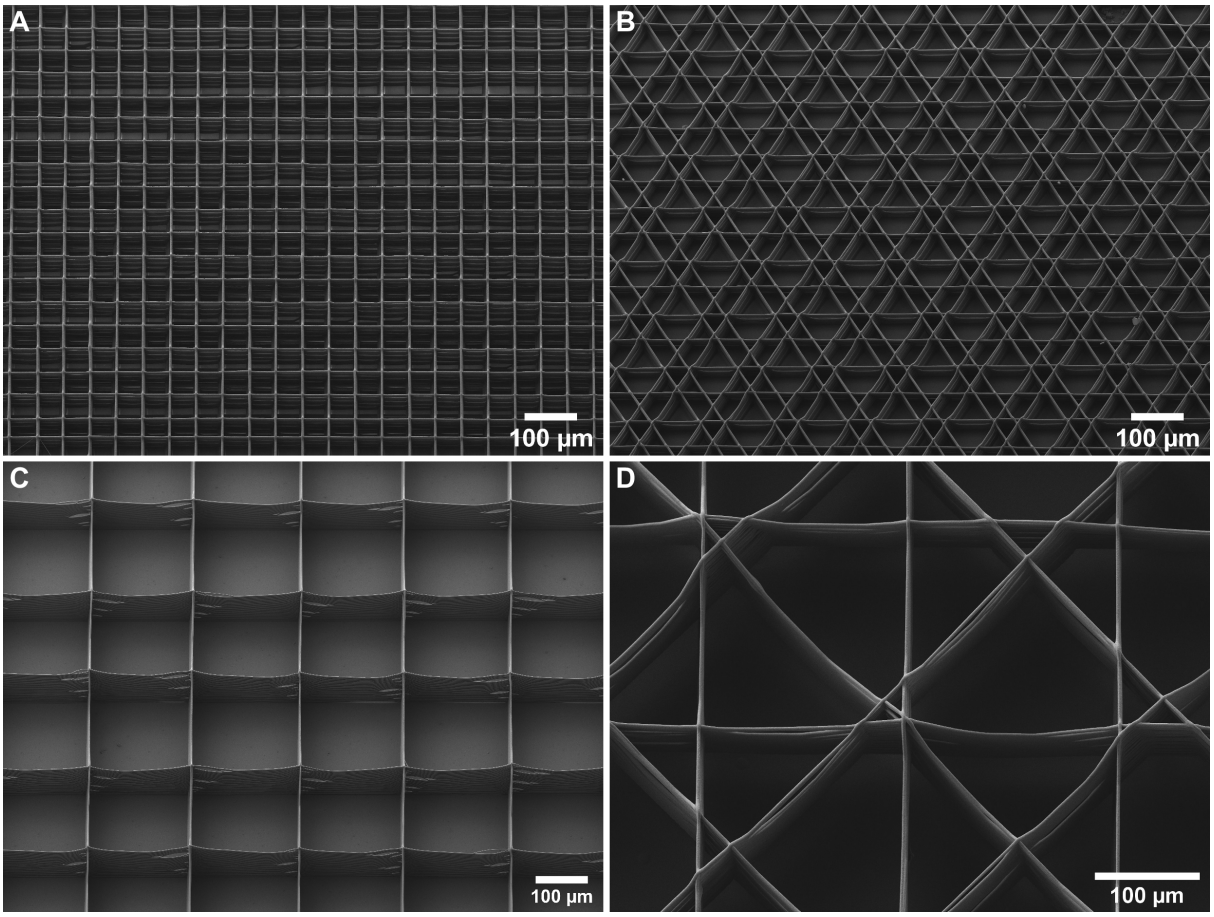

Figure 1. Different scaffolds design A) box-shaped scaffold B) triangle-shaped scaffold with 50 µm fiber spacing C) box-shaped scaffold D) triangle-shaped scaffold with 200 µm fiber spacing.

MEW normally allows for precisely controlled material design, and MEW scaffolds have been shown to facilitate cell adhesion, proliferation, and infiltration due to porous architecture and pore interconnectivity [13]. Most previous studies, however, use substantially larger fiber diameters that are produced here [17].

The fiber diameter used here is especially small for MEW and is accompanied by a fast jet speed, measured as 950 mm min^{-1}. Therefore, this high speed can provide challenges in accurately placing fibers for triangle pores made with a 0/45/90/135° laydown pattern (Figure 1B) due to jet lag at turns [5, 18]. The small fiber diameter is also utilized for reaching 50 µm fiber spacing without any fiber

bridging [19, 20]. However, it is especially pertinent to use such small diameter fibers as they have been previously shown that they can affect the cell phenotype [21].

Contact angle measurements showed that scaffolds became more hydrophilic when they were coated with NCO-sP(EO-stat-PO). The contact angle was 111±5^{o} for PCL scaffolds, and 15±3^{o} for NCO-sP(EO-stat-PO) coated scaffolds. In previous studies, NCO-P(EO-stat-PO) was combined with biodegradable hydrophobic synthetic polymers to create bioactive scaffolds and address many aspects of tissue engineering, such as adjustable cell adhesion, neural cell guidance, basal membrane mimicking, and inflammatory modulation [22].

As previously described, the as-printed PCL scaffold was first treated with a NaOH solution (Figure 2A). The NaOH-treated scaffolds were incubated NCO-sP(EO-stat-PO) for 10 min were tested to the presence of peptides on scaffolds with a solution of a FITC dye, conjugated to a short cysteine-containing peptide sequence (Cys-Gly-Gly-Lys(FITC)) overnight. After extensive washing with water, confocal microscopy confirms the presence of the FITC dye on the scaffolds on incubated NCO-sP(EO-stat-PO). The fluorescent dye was used to demonstrate the reactivity of NCO-sP(EO-stat-PO) (Figure 2B, C).

The scaffolds were coated with RGD (PCL + RGD), IKVAV (PCL + IKVAV), and RGD and IKVAV (PCL + RGD + IKVAV) via NCO-s(PEO-stat-PO). SEM and FITC dye confirmed the presence of NCO-s(PEO-stat-PO) on PCL fibers. The amount of bound peptide on PCL scaffolds showed a higher concentration of adsorbed peptide compared to pure PCL after four days of incubation in PBS. The amount of peptides for the scaffolds were 179.12±27, 183±11, 209.19±24 μg for PCL + RGD, PCL + IKVAV, PCL + RGD + IKVAV scaffolds, respectively.

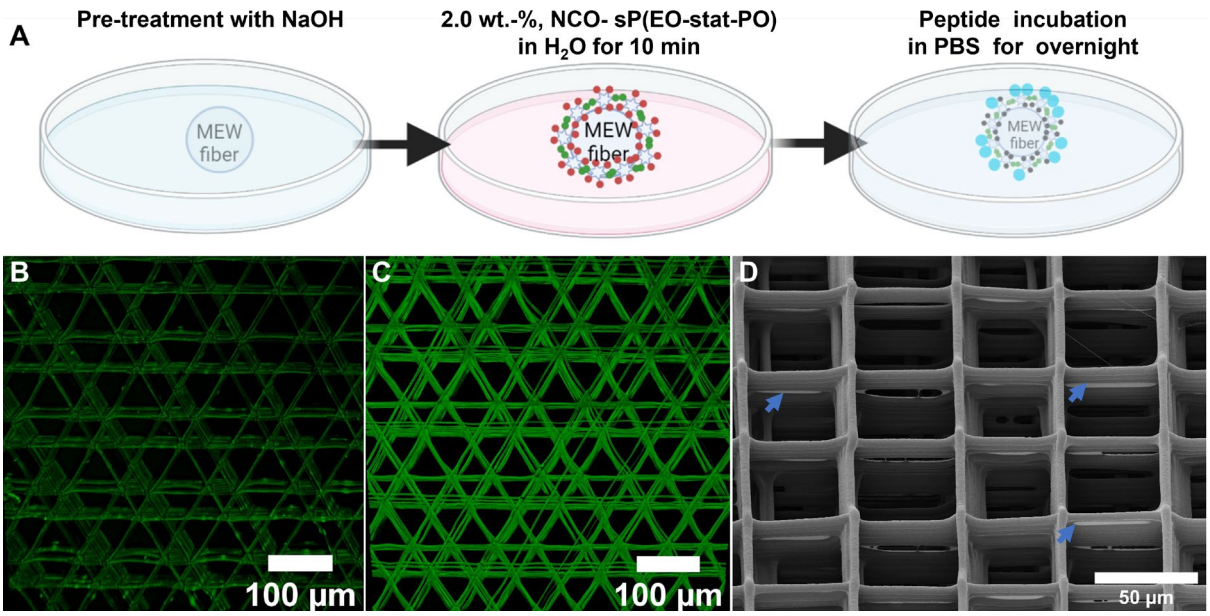

Figure 2. Peptide coating protocol and characterization of s(PEO-stat-PO) coating A) peptide-coating protocol B) confocal images of FITC-conjugated peptides on PCL fibers C) FITC conjugated peptide on NCO-s(PEO-stat-PO)-PCL fibers after overnight incubation and extensive washing with water D) SEM images of s(PEO-stat-PO) coated MEW scaffolds, indicating some pore-filling.

Similar to previous reports that used s(PEO-stat-PO)-coated MEW scaffolds [7], small bridging hydrogel coatings filled some of the pores between fibers. While this is slightly altering the morphology, it was considered minimal compared to the overall printed structure.

2.2. Cell morphology analysis

The major challenge in neural tissue engineering is identifying the *in vivo* microenvironment of the brain and the necessary components for achieving the repair or regeneration. Our approach has focused on carefully defined astrocytes and U87 glioblastoma cells population and their response to different control parameters inside the engineered microenvironment. For this purpose, U87 cells and primary murine astrocytes were seeded on the box, and triangle-shaped MEW scaffolds and peptide-coated scaffolds (Figure 3, 4). The triangle-shaped with 200 µm fiber spacing MEW scaffolds were coated with RGD, IKVAV, and a mixture of RGD and IKVAV peptides. After cell seeding, the cellular morphology was observed on day 2 and day 7 for U87 and primary astrocytes, respectively. The culture time was 2 days for U87

due to their high proliferation rate. Cellular area and eccentricity were defined by CellProfiler software. In addition, the results highlighted changes in cell shape among cell populations on different MEW scaffolds types.

The morphological difference of U87 cells on the box and triangle-shaped MEW scaffolds with 50 and 200 μm fiber spacing was observed. The scaffold designs and the size of fiber spacing significantly affect the cellular area (Figure 3). However, scaffold design and coating did not have any significant influence on the eccentricity of cells. The largest U87 cellular area was observed on triangle-shaped scaffolds with 200 μm fiber spacing (Figure 3I). In contrast, on the box-shaped MEW scaffolds with 200 μm fiber spacing, the cells mainly adhered to the fiber wall and formed clusters (Figure 3C). Triangle-shaped MEW scaffolds with 200 μm fiber spacing were coated with different peptides. It was clear that cellular areas on peptide-coated scaffolds were increased compared to non-coated triangle-shaped MEW scaffolds (Figure 3J). Thus, there were significant differences between non-coated and RGD coated scaffolds. The filopodia and lamellipodia protrusions from cells were also observed by SEM and confocal imaging to reveal their invasion through the MEW fibers (Figure 3A-H). The nucleus of the U87 cells was located at the rear of the cell, opposite the direction of movement or protrusion. This morphology was previously shown in our collaborative work about cell migration on MEW align fibers culture system.

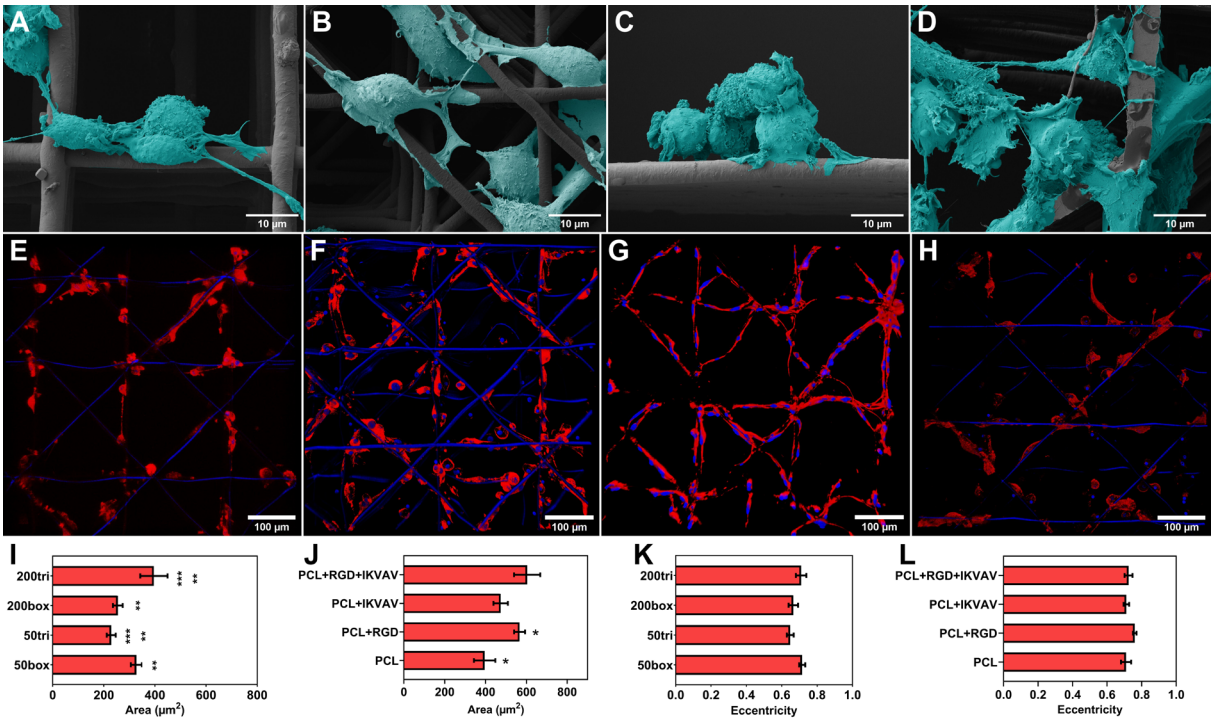

Figure 3. U87 glioblastoma cells exhibited different cellular morphology dependent upon MEW scaffolds. SEM images of A) box-shaped scaffold B) triangle-shaped scaffold with 50 µm fiber spacing C) box-shaped scaffold D) triangle-shaped scaffold with 200 µm fiber spacing. The confocal images of E) non-coated only PCL scaffold F) RGD (PCL+RGD) G) IKVAV (PCL+IKVAV) H) RGD+IKVAV (PCL+RGD+IKVAV) coated triangle-shaped MEW scaffold with 200 µm spacing. (Red: f-actin, blue: DAPI I- K) Size and shape-related metrics of the cells on different scaffold design (Label code: 50box: Box-shaped scaffold with 50 µm fiber spacing, 50tri: Triangle-shaped scaffolds with 50 µm fiber spacing, 200box: Box-shaped scaffolds with 200 µm fiber spacing, and 200tri: triangle-shaped scaffold with 200 fiber spacing. PCL: non coated MEW scaffold; scaffolds are called PCL+RGD, PCL+IKVAV, and PCL + RGD+IKVAV refer RGD, IKVAV, a mixture of RGD and IKVAV coated MEW scaffolds, respectively.

Depending on their origin and developmental stage, astrocytes represent heterogeneous populations in the brain with different morphologies, functionalities, and biochemical profiles [23, 24]. The morphology of the astrocytes was controlled using scaffold designs and biochemical cues. The phenotypic changes of primary murine astrocytes were observed on MEW scaffolds regarding cell area and eccentricity (Figure 4). The largest cellular area was seen on triangle-shaped MEW scaffolds with 200 µm spacing. There was a significant difference between cellular areas of the box and triangle-shaped MEW scaffolds in both fiber spacing (Figure 4I). The eccentricity of the scaffolds differed significantly from each other; however, the

design of scaffolds in the same fiber spacing did not have any significant difference. The mixture of RGD and IKVAV coated scaffolds showed the largest cellular area and were significantly different from the other peptide-coated scaffolds (Figure 4K). Primary astrocytes on box-shaped MEW scaffolds with 200 µm fiber spacing formed cell clusters on the cross-section of the MEW fibers.

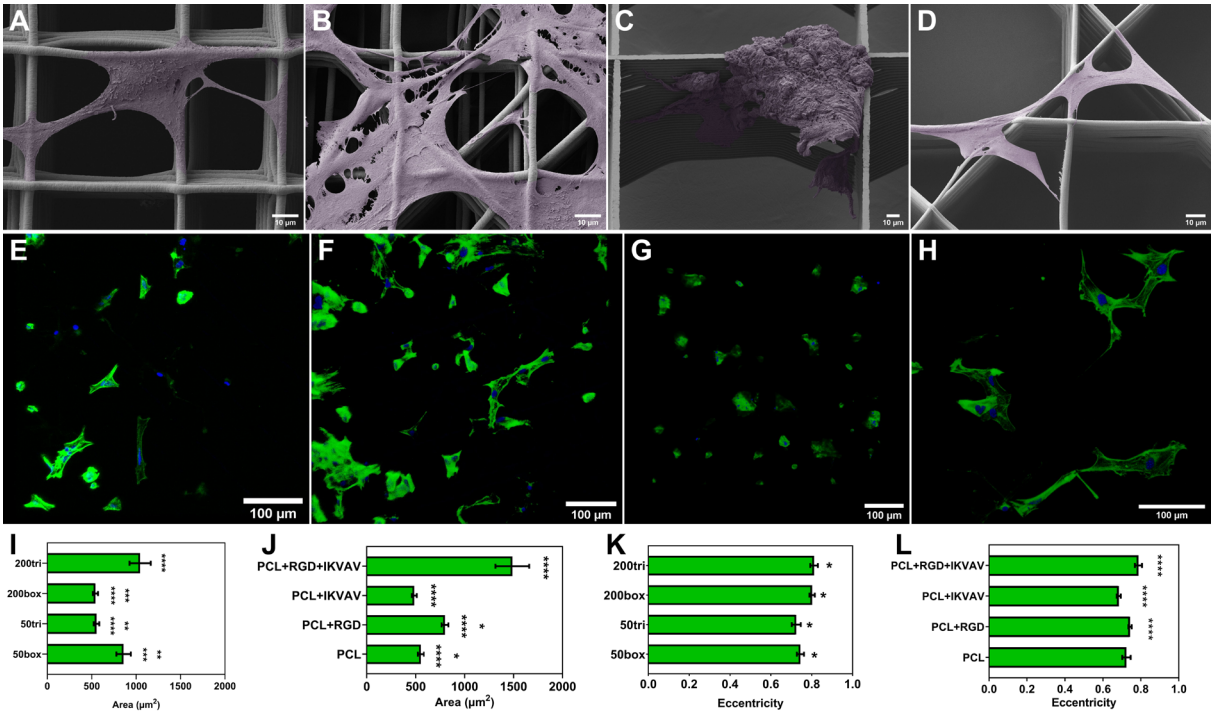

Figure 4. Primary astrocytes exhibited unique cellular morphology on MEW scaffolds. SEM images of A) box-shaped scaffold B) triangle-shaped scaffold with 50 µm fiber spacing C) box-shaped scaffold D) triangle-shaped scaffold with 200 µm fiber spacing. The confocal images of E) non-coated only PCL scaffold F) RGD (PCL+RGD) G) IKVAV (PCL+IKVAV) H) RGD+IKVAV (PCL+RGD+IKVAV) coated triangle-shaped MEW scaffold with 50 µm spacing. (Green: beta-actin, blue: DAPI) I- K) Size and shape-related metrics of the cells on different scaffold shape (Label code: 50box: Box-shaped scaffold with 50 µm fiber spacing, 50tri: Triangle shaped scaffolds with 50 µm fiber spacing, 200box: Box-shaped scaffolds with 200 µm fiber spacing, and 200tri: Triangle shape scaffold with 200 fiber spacing. PCL: non coated MEW scaffold, scaffolds are called PCL+RGD, PCL+IKVAV, and PCL+RGD+IKVAV refer RGD, IKVAV, a mixture of RGD and IKVAV coated MEW scaffolds, respectively).

Our results showed that the design of the scaffolds and the presence of the peptides are essential microenvironmental factors that influence the phenotypic transformation of astrocytes and U87. These data suggested that the cells have different characteristics that may reflect functional differences in the bioengineered

microenvironment due to the scaffolds' mechanical, biochemical, and topographical properties. Previous studies from Eichholz *et al*. showed that MEW scaffold designs affect cell morphology and it causes changes in the cellular activity of human skeletal stem cells. The study showed that the cells on the MEW scaffold patterned at 90° increased mineral production and ALP activity angles more than those angled at 45° or 10° or randomly oriented fibers [25]. Tourlomousis *et al*. used fibroblast as a model for yielding high cell shape homogeneity on MEW scaffolds [10].

Furthermore, several solution electrospinning studies showed that fiber surface topography could influence astrocytes' elongation and morphology changes [26, 27]. The fiber surface characteristics provide an additional tool to control and optimize astrocyte morphology. Based on these outcomes, many different MEW scaffold designs and peptide combinations can further study neurological diseases. In addition, more functional and mechanical analysis should be investigated for further evaluation of the study, such as mechanical analysis of scaffolds, gene and protein expression analysis, and immunofluorescent staining with specific markers such as glial fibrillary acidic protein for cells [28].

In contrast to triangle-shaped pores, astrocytes seeded into a box-shaped MEW scaffold with 200 µm spacing look more neurosphere-like structures, likely due to increased fiber spacing. The U87 cells on all the scaffolds showed migratory phenotypes on the fibers similar to a previous study [29]. There is an ongoing effort directed to fabricate *in vitro* models that provide insight into material-cell interactions to achieve phenotypic control and analysis [30]. The combination of biofabrication techniques and data analysis tools facilitates a new approach to tissue engineering that leads to uniform and predictable cell responses for many biomedical applications [31]. Precise control of *in vitro* models can overcome the challenges of translation to the clinic. For instance, cell interaction with the microenvironment control various cell cycles, differentiation, and function. Furthermore, cellular response changes are strongly influenced by the mechanical and topological properties of the matrix [32, 33]. Therefore 3D printing technologies facilities different design windows to alter the cell phenotypes which can improve to produce more *in vivo* like cell phenotypes *in vitro*.

3. Conclusion

This study developed an *in vitro* model using a flexible design option using small-diameter MEW fibers surface-coated with biological cues. A glioblastoma cell line and primary astrocytes were cultured on various MEW scaffolds to determine changes in the cell morphology, known to change depending on their microenvironment. The findings establish some base concepts that can be further developed to understand better the role of scaffold design and biochemical cues on brain cells. Furthermore, such *in vitro* outcomes could potentially be converted into a therapeutic approach *in vivo* for controlling tumor progression or glial scar formation following injury.

Experimental Section

Astrocytes and U87 cell culture

The glioma cell lines U87 (ATCC®) was cultured in MEM (Gibco™, Thermo Fisher Scientific, Waltham, MA, USA) with 10 % fetal bovine serum (Gibco™), 1 % L-glutamine, 1 % 1 M HEPES Buffer (Gibco™) and 1 % non-essential amino acids NEAA (Gibco™). Cells were incubated in a humidified atmosphere with 5% CO_2 at 37°C. Cells were passaged at 70-80% confluency using 0.025 % Trypsin (Gibco™).

Primary astrocytes were isolated at P0-P3 from CD1 mouse pups. Briefly, cortices were homogenized and put through a 70 µm cell strainer. Cells were counted, seeded in dishes, and cultured in DMEM supplemented with 10% fetal calf serum, 2 × 10−3 M GlutaMAX, 1 × 10−3 M sodium pyruvate, and 50 U mL^{-1} penicillin/streptomycin (Thermo Fisher Scientific, Waltham, United States) at 37 °C and 5% CO_2. The astrocytes were seeded on scaffolds one week later after first passaging. Experiments were authorized by the local veterinary authority and Committee on the Ethics of Animal Experiments (Regierung von Unterfranken).

MEW process

A custom-built MEW printer was used to fabricate scaffolds as previously described [18]. MEW was performed using medical-grade PCL (PURASORB PC 12, Lot#1712002224, 05/2018 Corbion Inc, Amsterdam, Netherlands) at 21±3°C and humidity of 35±12%. The parameters were used: 77°C; 2 bar of air pressure; 30 gauge nozzle; 4 kV voltage applied across a 1.4 mm collector distance for the scaffolds. The scaffold designs were named box and triangle-shaped MEW scaffolds, which related to laydown patterns, 0/90o and 0/45/90/135°, respectively.

sP(EO-stat-PO) coating of MEW scaffolds

PCL scaffolds were coated with RGD and IKVAV via NCO-sP(EO-stat-PO) monomer. The water and 100% ethanol were used for the pretreatment of the PCL scaffolds. Then scaffolds were kept in 1 M sodium hydroxide (NaOH) for 30 min, and they were incubated in 2% (wt%) sP(EO-stat-PO) solution for 10 min and kept in 2.5 mM cysteine-containing peptide solutions overnight. After that, the scaffolds were washed with PBS 5 times.

Contact angle measurements

Contact angle measurements (OCA 20, Dataphysics Instruments GmbH, Filderstadt, Germany) were performed to observe hydrophilicity changes with the coating. Briefly, 3 µL of water was placed on a 50 µm spacing scaffold, and then the shape of drops was analyzed using SCA 20 software (Dataphysics Instruments GmbH, Filderstadt, Germany).

Assessment of the peptide coating

To quantify the peptide bounding on the PCL fibers, the Pierce™ peptide assay (Thermo Fisher Scientific, Waltham) was performed according to the manufacturer's instructions with some modifications. Briefly, the scaffolds were incubated with 200 µL of working reagent in 1.5 mL reaction tubes for 30 min at

37°C, and immediately before measurements, the supernatant was transferred into a 96-well plate.

The reactive sP(EO-stat-PO) were incubated in a solution of a FITC dye, conjugated to a short cysteine-containing peptide sequence (Cys-Gly-Gly-Lys(FITC)) to observe the presence of peptides on the scaffolds after several washing steps. All the confocal images were taken using the identical laser power and gain.

Scanning electron microscopy

MEW scaffold samples were imaged using a Crossbeam 340 SEM equipped with GEMINI e-Beam column (Carl Zeiss Microscopy, Göttingen, Germany). Before imaging, the samples were sputter-coated with a 3.5 nm platinum layer (Leica EM ACE600, Wetzlar, Germany).

U87 glioblastoma cells and primary astrocytes were fixed with 6% glutaraldehyde for 15 min on ice after incubation for 2 and 7 days, respectively. The samples were then incubated 2 times PBS on ice before being dehydred with a graded ethanol series (from 70% to 100%). Following hexamethyldisilazane, air drying was performed. Then cells were sputter-coated with a 3.5 nm platinum layer before SEM imaging.

Actin staining of U87 and astrocytes

For cell morphology analysis, U87 cells were cultured on the MEW scaffolds for two days and fixed with 4% formaldehyde for 1 h at room temperature (RT). The samples were washed with PBS, then permeabilized with 0.1 % Triton X-100, blocking with 2% bovine serum albumin in PBS for 15 min at room temperature (RT). Cells were stained with Phalloidin-iFluor 555 Reagent (Abcam, Cambridge, U.K.) for 30 min at RT. Subsequently, samples were washed with PBS and mounted with a mounting medium containing DAPI (Dianova, Hamburg (Germany)). Astrocytes were stained with ActinGreen™ 488 ReadyProbes™ reagent. Astrocytes were cultured for 7 days on MEW scaffolds. At day 7, cells were fixed with 4% formaldehyde at RT for 15 min and blocked 1 h in PBS containing 3% goat serum and 0.1% Triton X-100.

The beta-actin stain was performed for 30 min in a blocking solution. Consequently, the constructs were washed with PBS Cells were stained with DAPI. Images were captured via confocal microscopy (TCS SP8, Leica, Wetzlar (Germany)).

Cell morphology analysis

The CellProfiler software was used to quantify cellular morphological features automatically. At least 50 cells were analyzed for each scaffold types. The z-stack images were pre-processed in ImageJ.

Statistical analysis

The determination of the statistical significance was performed by one-way analysis of variance (ANOVA). Results were considered significant at a p-value below 0.05 (*), below 0.01 (**), below 0.001 (***), below 0.0001 (****).

Acknowledgments

This work was supported by the German Research Foundation (DFG) as part of the Collaborative Research Centre SFB TRR225 (B01) as well as the DFG State Major Instrumentation Programme for funding the Zeiss Crossbeam CB 340 SEM (INST 105022/58-1 FUGG). The authors thank Philip Stahlhut for technical assistance with SEM imaging, while discussions are appreciated with Annalena Weiland and Prof. Dr. Reiner Strick.

References

1. Nikolakopoulou, P.; Rauti, R.; Voulgaris, D.; Shlomy, I.; Maoz, B. M.; Herland, A., Brain 2020, 143 (11), 3181-3213.
2. Beghi, E.; Giussani, G.; Nichols, E.; Abd-Allah, F.; Abdela, J.; Abdelalim, A.; Abraha, H. N.; Adib, M. G.; Agrawal, S.; Alahdab, F., The Lancet Neurology 2019, 18 (4), 357-375.
3. Ngo, M. T.; Harley, B. A., APL bioengineering 2021, 5 (2), 020902.
4. Liu, L.; Li, X.; Zhang, X.; Xu, T., Biofabrication 2020, 12 (3), 035008.
5. Bakirci, E.; Schaefer, N.; Dahri, O.; Hrynevich, A.; Strissel, P.; Strick, R.; Dalton, P. D.; Villmann, C., Advanced Biosystems 2020, 4 (10), 2000077.
6. Dalton, P. D.; Woodfield, T. B. F.; Mironov, V.; Groll, J., Adv Sci (Weinh) 2020, 7 (11), 1902953.
7. Bertlein, S.; Hochleitner, G.; Schmitz, M.; Tessmar, J.; Raghunath, M.; Dalton, P. D.; Groll, J., Advanced healthcare materials 2019, 8 (7), 1801544.
8. Olvera, D.; Sohrabi Molina, M.; Hendy, G.; Monaghan, M. G., Advanced Functional Materials 2020, 30 (44), 1909880.
9. Abbasi, N.; Hamlet, S.; Nguyen, N.-T., Journal of Science: Advanced Materials and Devices 2020, 5 (1), 30-39.
10. Tourlomousis, F.; Jia, C.; Karydis, T.; Mershin, A.; Wang, H.; Kalyon, D. M.; Chang, R. C., Microsystems & nanoengineering 2019, 5 (1), 1-19.
11. Hu, Y.; Huang, G.; Tian, J.; Qiu, J.; Jia, Y.; Feng, D.; Wei, Z.; Li, S.; Xu, F., NPG Asia Materials 2021, 13 (1), 1-15.
12. Dede Eren, A.; Vasilevich, A.; Eren, E. D.; Sudarsanam, P.; Tuvshindorj, U.; de Boer, J.; Foolen, J., Tissue Engineering Part A 2021, 27 (15-16), 1023-1036.
13. Carpenter, A. E.; Jones, T. R.; Lamprecht, M. R.; Clarke, C.; Kang, I. H.; Friman, O.; Guertin, D. A.; Chang, J. H.; Lindquist, R. A.; Moffat, J., Genome biology 2006, 7 (10), 1-11.
14. Robinson, T. M.; Hutmacher, D. W.; Dalton, P. D., Advanced Functional Materials 2019, 29 (44), 1904664.
15. Youssef, A.; Hrynevich, A.; Fladeland, L.; Balles, A.; Groll, J.; Dalton, P. D.; Zabler, S., Tissue Engineering Part C: Methods 2019, 25 (6), 367-379.
16. Castilho, M.; Mouser, V.; Chen, M.; Malda, J.; Ito, K., Acta biomaterialia 2019, 95, 297-306.
17. Janzen, D.; Bakirci, E.; Wieland, A.; Martin, C.; Dalton, P. D.; Villmann, C., Advanced healthcare materials 2020, 9 (9), 1901630.
18. Hrynevich, A.; Liashenko, I.; Dalton, P. D., Advanced Materials Technologies 2020, 5 (12), 2000772.

19. Kim, J.; Bakirci, E.; O'Neill, K. L.; Hrynevich, A.; Dalton, P. D., Macromolecular Materials and Engineering 2021, 306 (3), 2000685.
20. Ding, H.; Cao, K.; Zhang, F.; Boettcher, W.; Chang, R. C., Materials & Design 2019, 178, 107857.
21. Tylek, T.; Blum, C.; Hrynevich, A.; Schlegelmilch, K.; Schilling, T.; Dalton, P. D.; Groll, J., Biofabrication 2020, 12 (2), 025007.
22. Grafahrend, D.; Heffels, K.-H.; Beer, M. V.; Gasteier, P.; Möller, M.; Boehm, G.; Dalton, P. D.; Groll, J., Nature materials 2011, 10 (1), 67-73.
23. Sloan, S. A.; Barres, B. A., Current opinion in neurobiology 2014, 27, 75-81.
24. Bayraktar, O. A.; Fuentealba, L. C.; Alvarez-Buylla, A.; Rowitch, D. H., Cold Spring Harbor perspectives in biology 2015, 7 (1), a020362.
25. Eichholz, K. F.; Hoey, D. A., Acta biomaterialia 2018, 75, 140-151.
26. Puschmann, T. B.; Zandén, C.; De Pablo, Y.; Kirchhoff, F.; Pekna, M.; Liu, J.; Pekny, M., Glia 2013, 61 (3), 432-440.
27. Johnson, C. D.; D'Amato, A. R.; Puhl, D. L.; Wich, D. M.; Vesperman, A.; Gilbert, R. J., Biomedical Materials 2018, 13 (5), 054101.
28. Hara, M.; Kobayakawa, K.; Ohkawa, Y.; Kumamaru, H.; Yokota, K.; Saito, T.; Kijima, K.; Yoshizaki, S.; Harimaya, K.; Nakashima, Y., Nature medicine 2017, 23 (7), 818-828.
29. Wieland, A.; Strissel, P. L.; Schorle, H.; Bakirci, E.; Janzen, D.; Beckmann, M. W.; Eckstein, M.; Dalton, P. D.; Strick, R., Cancers 2021, 13 (20), 5144.
30. Vermeulen, S.; Honig, F.; Vasilevich, A.; Roumans, N.; Romero, M.; Dede Eren, A.; Tuvshindorj, U.; Alexander, M.; Carlier, A.; Williams, P., Advanced Materials 2021, 33 (31), 2102084.
31. Prendergast, M. E.; Burdick, J. A., Advanced Materials 2020, 32 (13), 1902516.
32. Stukel, J. M.; Willits, R. K., Tissue Engineering Part B: Reviews 2016, 22 (3), 173-182.
33. Gong, L.; Cao, L.; Shen, Z.; Shao, L.; Gao, S.; Zhang, C.; Lu, J.; Li, W., Advanced Materials 2018, 30 (17), 1705684.

4. Discussion and future perspectives

A significant challenge in the clinical translation of potential therapies for various diseases is the difference between *in vitro* observations and *in vivo* efficacy of the treatment [204]. Traditional 2D *in vitro* models often have difficulties accurately recapitulating the native or diseased tissue microenvironments. This issue is well-addressed by 3D *in vitro* models, which improve the investigation of the translational potential of drugs and treatments. Recent studies have shown that 3D *in vitro* models, such as spheroids, hydrogels, fiber constructs, and microfluidic organs on-chip, better mimic the cellular microenvironment than 2D *in vitro* models [205]. However, traditional *in vitro* 3D models cannot reproduce the dynamic, multicellular, and functionally complex architectures of tissues and organs. Therefore, it is critical to establish tissue-like miniatures with similar structural and functional properties to natural tissue for realistic 3D representations [3].

Biofabrication and its use of 3D printing offers a modern approach to design and fabricate complex tissue structures *in vitro*, enabling design flexibility, mass customization, multi-material fabrication, and advanced geometry [206]. Furthermore, it allows for the integration of different combinations of living cells in supporting matrices with precise control, resulting in the engineering of various tissues with promising biomedical applications. For example, MEW was used to produce neural cell elongation on suspended fibers [207], laser-based bioprinting was utilized to develop 3D coculture models of the interaction between cancer and endothelial cells [208]. In addition, each 3D technology has different strengths and weaknesses in resolution, fabrication time, and material windows [209]. Thus, it is beneficial to combine different biofabrication technologies to replicate the native tissue heterogeneity, with the capillary featuring integrated vascularization necessary for tissue development, maturation, and biological propagation. Recently, the group of Ozbolat has introduced a new hybrid bioprinting approach named aspiration-assisted bioprinting (AAB), which uses aspiration forces and allows printing a wide range of biologics (spheroids) with a range of dimensions (80μm - 800 μm) in precise control with minimal cell damage in/on a gel substrate [210, 211]. The combination of AAB technology with a second printing technology allows exploring different tissue-tissue and tissue-material interactions. Also, combining different extrusion-based technologies allows the production of multiphasic scaffolds, which is essential for

mimicking many tissues' hierarchical structures [212]. Therefore, hybrid biofabrication can be advantageous when designing and fabricating engineered tissue *in vitro* models [16]. However, these systems must go through several processing steps and optimizations for biomedical applications. Therefore, future research will enhance digital technologies such as artificial intelligence and machine learning [213] [214]. It is possible to use machine learning algorithms at various steps during the fabrication process [215]. For instance, machine learning algorithms can be used in patient imaging data searches to discover tissue structures that can be optimized for bioprinting, in drug discovery to find previously tested or failed trials for therapy, in precision medicine to develop *in vitro* models with individual genotypic and phenotypic characteristics, in material design to optimize printability requirements and more [216-218]. Using in silico simulations and digitalization in conjunction with developing *in vitro* systems will make biomedical research more human-relevant than using gold-standard animal models [219].

This doctoral thesis provides insight into the high-resolution 3D printing technology, MEW, and 3D printed *in vitro* models from material and bioengineering perspectives. For this purpose, the thesis has investigated expanding the MEW polymer library, improving the accuracy and precision of the MEW constructs using different process parameters, and improving the biological properties of MEW scaffolds to have more reproducible *in vitro* systems.

In contrast to many other biofabrication technologies, MEW has a unique resolution, design, precision, and excellent repeatability properties. Electrospinning and extrusion 3D printing have resolution limits for the fiber positioning and diameter, respectively [220, 221]. Depending on the printing parameters and polymer characteristics, the fiber diameters can be tailored between ≈0.8 and ≈100 µm with MEW [42]. The variety of polymers applied in this technique is still limited, with PCL being the current gold standard [129]. However, different applications require varying mechanical and biological properties of the materials. Therefore, an extended polymer library of MEW is crucial.

In the first manuscript, potential new materials for expanding the MEW polymer library were studied [222]. This study includes the processing of copolymers

based on hydrophilic PPO-PEG-PPO and hydrophobic PDMS segments. Such copolymer compositions provide tunable material properties, including wettability, surface roughness, mechanical properties, and cytotoxicity, depending on the content ratio of segments. The influence of different MEW processing parameters on fiber diameter was investigated for each copolymer. In this context, the results showed that each copolymer has different fiber morphology and surface properties depending on the ratio of hydrophobic and hydrophilic segments. In addition, the cytotoxicity of the copolymers was determined. The study revealed that increasing the number of hydrophilic segments increases the cytotoxicity of the copolymers. Furthermore, these copolymers have unique properties compared to other polymers reported for MEW, including thermal reversibility, a smooth surface, transparency, strong interlayer bonding between fibers, and tunable hydrophilic and hydrophobic behavior. It was shown that copolymers could be printed upon each other with good fiber fusion. This hybrid printing approach can be used for folding scaffolds for printing or capillary origami applications due to their adjustable wettability for future applications.

In the second manuscript, MEW was used to fabricate an *in vitro* device for rapid screening of glioblastoma cell migration [148]. PCL was utilized for the fabrication of the device. In the fabrication process, we investigated the influence of collector speed and the number of printed layers (i.e., wall height) on the accuracy, precision, and dimensional consistency of the radial migration device. A printing speed close to the CTS resulted in more accurate MEW constructs. Otherwise, the printing accuracy of the circle shape with MEW might be low due to the inward tilting of the walls and jet lag. In the literature, the researchers overcome inward tilted walls by modifying the G-codes [150]. According to our optimization process, the final radial migration device had a diameter of 9.4±0.1 mm, a wall height of around 350 µm, and a wall thickness of 17±1 µm. A human glioblastoma cell line, U87, was used for the competitive 3D *in vitro* radial culture device regarding cell growth and migration. Four different Matrigel concentrations within separate chambers facilitated U87 cells to determine a preferred matrix for migration and growth. The cells migrated through the 6 and 8 $mg\ mL^{-1}$ Matrigel concentrations. This device offers several possibilities to test different matrices easily with minimal volume in a competitive manner before performing a large experiment, which is essential for cost

and time efficiency. Furthermore, it is applicable for other cell types, and it could be a valuable tool to screen a spectrum of different matrices with additional automation for future direction.

The third manuscript includes MEW scaffolds which were used as models for studying the impact of the design and dimensions on phenotypes of glioblastoma cells and astrocytes. The results showed that MEW scaffolds with different designs and spacing affected the shape of cells. In addition, the MEW scaffolds were coated with different peptides such as IKVAV and RGD to investigate the effects of the biochemical cues. In the current study, we hypothesized that the culture of glioblastoma U87 and astrocytes in a manner that maintains phenotype depends on the substrate's designs and biochemical properties. To test this, we first screened different MEW scaffold designs and peptide coatings. The results showed that engineering a biomimetic substrate with mechanical and ECM-like properties promotes different phenotypes of glioblastoma U87 cells and astrocytes during *in vitro* culture. It is essential because it shows the ability to use physical and biochemical cues to expand both cells types, which could provide a potential pathway for generating large numbers of cells for future therapeutic applications. The next step could be to produce well-established *in vitro* models that provide insight into cell interactions to reach phenotypic control and analysis. Combining hybrid biofabrication techniques and data analysis tools facilitates a new tissue engineering approach leading to uniform and predictable cell responses for many biomedical applications [223]. Precise control over the *in vitro* models can overcome the challenges associated with a translation to the clinic using machine learning. For example, it has been shown that cell interaction with the ECM controls cell cycle, differentiation, and function for various cell types. The changes of cells are strongly influenced by the mechanical and topological properties of the matrix. Biofabrication can provide this precise chemical and mechanical microenvironment for cells, which is essential for a potentially homogeneous and reproducible cellular microenvironment for future translational research. The analysis data using different machine learning algorithms help to predict an ideal microenvironment without the necessity of performing a high number of experiments [200, 224].

Furthermore, surface modification is a common tool to improve the microenvironments of the cell-material interface to support an adhesive surface. Several surface modification approaches, including biomolecule loading, plasma treatment, and surface graft copolymerization, were utilized to improve MEW scaffolds' properties [78, 80]. MEW scaffolds were coated with signaling molecules, growth factors, peptides, and small molecules, resulting in more *in vivo* like cell morphologies *in vitro*. Furthermore, surface-modified scaffolds can be served as drug-loaded scaffolds for the local release of the drug, and the possibility for homing and differentiating stem cells.

Taken together, this thesis highlights essential avenues for the fabrication of *in vitro* models using high-resolution 3D printing techniques, MEW, including 1) extension of the polymer library for MEW, 2) design considerations, 3) hybrid approach, and controllable microenvironment for cell response.

5. Conclusion

This doctoral thesis has explored the potential of the MEW technology for *in vitro* models in various tissue engineering applications. The introduction reviewed the literature about *in vitro* models fabricated by the high-resolution 3D printing technology, MEW. The motivation of the thesis is highlighted, which is developing materials and *in vitro* models that can mimic the cellular microenvironment and be used for high-throughput analysis. The material and bioengineering approaches were used to address essential aspects: 1) extending MEW polymer library, 2) developing *in vitro* models to evaluate cell growth and migration toward the different matrices, and 3) studying the effect of scaffold designs and biochemical cues of microenvironments on cells.

In the first manuscript, a variety of amphiphilic segmented copolymers were melt electrowritten. All copolymers showed outstanding processability with MEW and unique properties, including thermal reversibility, a very smooth surface, transparency, strong interlayer bonding between fibers, and adjustable hydrophilic and hydrophobic behavior. The copolymers can extend the usage of MEW in different biochemical applications, including microfluidics, sensors, and devices.

In the second manuscript, MEW is used to fabricate 3D *in vitro* tools instead of fabricating scaffolds for the first time. We developed a 3D-printed radial device for determining the matrices that promote cell migration and growth. There are eight chambers in the device, and four different Matrigel concentrations are distributed among them. U87 glioblastoma cells are deposited into the cell depot. Cell growth and migration were monitored for eight days in all chambers. U87 cell growth and migration were promoted by 6 and 8 mg mL^{-1} Matrigel concentrations. Moreover, we systematically studied how design and process parameters affect the printing accuracy of radial devices. The results showed that collector speeds, design diameter, and the number of layers affect the accuracy and precision of the radial devices.

In the third manuscript, MEW scaffolds were precisely fabricated and coated with peptides using NCO-(sP(EO-stat-PO)). The influence of design and biochemical

cues on glioblastoma and astrocytes cell shapes were examined. The peptide coating using NCO-(sP(EO-stat-PO)) is simple. These results suggested that MEW scaffolds can be used as *in vitro* systems to understand the complex *in vivo* behavior of U87 cells and astrocytes. The adjustable properties of the MEW construct, such as fiber diameter, scaffold architecture, and the capacity to modify the fiber with different biochemical cues, enable to mimic cellular microenvironment in health and diseased conditions.

In summary, this thesis provides new aspects of using 3D printing-MEW to fabricate *in vitro* models for rapid screening for cell migration and manipulating cell shape through surface functionalities and scaffold architecture. These aspects have future potential to be used as a tool with data science to fabricate more tissue-like structures using hybrid biofabrication approaches.

6. References

1. Polykandriotis, E., L. Popescu, and R. Horch, *Regenerative medicine: then and now–an update of recent history into future possibilities.* Journal of cellular and molecular medicine, 2010. **14**(10): p. 2350-2358.
2. Berthiaume, F., T.J. Maguire, and M.L. Yarmush, *Tissue engineering and regenerative medicine: history, progress, and challenges.* Annual review of chemical and biomolecular engineering, 2011. **2**: p. 403-430.
3. Moroni, L., et al., *Biofabrication strategies for 3D in vitro models and regenerative medicine.* Nature Reviews Materials, 2018. **3**(5): p. 21-37.
4. Zhang, S., Z. Wan, and R.D. Kamm, *Vascularized organoids on a chip: strategies for engineering organoids with functional vasculature.* Lab on a Chip, 2021. **21**(3): p. 473-488.
5. Gomes, M.E., et al., *Tissue engineering and regenerative medicine: new trends and directions—a year in review.* Tissue Engineering Part B: Reviews, 2017. **23**(3): p. 211-224.
6. Huang, J., et al., *Role of molecular chemistry of degradable pHEMA hydrogels in three-dimensional biomimetic mineralization.* Chemistry of Materials, 2012. **24**(7): p. 1331-1337.
7. Ashammakhi, N., et al., *Minimally invasive and regenerative therapeutics.* Advanced Materials, 2019. **31**(1): p. 1804041.
8. Elsdale, T. and J. Bard, *Collagen substrata for studies on cell behavior.* The Journal of cell biology, 1972. **54**(3): p. 626-637.
9. Edmondson, R., et al., *Three-dimensional cell culture systems and their applications in drug discovery and cell-based biosensors.* Assay and drug development technologies, 2014. **12**(4): p. 207-218.
10. Elliott, N.T. and F. Yuan, *A review of three-dimensional in vitro tissue models for drug discovery and transport studies.* Journal of pharmaceutical sciences, 2011. **100**(1): p. 59-74.
11. Yang, B., et al., *Enhanced mechanosensing of cells in synthetic 3D matrix with controlled biophysical dynamics.* Nature Communications, 2021. **12**(1): p. 1-13.
12. Polonchuk, L., et al., *Cardiac spheroids as promising in vitro models to study the human heart microenvironment.* Scientific reports, 2017. **7**(1): p. 1-12.
13. Zadpoor, A.A. and J. Malda, *Additive manufacturing of biomaterials, tissues, and organs*. 2017, Springer.
14. Malda, J., et al., *25th anniversary article: engineering hydrogels for biofabrication.* Advanced materials, 2013. **25**(36): p. 5011-5028.
15. Mironov, V., et al., *Biofabrication: a 21st century manufacturing paradigm.* Biofabrication, 2009. **1**(2): p. 022001.
16. Dalton, P.D., et al., *Advances in hybrid fabrication toward hierarchical tissue constructs.* Advanced Science, 2020. **7**(11): p. 1902953.
17. Vyas, C., et al., *Engineering the vasculature with additive manufacturing.* Current Opinion in Biomedical Engineering, 2017. **2**: p. 1-13.
18. Ozbolat, I.T., *Scaffold-based or scaffold-free bioprinting: competing or complementing approaches?* Journal of Nanotechnology in Engineering and Medicine, 2015. **6**(2).
19. Hutmacher, D.W. and P.D. Dalton, *Melt electrospinning.* Chemistry–An Asian Journal, 2011. **6**(1): p. 44-56.
20. Brown, T.D., P.D. Dalton, and D.W. Hutmacher, *Melt electrospinning today: An opportune time for an emerging polymer process.* Progress in Polymer Science, 2016. **56**: p. 116-166.
21. Zhou, H., T.B. Green, and Y.L. Joo, *The thermal effects on electrospinning of polylactic acid melts.* Polymer, 2006. **47**(21): p. 7497-7505.
22. Deng, R., et al., *Melt electrospinning of low‐density polyethylene having a low‐melt flow index.* Journal of Applied Polymer Science, 2009. **114**(1): p. 166-175.

23. Brown, T.D., et al., *Design and fabrication of tubular scaffolds via direct writing in a melt electrospinning mode.* Biointerphases, 2012. **7**(1): p. 13.
24. Sampath, M., et al., *Curcumin loaded poly (lactic-co-glycolic) acid nanofiber for the treatment of carcinoma.* Colloids and surfaces B: biointerfaces, 2014. **117**: p. 128-134.
25. Fang, J., et al., *Needleless melt-electrospinning of polypropylene nanofibres.* Journal of nanomaterials, 2012. **2012**.
26. Buivydiene, D., et al., *Formation and characterisation of air filter material printed by melt electrospinning.* Journal of Aerosol Science, 2019. **131**: p. 48-63.
27. Sarbatly, R., D. Krishnaiah, and Z. Kamin, *A review of polymer nanofibres by electrospinning and their application in oil–water separation for cleaning up marine oil spills.* Marine pollution bulletin, 2016. **106**(1-2): p. 8-16.
28. Shi, F., C. Chen, and Z.-L. Xu, *Recent Advances on Electrospun Nanofiber Materials for Post-lithium Ion Batteries.* Advanced Fiber Materials, 2021: p. 1-27.
29. Chen, Q., et al., *Direct write micro/nano optical fibers by near-field melt electrospinning.* Optics letters, 2017. **42**(24): p. 5106-5109.
30. Li, H. and W. Yang, *Electrospinning technology in non-woven fabric manufacturing.* Non-woven fabrics, 2016: p. 33.
31. Muerza-Cascante, M.L., et al., *Melt electrospinning and its technologization in tissue engineering.* Tissue Engineering Part B: Reviews, 2015. **21**(2): p. 187-202.
32. Cao, K., et al., *PLLA-PHB fiber membranes obtained by solvent-free electrospinning for short-time drug delivery.* Drug delivery and translational research, 2018. **8**(1): p. 291-302.
33. Lian, H. and Z. Meng, *Melt electrospinning of daunorubicin hydrochloride-loaded poly (ε-caprolactone) fibrous membrane for tumor therapy.* Bioactive materials, 2017. **2**(2): p. 96-100.
34. Yarin, A.L., S. Koombhongse, and D.H. Reneker, *Taylor cone and jetting from liquid droplets in electrospinning of nanofibers.* Journal of applied physics, 2001. **90**(9): p. 4836-4846.
35. Shin, Y., et al., *Electrospinning: A whipping fluid jet generates submicron polymer fibers.* Applied physics letters, 2001. **78**(8): p. 1149-1151.
36. Reneker, D.H., et al., *Bending instability of electrically charged liquid jets of polymer solutions in electrospinning.* Journal of Applied physics, 2000. **87**(9): p. 4531-4547.
37. Garg, K. and G.L. Bowlin, *Electrospinning jets and nanofibrous structures.* Biomicrofluidics, 2011. **5**(1): p. 013403.
38. Großhaus, C., et al., *Melt Electrospinning of Nanofibers from Medical‐Grade Poly (ε‐Caprolactone) with a Modified Nozzle.* Small, 2020. **16**(44): p. 2003471.
39. Dalton, P.D., *Melt electrowriting with additive manufacturing principles.* Current Opinion in Biomedical Engineering, 2017. **2**: p. 49-57.
40. Hochleitner, G., et al., *Fibre pulsing during melt electrospinning writing.* BioNanoMaterials, 2016. **17**(3-4): p. 159-171.
41. Hrynevich, A., et al., *Dimension‐based design of melt electrowritten scaffolds.* Small, 2018. **14**(22): p. 1800232.
42. Robinson, T.M., D.W. Hutmacher, and P.D. Dalton, *The next frontier in melt electrospinning: taming the jet.* Advanced Functional Materials, 2019. **29**(44): p. 1904664.
43. Mechau, J., et al., *Hydrophilic (AB) n Segmented Copolymers for Melt Extrusion‐Based Additive Manufacturing.* Macromolecular Chemistry and Physics, 2021. **222**(1): p. 2000265.
44. Brown, T.D., P.D. Dalton, and D.W. Hutmacher, *Direct writing by way of melt electrospinning.* Advanced Materials, 2011. **23**(47): p. 5651-5657.
45. Dayan, C.B., et al., *Modeling 3D melt electrospinning writing by response surface methodology.* Materials & Design, 2018. **148**: p. 87-95.
46. Mieszczanek, P., et al., *Convergence of Machine Vision and Melt Electrowriting.* Advanced Materials: p. 2100519.

47. Ding, H., et al., *A fundamental study of charge effects on melt electrowritten polymer fibers.* Materials & Design, 2019. **178**: p. 107857.
48. Cao, K., F. Zhang, and R.C. Chang, *A Charge-Based Mechanistic Study into the Effects of Process Parameters on Fiber Accumulating Geometry for a Melt Electrohydrodynamic Process.* Processes, 2020. **8**(11): p. 1440.
49. Kim, J., et al., *Fiber Bridging during Melt Electrowriting of Poly (ε-Caprolactone) and the Influence of Fiber Diameter and Wall Height.* Macromolecular Materials and Engineering, 2021. **306**(3): p. 2000685.
50. Saidy, N.T., et al., *Melt Electrowriting of Complex 3D Anatomically Relevant Scaffolds.* Front Bioeng Biotechnol, 2020. **8**: p. 793.
51. Peiffer, Q.C., et al., *Melt electrowriting onto anatomically relevant biodegradable substrates: Resurfacing a diarthrodial joint.* Mater Des, 2020. **195**: p. 109025.
52. Saha, U., et al., *A Deeper Insight into the Influence of the Electric Field Strength When Melt-Electrowriting on Non-Planar Surfaces.* Macromolecular Materials and Engineering, 2021: p. 2100496.
53. Nairn, R., et al., *A deeper insight into the influence of the electric field densities in Melt-Electrowriting: Printing in the 4th Dimension.* 2021.
54. O'Connell, C.D., et al., *Electrostatic Distortion of Melt-Electrowritten Patterns by 3D Objects: Quantification, Modeling, and Toolpath Correction.* Advanced Materials Technologies, 2021: p. 2100345.
55. Florczak, S., et al., *Melt electrowriting of electroactive poly (vinylidene difluoride) fibers.* Polymer International, 2019. **68**(4): p. 735-745.
56. Haigh, J.N., T.R. Dargaville, and P.D. Dalton, *Additive manufacturing with polypropylene microfibers.* Materials Science and Engineering: C, 2017. **77**: p. 883-887.
57. Sanchez Diaz, R., et al., *Highly Elastic Scaffolds Produced by Melt Electrowriting of Poly (L-lactide-co-ε-caprolactone).* Advanced Materials Technologies, 2021: p. 2100508.
58. Nahm, D., et al., *A versatile biomaterial ink platform for the melt electrowriting of chemically-crosslinked hydrogels.* Materials Horizons, 2020. **7**(3): p. 928-933.
59. Hochleitner, G., et al., *Melt electrowriting of thermoplastic elastomers.* Macromolecular rapid communications, 2018. **39**(10): p. 1800055.
60. Kade, J.C., et al., *Melt electrowriting of poly (vinylidene difluoride) using a heated collector.* Polymers for Advanced Technologies, 2021.
61. Kade, J., et al., *Melt Electrowriting of Poly (vinylidene fluoride-co-trifluoroethylene).* 2021.
62. Hochleitner, G., et al., *High definition fibrous poly (2-ethyl-2-oxazoline) scaffolds through melt electrospinning writing.* Polymer, 2014. **55**(20): p. 5017-5023.
63. Haigh, J.N., et al., *Hierarchically Structured Porous Poly (2-oxazoline) Hydrogels.* Macromolecular rapid communications, 2016. **37**(1): p. 93-99.
64. Meng, J., et al., *Design and manufacturing of 3D high-precision micro-fibrous poly (l-lactic acid) scaffold using melt electrowriting technique for bone tissue engineering.* Materials & Design, 2021. **210**: p. 110063.
65. Nadernezhad, A., et al., *Melt Electrowriting of Isomalt for High-Resolution Templating of Embedded Microchannels.* Advanced Materials Technologies, 2021: p. 2100221.
66. Chen, F., et al., *Additive manufacturing of a photo-cross-linkable polymer via direct melt electrospinning writing for producing high strength structures.* Biomacromolecules, 2016. **17**(1): p. 208-214.
67. Hochleitner, G., et al., *Melt electrowriting below the critical translation speed to fabricate crimped elastomer scaffolds with non-linear extension behaviour mimicking that of ligaments and tendons.* Acta Biomater, 2018. **72**: p. 110-120.
68. Shao, Z., et al. *Research on Melt Electrowriting TPU Hydrophobic Microfiber Mesh for Directional Water Transport*. in *2021 IEEE 16th International Conference on Nano/Micro Engineered and Molecular Systems (NEMS)*. 2021. IEEE.

69. Abdal-hay, A., et al., *Novel polycaprolactone/hydroxyapatite nanocomposite fibrous scaffolds by direct melt-electrospinning writing.* European Polymer Journal, 2018. **105**: p. 257-264.
70. Paxton, N.C., et al., *Rheological characterization of biomaterials directs additive manufacturing of strontium-substituted bioactive glass/polycaprolactone microfibers.* Macromolecular rapid communications, 2019. **40**(11): p. 1900019.
71. Hewitt, E., et al., *Melt-electrowriting with novel milk protein/PCL biomaterials for skin regeneration.* Biomed Mater, 2019. **14**(5): p. 055013.
72. Hochleitner, G., et al., *Melt electrospinning writing of defined scaffolds using polylactide-poly (ethylene glycol) blends with 45S5 bioactive glass particles.* Materials Letters, 2017. **205**: p. 257-260.
73. Mueller, K.M.A., et al., *Visualization of USPIO-labeled melt-electrowritten scaffolds by non-invasive magnetic resonance imaging.* Biomaterials Science, 2021.
74. Bai, J., et al., *Melt electrohydrodynamic 3D printed poly (ε-caprolactone)/polyethylene glycol/roxithromycin scaffold as a potential anti-infective implant in bone repair.* International journal of pharmaceutics, 2020. **576**: p. 118941.
75. Yoshida, M., et al., *Three-Dimensional Melt-Electrowritten Polycaprolactone/Chitosan Scaffolds Enhance Mesenchymal Stem Cell Behavior.* ACS Applied Bio Materials, 2021. **4**(2): p. 1319-1329.
76. Hammerl, A., et al., *A growth factor-free co-culture system of osteoblasts and peripheral blood mononuclear cells for the evaluation of the osteogenesis potential of melt-electrowritten polycaprolactone scaffolds.* International journal of molecular sciences, 2019. **20**(5): p. 1068.
77. Daghrery, A., et al., *A Highly Ordered, Nanostructured Fluorinated CaP-Coated Melt Electrowritten Scaffold for Periodontal Tissue Regeneration.* Advanced Healthcare Materials, 2021: p. 2101152.
78. Abbasi, N., S. Hamlet, and N.-T. Nguyen, *Calcium phosphate stability on melt electrowritten PCL scaffolds.* Journal of Science: Advanced Materials and Devices, 2020. **5**(1): p. 30-39.
79. Olvera, D., et al., *Electroconductive melt electrowritten patches matching the mechanical anisotropy of human myocardium.* Advanced Functional Materials, 2020. **30**(44): p. 1909880.
80. Eichholz, K.F., et al., *Development of a New Bone-Mimetic Surface Treatment Platform: Nanoneedle Hydroxyapatite (nnHA) Coating.* Advanced Healthcare Materials, 2020. **9**(24): p. 2001102.
81. Eichholz, K.F., et al., *Extracellular Vesicle Functionalized Melt Electrowritten Scaffolds for Bone Tissue Engineering.* Advanced NanoBiomed Research, 2021: p. 2100037.
82. Zhang, Z., et al., *3D anisotropic photocatalytic architectures as bioactive nerve guidance conduits for peripheral neural regeneration.* Biomaterials, 2020. **253**: p. 120108.
83. Bertlein, S., et al., *Permanent hydrophilization and generic bioactivation of melt electrowritten scaffolds.* Advanced healthcare materials, 2019. **8**(7): p. 1801544.
84. Blum, C., et al., *Extracellular matrix-modified fiber scaffolds as a proadipogenic mesenchymal stromal cell delivery platform.* ACS biomaterials science & engineering, 2019. **5**(12): p. 6655-6666.
85. Bas, O., et al., *An integrated design, material, and fabrication platform for engineering biomechanically and biologically functional soft tissues.* ACS applied materials & interfaces, 2017. **9**(35): p. 29430-29437.
86. Visser, J., et al., *Reinforcement of hydrogels using three-dimensionally printed microfibres.* Nature communications, 2015. **6**(1): p. 1-10.
87. Kristen, M., et al., *Fiber scaffold patterning for mending hearts: 3D organization bringing the next step.* Advanced healthcare materials, 2020. **9**(1): p. 1900775.
88. Dubey, N., et al., *Highly tunable bioactive fiber-reinforced hydrogel for guided bone regeneration.* Acta Biomaterialia, 2020. **113**: p. 164-176.

89. Chen, M., et al., *Multiscale modelling and homogenisation of fibre-reinforced hydrogels for tissue engineering.* European journal of applied mathematics, 2020. **31**(1): p. 143-171.
90. Castilho, M., et al., *Mechanical behavior of a soft hydrogel reinforced with three-dimensional printed microfibre scaffolds.* Scientific reports, 2018. **8**(1): p. 1-10.
91. de Ruijter, M., et al., *Out‐of‐Plane 3D‐Printed Microfibers Improve the Shear Properties of Hydrogel Composites.* Small, 2018. **14**(8): p. 1702773.
92. Bas, O., et al., *Enhancing structural integrity of hydrogels by using highly organised melt electrospun fibre constructs.* European Polymer Journal, 2015. **72**: p. 451-463.
93. Saidy, N.T., et al., *Biologically Inspired Scaffolds for Heart Valve Tissue Engineering via Melt Electrowriting.* Small, 2019. **15**(24): p. e1900873.
94. Castilho, M., et al., *Melt electrowriting allows tailored microstructural and mechanical design of scaffolds to advance functional human myocardial tissue formation.* Advanced Functional Materials, 2018. **28**(40): p. 1803151.
95. Schaefer, N., et al., *3D Electrophysiological Measurements on Cells Embedded within Fiber‐Reinforced Matrigel.* Advanced healthcare materials, 2019. **8**(5): p. 1801226.
96. Janzen, D., et al., *Cortical Neurons form a Functional Neuronal Network in a 3D Printed Reinforced Matrix.* Advanced healthcare materials, 2020. **9**(9): p. 1901630.
97. Fischhaber, N., et al., *Spinal Cord Neuronal Network Formation in a 3D Printed Reinforced Matrix—A Model System to Study Disease Mechanisms.* Advanced Healthcare Materials: p. 2100830.
98. de Ruijter, M., et al., *Simultaneous micropatterning of fibrous meshes and bioinks for the fabrication of living tissue constructs.* Advanced healthcare materials, 2019. **8**(7): p. 1800418.
99. Diloksumpan, P., et al., *Combining multi-scale 3D printing technologies to engineer reinforced hydrogel-ceramic interfaces.* Biofabrication, 2020. **12**(2): p. 025014.
100. Ross, M.T., et al., *Using melt-electrowritten microfibres for tailoring scaffold mechanics of 3D bioprinted chondrocyte-laden constructs.* Bioprinting, 2021. **23**: p. e00158.
101. Jungst, T., et al., *Heterotypic scaffold design orchestrates primary cell organization and phenotypes in cocultured small diameter vascular grafts.* Advanced Functional Materials, 2019. **29**(43): p. 1905987.
102. McMaster, R., et al., *Tailored Melt Electrowritten Scaffolds for the Generation of Sheet‐Like Tissue Constructs from Multicellular Spheroids.* Advanced healthcare materials, 2019. **8**(7): p. 1801326.
103. Han, Y., et al., *High-precision, gelatin-based, hybrid, bilayer scaffolds using melt electro-writing to repair cartilage injury.* Bioactive materials, 2021. **6**(7): p. 2173-2186.
104. Wang, Z., et al., *Fabrication and in vitro evaluation of PCL/gelatin hierarchical scaffolds based on melt electrospinning writing and solution electrospinning for bone regeneration.* Materials Science and Engineering: C, 2021. **128**: p. 112287.
105. Tourlomousis, F., et al., *Machine learning metrology of cell confinement in melt electrowritten three-dimensional biomaterial substrates.* Microsystems & nanoengineering, 2019. **5**(1): p. 1-19.
106. Turner, P.R., et al., *Melt Electrowritten Sandwich Scaffold Technique Using Sulforhodamine B to Monitor Stem Cell Behavior.* Tissue Engineering Part C: Methods, 2020. **26**(10): p. 519-527.
107. Abbasi, N., et al., *Effects of gradient and offset architectures on the mechanical and biological properties of 3-D melt electrowritten (MEW) scaffolds.* ACS Biomaterials Science & Engineering, 2019. **5**(7): p. 3448-3461.
108. Abbasi, N., et al., *Role of offset and gradient architectures of 3-D melt electrowritten scaffold on differentiation and mineralization of osteoblasts.* Biomaterials research, 2020. **24**(1): p. 1-16.
109. Jørgensen, M., et al., *A melt-electrowritten filter for capture and culture of circulating colon cancer cells.* Materials Today Bio, 2020. **6**: p. 100052.

110. Ryma, M., et al., *Translation of Collagen Ultrastructure to Biomaterial Fabrication for Material‐Independent but Highly Efficient Topographic Immunomodulation.* Advanced Materials, 2021. **33**(33): p. 2101228.
111. Muerza-Cascante, M.L., et al., *Endosteal-like extracellular matrix expression on melt electrospun written scaffolds.* Acta biomaterialia, 2017. **52**: p. 145-158.
112. Constante, G., et al., *4D Biofabrication Using a Combination of 3D Printing and Melt-Electrowriting of Shape-Morphing Polymers.* ACS Appl Mater Interfaces, 2021. **13**(11): p. 12767-12776.
113. Uribe-Gomez, J., et al., *Shape-morphing fibrous hydrogel/elastomer bilayers fabricated by a combination of 3D printing and melt electrowriting for muscle tissue regeneration.* ACS Applied Bio Materials, 2021. **4**(2): p. 1720-1730.
114. Su, Y., et al., *A hierarchically ordered compacted coil scaffold for tissue regeneration.* NPG Asia Materials, 2020. **12**(1): p. 1-10.
115. Abbasi, N., et al., *In vivo bone regeneration assessment of offset and gradient melt electrowritten (MEW) PCL scaffolds.* Biomaterials research, 2020. **24**(1): p. 1-24.
116. Wang, S., et al., *Hydrogels with cell adhesion peptide‐decorated channel walls for cell guidance.* Macromolecular Rapid Communications, 2020. **41**(15): p. 2000295.
117. Zeng, J., et al., *Fabrication of microfluidic channels based on melt-electrospinning direct writing.* Microfluidics and Nanofluidics, 2018. **22**(2): p. 1-10.
118. Kotz, F., et al., *Fabrication of arbitrary three-dimensional suspended hollow microstructures in transparent fused silica glass.* Nature communications, 2019. **10**(1): p. 1-7.
119. Su, Y., et al., *Melt Electrospinning Writing of Magnetic Microrobots.* Advanced Science, 2021. **8**(3): p. 2003177.
120. Hutmacher, D., et al., *Ultrafast Soft Actuators.* 2021.
121. Xiong, J., J. Chen, and P.S. Lee, *Functional fibers and fabrics for soft robotics, wearables, and human–robot interface.* Advanced Materials, 2021. **33**(19): p. 2002640.
122. Georgopoulou, A., et al. *A Sensorized Soft Pneumatic Actuator Fabricated with Extrusion-Based Additive Manufacturing*. in *Actuators*. 2021. Multidisciplinary Digital Publishing Institute.
123. Zhu, Z., H.S. Park, and M.C. McAlpine, *3D printed deformable sensors.* Sci Adv, 2020. **6**(25): p. eaba5575.
124. Youssef, A., S.J. Hollister, and P.D. Dalton, *Additive manufacturing of polymer melts for implantable medical devices and scaffolds.* Biofabrication, 2017. **9**(1): p. 012002.
125. Hutmacher, D.W., *Scaffolds in tissue engineering bone and cartilage.* Biomaterials, 2000. **21**(24): p. 2529-2543.
126. Ngo, T.D., et al., *Additive manufacturing (3D printing): A review of materials, methods, applications and challenges.* Composites Part B: Engineering, 2018. **143**: p. 172-196.
127. Hochleitner, G., et al., *Additive manufacturing of scaffolds with sub-micron filaments via melt electrospinning writing.* Biofabrication, 2015. **7**(3): p. 035002.
128. Rainer, A. and L. Moroni, *Computer aided tissue engineering: methods and protocols: volume 2147*. 2021: Springer.
129. Kade, J.C. and P.D. Dalton, *Polymers for Melt Electrowriting.* Adv Healthc Mater, 2021. **10**(1): p. e2001232.
130. Ratner, B.D. and S.J. Bryant, *Biomaterials: where we have been and where we are going.* Annu. Rev. Biomed. Eng., 2004. **6**: p. 41-75.
131. Hoffman, A., *Hydrogel biomedical articles.* Adv. Drug Deliv. Rev, 2002. **54**(90): p. 3-12.
132. Hu, W., et al., *Mussel-inspired copolymer-coated polypropylene mesh with anti-adhesion efficiency for abdominal wall defect repair.* Biomaterials science, 2019. **7**(4): p. 1323-1334.
133. Swartzlander, M.D., et al., *Linking the foreign body response and protein adsorption to PEG-based hydrogels using proteomics.* Biomaterials, 2015. **41**: p. 26-36.

134. Miller, J.S., et al., *Rapid casting of patterned vascular networks for perfusable engineered three-dimensional tissues.* Nature materials, 2012. **11**(9): p. 768-774.
135. Grigoryan, B., et al., *Multivascular networks and functional intravascular topologies within biocompatible hydrogels.* Science, 2019. **364**(6439): p. 458-464.
136. Lorson, T., et al., *A thermogelling supramolecular hydrogel with sponge-like morphology as a cytocompatible bioink.* Biomacromolecules, 2017. **18**(7): p. 2161-2171.
137. He, J., et al., *Microscale Electro-Hydrodynamic Cell Printing with High Viability.* Small, 2017. **13**(47): p. 1702626.
138. Castilho, M., et al., *Hydrogel-based bioinks for cell electrowriting of well-organized living structures with micrometer-scale resolution.* Biomacromolecules, 2021. **22**(2): p. 855-866.
139. Pawar, G.M., et al., *Injectable hydrogels from segmented PEG-bisurea copolymers.* Biomacromolecules, 2012. **13**(12): p. 3966-3976.
140. Koenig, K., et al., *A new prototype melt-electrospinning device for the production of biobased thermoplastic sub-microfibers and nanofibers.* Biomaterials research, 2019. **23**(1): p. 1-12.
141. Bas, O., et al., *Biofabricated soft network composites for cartilage tissue engineering.* Biofabrication, 2017. **9**(2): p. 025014.
142. Fürsattel, E.M., *Extrusion-based melt processing of (AB) n segmented poly (urea-siloxane) s and their modification towards amphiphilic hydrogels*. 2021.
143. Hrynevich, A., I. Liashenko, and P.D. Dalton, *Accurate prediction of melt electrowritten laydown patterns from simple geometrical considerations.* Advanced Materials Technologies, 2020. **5**(12): p. 2000772.
144. Skylar-Scott, M.A., et al., *Voxelated soft matter via multimaterial multinozzle 3D printing.* Nature, 2019. **575**(7782): p. 330-335.
145. Blum, C., et al., *Controlling Topography and Crystallinity of Melt Electrowritten Poly (ε-Caprolactone) Fibers.* 3D Printing and Additive Manufacturing, 2021.
146. Sami, S., et al., *Understanding the influence of hydrogen bonding and diisocyanate symmetry on the morphology and properties of segmented polyurethanes and polyureas: Computational and experimental study.* Polymer, 2014. **55**(18): p. 4563-4576.
147. Candau, N., et al., *Mechanical reinforcement and memory effect of strain-induced soft segment crystals in thermoplastic polyurethane-urea elastomers.* Polymer, 2021. **223**: p. 123708.
148. Bakirci, E., et al., *Melt electrowritten in vitro radial device to study cell growth and migration.* Advanced Biosystems, 2020. **4**(10): p. 2000077.
149. Castan, L., et al., *Comparative study of cytotoxicity and genotoxicity of commercial Jeffamines® and polyethylenimine in CHO-K1 cells.* Journal of Biomedical Materials Research Part B: Applied Biomaterials, 2018. **106**(2): p. 742-750.
150. Liashenko, I., A. Hrynevich, and P.D. Dalton, *Designing Outside the Box: Unlocking the Geometric Freedom of Melt Electrowriting using Microscale Layer Shifting.* Adv Mater, 2020. **32**(28): p. e2001874.
151. Williams, D., *Tissue Engineering*. 2008, Burlington: Academic Press.
152. Daley, W.P. and K.M. Yamada, *ECM-modulated cellular dynamics as a driving force for tissue morphogenesis.* Current opinion in genetics & development, 2013. **23**(4): p. 408-414.
153. Yamada, K.M. and M. Sixt, *Mechanisms of 3D cell migration.* Nature Reviews Molecular Cell Biology, 2019. **20**(12): p. 738-752.
154. Bellail, A.C., et al., *Microregional extracellular matrix heterogeneity in brain modulates glioma cell invasion.* The international journal of biochemistry & cell biology, 2004. **36**(6): p. 1046-1069.
155. Chen, R., et al., *Glioma subclassifications and their clinical significance.* Neurotherapeutics, 2017. **14**(2): p. 284-297.
156. Farin, A., et al., *Transplanted glioma cells migrate and proliferate on host brain vasculature: a dynamic analysis.* Glia, 2006. **53**(8): p. 799-808.

157. Jain, A., et al., *Guiding intracortical brain tumour cells to an extracortical cytotoxic hydrogel using aligned polymeric nanofibres.* Nature materials, 2014. **13**(3): p. 308-316.
158. Stroka, K.M., et al., *Bioengineering paradigms for cell migration in confined microenvironments.* Current opinion in cell biology, 2014. **30**: p. 41-50.
159. Wei, S.C., et al., *Matrix stiffness drives epithelial–mesenchymal transition and tumour metastasis through a TWIST1–G3BP2 mechanotransduction pathway.* Nature cell biology, 2015. **17**(5): p. 678-688.
160. Xu, H., X. Liu, and W. Le, *Recent advances in microfluidic models for cancer metastasis research.* TrAC Trends in Analytical Chemistry, 2018. **105**: p. 1-6.
161. Pollard, T.D. and G.G. Borisy, *Cellular motility driven by assembly and disassembly of actin filaments.* Cell, 2003. **112**(4): p. 453-465.
162. Winkler, B., I.S. Aranson, and F. Ziebert, *Confinement and substrate topography control cell migration in a 3D computational model.* Communications Physics, 2019. **2**(1): p. 1-11.
163. Mierke, C.T., *The matrix environmental and cell mechanical properties regulate cell migration and contribute to the invasive phenotype of cancer cells.* Reports on Progress in Physics, 2019. **82**(6): p. 064602.
164. Liang, C.-C., A.Y. Park, and J.-L. Guan, *In vitro scratch assay: a convenient and inexpensive method for analysis of cell migration in vitro.* Nature protocols, 2007. **2**(2): p. 329-333.
165. Mak, M., C.A. Reinhart-King, and D. Erickson, *Elucidating mechanical transition effects of invading cancer cells with a subnucleus-scaled microfluidic serial dimensional modulation device.* Lab on a Chip, 2013. **13**(3): p. 340-348.
166. Duong, L.H. and P.-C. Chen, *Simple and low-cost production of hybrid 3D-printed microfluidic devices.* Biomicrofluidics, 2019. **13**(2): p. 024108.
167. Youssef, A., et al., *The impact of melt electrowritten scaffold design on porosity determined by x-ray microtomography.* Tissue Engineering Part C: Methods, 2019. **25**(6): p. 367-379.
168. Wunner, F.M., et al., *Melt electrospinning writing of highly ordered large volume scaffold architectures.* Advanced Materials, 2018. **30**(20): p. 1706570.
169. Zhang, G., et al., *High-Resolution Electric-Field-Driven Jet 3D Printing and Applications.* 3D Printing, 2018: p. 23.
170. Ma, H., H. Xu, and J. Qin, *Biomimetic tumor microenvironment on a microfluidic platform.* Biomicrofluidics, 2013. **7**(1): p. 011501.
171. Wang, C., X. Tong, and F. Yang, *Bioengineered 3D brain tumor model to elucidate the effects of matrix stiffness on glioblastoma cell behavior using PEG-based hydrogels.* Molecular pharmaceutics, 2014. **11**(7): p. 2115-2125.
172. Pogoda, K., et al., *Soft substrates containing hyaluronan mimic the effects of increased stiffness on morphology, motility, and proliferation of glioma cells.* Biomacromolecules, 2017. **18**(10): p. 3040-3051.
173. Moshayedi, P., et al., *The relationship between glial cell mechanosensitivity and foreign body reactions in the central nervous system.* Biomaterials, 2014. **35**(13): p. 3919-3925.
174. Barnes, J.M., L. Przybyla, and V.M. Weaver, *Tissue mechanics regulate brain development, homeostasis and disease.* Journal of cell science, 2017. **130**(1): p. 71-82.
175. Reid, S.E., et al., *Tumor matrix stiffness promotes metastatic cancer cell interaction with the endothelium.* The EMBO journal, 2017. **36**(16): p. 2373-2389.
176. Wood, M.D., et al., *Heparin-binding-affinity-based delivery systems releasing nerve growth factor enhance sciatic nerve regeneration.* Journal of Biomaterials Science, Polymer Edition, 2010. **21**(6-7): p. 771-787.
177. Liu, T.-L., et al., *Observing the cell in its native state: Imaging subcellular dynamics in multicellular organisms.* Science, 2018. **360**(6386).

178. Truong, D.D., et al., *A human organotypic microfluidic tumor model permits investigation of the interplay between patient-derived fibroblasts and breast cancer cells.* Cancer research, 2019. **79**(12): p. 3139-3151.
179. Grafahrend, D., et al., *Biofunctionalized poly (ethylene glycol)-block-poly (ε-caprolactone) nanofibers for tissue engineering.* Journal of Materials Science: Materials in Medicine, 2008. **19**(4): p. 1479-1484.
180. Sakiyama, S.E., J.C. Schense, and J.A. Hubbell, *Incorporation of heparin-binding peptides into fibrin gels enhances neurite extension: an example of designer matrices in tissue engineering.* The FASEB Journal, 1999. **13**(15): p. 2214-2224.
181. Klinkhammer, K., et al., *Deposition of electrospun fibers on reactive substrates for in vitro investigations.* Tissue Engineering Part C: Methods, 2009. **15**(1): p. 77-85.
182. Schindelin, J., et al., *Fiji: an open-source platform for biological-image analysis.* Nature methods, 2012. **9**(7): p. 676-682.
183. Nikolakopoulou, P., et al., *Recent progress in translational engineered in vitro models of the central nervous system.* Brain, 2020. **143**(11): p. 3181-3213.
184. Beghi, E., et al., *Global, regional, and national burden of epilepsy, 1990–2016: a systematic analysis for the Global Burden of Disease Study 2016.* The Lancet Neurology, 2019. **18**(4): p. 357-375.
185. Ngo, M.T. and B.A. Harley, *Progress in mimicking brain microenvironments to understand and treat neurological disorders.* APL bioengineering, 2021. **5**(2): p. 020902.
186. Liu, L., et al., *Biomanufacturing of a novel in vitro biomimetic blood-brain barrier model.* Biofabrication, 2020. **12**(3): p. 035008.
187. Hu, Y., et al., *Matrix stiffness changes affect astrocyte phenotype in an in vitro injury model.* NPG Asia Materials, 2021. **13**(1): p. 1-15.
188. Dede Eren, A., et al., *Tendon-derived biomimetic surface topographies induce phenotypic maintenance of tenocytes in vitro.* Tissue Engineering Part A, 2021. **27**(15-16): p. 1023-1036.
189. Carpenter, A.E., et al., *CellProfiler: image analysis software for identifying and quantifying cell phenotypes.* Genome biology, 2006. **7**(10): p. 1-11.
190. Castilho, M., et al., *Bi-layered micro-fibre reinforced hydrogels for articular cartilage regeneration.* Acta biomaterialia, 2019. **95**: p. 297-306.
191. Tylek, T., et al., *Precisely defined fiber scaffolds with 40 μm porosity induce elongation driven M2-like polarization of human macrophages.* Biofabrication, 2020. **12**(2): p. 025007.
192. Grafahrend, D., et al., *Degradable polyester scaffolds with controlled surface chemistry combining minimal protein adsorption with specific bioactivation.* Nature materials, 2011. **10**(1): p. 67-73.
193. Sloan, S.A. and B.A. Barres, *Mechanisms of astrocyte development and their contributions to neurodevelopmental disorders.* Current opinion in neurobiology, 2014. **27**: p. 75-81.
194. Bayraktar, O.A., et al., *Astrocyte development and heterogeneity.* Cold Spring Harbor perspectives in biology, 2015. **7**(1): p. a020362.
195. Eichholz, K.F. and D.A. Hoey, *Mediating human stem cell behaviour via defined fibrous architectures by melt electrospinning writing.* Acta biomaterialia, 2018. **75**: p. 140-151.
196. Puschmann, T.B., et al., *Bioactive 3D cell culture system minimizes cellular stress and maintains the in vivo-like morphological complexity of astroglial cells.* Glia, 2013. **61**(3): p. 432-440.
197. Johnson, C.D., et al., *Electrospun fiber surface nanotopography influences astrocyte-mediated neurite outgrowth.* Biomedical Materials, 2018. **13**(5): p. 054101.
198. Hara, M., et al., *Interaction of reactive astrocytes with type I collagen induces astrocytic scar formation through the integrin–N-cadherin pathway after spinal cord injury.* Nature medicine, 2017. **23**(7): p. 818-828.

199. Wieland, A., et al., *Brain and Breast Cancer Cells with PTEN Loss of Function Reveal Enhanced Durotaxis and RHOB Dependent Amoeboid Migration Utilizing 3D Scaffolds and Aligned Microfiber Tracts.* Cancers, 2021. **13**(20): p. 5144.
200. Vermeulen, S., et al., *Expanding Biomaterial Surface Topographical Design Space through Natural Surface Reproduction.* Advanced Materials, 2021. **33**(31): p. 2102084.
201. Prendergast, M.E. and J.A. Burdick, *Recent advances in enabling technologies in 3D printing for precision medicine.* Advanced Materials, 2020. **32**(13): p. 1902516.
202. Stukel, J.M. and R.K. Willits, *Mechanotransduction of neural cells through cell–substrate interactions.* Tissue Engineering Part B: Reviews, 2016. **22**(3): p. 173-182.
203. Gong, L., et al., *Materials for Neural Differentiation, Trans-Differentiation, and Modeling of Neurological Disease.* Advanced Materials, 2018. **30**(17): p. 1705684.
204. Tschugg, A., et al., *A prospective randomized multicenter phase I/II clinical trial to evaluate safety and efficacy of NOVOCART disk plus autologous disk chondrocyte transplantation in the treatment of nucleotomized and degenerative lumbar disks to avoid secondary disease: safety results of Phase I—a short report.* Neurosurgical review, 2017. **40**(1): p. 155-162.
205. Dellaquila, A., et al., *In Vitro Strategies to Vascularize 3D Physiologically Relevant Models.* Advanced Science, 2021: p. 2100798.
206. Harley, W.S., et al., *Advances in biofabrication techniques towards functional bioprinted heterogeneous engineered tissues: A comprehensive review.* Bioprinting, 2021: p. e00147.
207. Hrynevich, A., et al., *Design of Suspended Melt Electrowritten Fiber Arrays for Schwann Cell Migration and Neurite Outgrowth.* Macromolecular Bioscience, 2021: p. 2000439.
208. Phamduy, T.B., et al., *Printing cancer cells into intact microvascular networks: a model for investigating cancer cell dynamics during angiogenesis.* Integrative Biology, 2015. **7**(9): p. 1068-1078.
209. Guzzi, E.A. and M.W. Tibbitt, *Additive manufacturing of precision biomaterials.* Advanced Materials, 2020. **32**(13): p. 1901994.
210. Ayan, B., et al., *Aspiration-assisted bioprinting for precise positioning of biologics.* Science advances, 2020. **6**(10): p. eaaw5111.
211. Kim, M.H., et al., *Aspiration-assisted freeform bioprinting of mesenchymal stem cell spheroids within alginate microgels.* bioRxiv, 2021.
212. Mekhileri, N., et al., *Automated 3D bioassembly of micro-tissues for biofabrication of hybrid tissue engineered constructs.* Biofabrication, 2018. **10**(2): p. 024103.
213. An, J., C.K. Chua, and V. Mironov, *Application of Machine Learning in 3D Bioprinting: Focus on Development of Big Data and Digital Twin.* International Journal of Bioprinting, 2021. **7**(1).
214. Vasilevich, A.S., et al., *On the correlation between material-induced cell shape and phenotypical response of human mesenchymal stem cells.* Scientific reports, 2020. **10**(1): p. 1-15.
215. Goh, G.D., S.L. Sing, and W.Y. Yeong, *A review on machine learning in 3D printing: applications, potential, and challenges.* Artificial Intelligence Review, 2021. **54**(1): p. 63-94.
216. Duarte Campos, D.F. and L. De Laporte, *Digitally Fabricated and Naturally Augmented In Vitro Tissues.* Advanced Healthcare Materials, 2021. **10**(2): p. 2001253.
217. Mir, T.A., et al., *Biofabrication offers future hope for tackling various obstacles and challenges in tissue engineering and regenerative medicine: A Perspective.* International Journal of Bioprinting, 2019. **5**(1).
218. Ng, W.L., et al., *Deep learning for fabrication and maturation of 3D bioprinted tissues and organs.* Virtual and Physical Prototyping, 2020. **15**(3): p. 340-358.
219. Yang, Y., et al., *Deep learning for in vitro prediction of pharmaceutical formulations.* Acta pharmaceutica sinica B, 2019. **9**(1): p. 177-185.

220. Miri, A.K., et al., *Effective bioprinting resolution in tissue model fabrication.* Lab on a Chip, 2019. **19**(11).
221. Xue, J., et al., *Electrospinning and electrospun nanofibers: Methods, materials, and applications.* Chemical reviews, 2019. **119**(8): p. 5298-5415.
222. Bakirci, E., et al., *Melt Electrowriting of Amphiphilic Physically Crosslinked Segmented Copolymers.* Macromolecular Chemistry and Physics: p. 2100259.
223. Chen, D., et al., *Machine learning based methodology to identify cell shape phenotypes associated with microenvironmental cues.* Biomaterials, 2016. **104**: p. 104-118.
224. Balachander, G.M., et al., *3D Tumor Models for Breast Cancer: Whither We Are and What We Need.* ACS Biomaterials Science & Engineering, 2021. **7**(8): p. 3470-3486.

7. Curriculum vitae

8. Declaration of authorship

Statement of individual author contributions and of legal second publication rights:

Publication Ezgi Bakirci, Andreas Frank, Simon Gumbel, Paul F. Otto, Eva Fürsattel, Ingrid Tessmer, Hans-Werner Schmidt, Paul D. Dalton.

"Melt Electrowriting of Amphiphilic Physically Crosslinked Segmented Copolymers" Macromolecular Chemistry and Physics; (2021) 2100259

Participated in	**Author Initials,** Responsibility decreasing from left to right				
Study Design Methods Development	EB	PD	AF	HWS	
Data Collection	EB	AF	SG	PFO	IT
Data Analysis and Interpretation	EB	AF	SG		
Manuscript Writing Writing of Introduction Writing of Materials & Methods Writing of Discussion Writing of First Draft	EB EB EB EB EB	AF AF	SG		

Explanations (if applicable):

Publication Ezgi Bakirci, Andreas Frank, Simon Gumbel, Paul F. Otto, Eva Fürsattel, Ingrid Tessmer, Hans-Werner Schmidt, Paul D. Dalton.

“Melt Electrowriting of Amphiphilic Physically Crosslinked Segmented Copolymers” Macromolecular Chemistry and Physics; (2021) 2100259

Figure	**Author Initials,** Responsibility decreasing from left to right				
1	SG	EB			
2	AF				
3	EB				
4	EB	AF			
5	IT	EB			
6	EB	SG			
7	EB				

Publication

Ezgi Bakirci, Natascha Schaefer, Ouafa Dahri, Andrei Hrynevich, Pamela Strissel, Reiner Strick, Paul D. Dalton, and Carmen Villmann.

"Melt electrowritten in vitro radial device to study cell growth and migration." *Advanced Biosystems* 4, no. 10 (2020): 2000077.

Participated in	**Author Initials,** Responsibility decreasing from left to right				
Study Design Methods Development	EB	PD	OD		
Data Collection	EB	NS	CV	OD	
Data Analysis and Interpretation	EB	NS	PD	CV	
Manuscript Writing Writing of Introduction Writing of Materials & Methods Writing of Discussion Writing of First Draft	EB EB EB EB EB	PD NS NS NS	PD	CV	

Explanations (if applicable):

Publication Ezgi Bakirci, Natascha Schaefer, Ouafa Dahri, Andrei Hrynevich, Pamela Strissel, Reiner Strick, Paul D. Dalton, and Carmen Villmann.

"Melt electrowritten in vitro radial device to study cell growth and migration." *Advanced Biosystems* 4, no. 10 (2020): 2000077.

Figure	**Author Initials,** Responsibility decreasing from left to right				
1	EB	AH			
2	EB	AH			
3	EB				
4	NS	CV	EB		
5					

The doctoral researcher confirms that she/he has obtained permission from both the publishers and the co-authors for legal second publication.

The doctoral researcher and the primary supervisor confirm the correctness of the above mentioned assessment.

Ezgi Bakirci 05/11/2021 Wuerzburg

_____

Doctoral Researcher's Name Date Place Signature

Prof. Paul D. Dalton

_____

Primary Supervisor's Name Date Place Signature

9. Affidavit

I hereby confirm that my thesis entitled is the result of my own work. I did not receive any help or support from commercial consultants. All sources and/or materials applied are listed and specified in the thesis. Furthermore, I confirm that this thesis has not yet been submitted as part of another examination process neither in identical nor in similar form.

Würzburg, 5/11/2021

Place, Date Signature

Eidesstattliche Erklärung

Hiermit erkläre ich an Eides statt, die Dissertation eigenständig, d.h. insbesondere selbständig und ohne Hilfe eines kommerziellen Promotionsberaters, angefertigt und keine anderen als die von mir angegebenen Quellen und Hilfsmittel verwendet zu haben. Ich erkläre außerdem, dass die Dissertation weder in gleicher noch in ähnlicher Form bereits in einem anderen Prüfungsverfahren vorgelegen hat.

Würzburg, 5/11/2021

Ort, Datum Unterschrift